Studies on Transport Properties of Single Crystal Transistors Based on Mixed-Stacked Charge-Transfer Complexes with Disorder or Nonuniformity

Thesis
Submitted to the Graduate School of Chemical Sciences and Engineering
Hokkaido University

In Fulfillment of the Requirement
for the Degree of Doctor of Science

Seiya YOKOKURA

December, 2015

Acknowledgment

This work has been carried out under the supervision of Professor Tamotsu Inabe at the Solid State Chemistry Laboratory, Division of Chemistry, Graduate School of Science, Hokkaido University, could not be accomplished without the support of many people.

First of all, the author would like to express the sincerest gratitude for Professor Tamotsu Inabe. Without his valuable discussions, various suggestions and continuous encouragement, this thesis would never be completed.

The author would like to express his thanks to Associate Professor Jun Harada, Dr. Yukihiro Takahashi and Dr. Hiroyuki Hasegawa for their warmhearted encouragement, instructive discussions and thoughtful advices.

The author would like to express appreciation for Professor Sadamu Takeda (Hokkaido University), who are the main research advisor of this thesis. The author is indebted to him for the DSC measurements. The author would like to express appreciation for Professor Takanori Suzuki, Professor Kazuki Sada and Professor Toshihiro Shimada, who are the co-research advisors of this thesis.

The author acknowledges to Professor Hiroshi Okamoto (University of Tokyo) for measurements of the optical spectra and giving useful and helpful advices about the results. The author acknowledges to Professor Kunio Awaga and Associate Professor Michio Matsushita (Nagoya University) for the fabrications of the transistors and many useful discussions. The author acknowledges to Professor Reiji Kumai (CMRC, KEK) for useful and helpful discussion about the research. The author is indebted to Professor Yukio Hinatsu and Associate Professor Makoto Wakeshima (Hokkaido University) for the SQUID measurements.

The author is thankful to the present and senior members of the Solid State Chemistry Laboratory, Hokkaido University. The author thanks to his senior, Dr. Hiroyuki Kubota, Dr. Yukari Nakagawa, Mr. Takahiro Takano, and Mr. Kei Hayakawa for their appropriate advices and kindness. The author also thanks to Mr. Yu Kudo, Mr. Yuki Nakagawa, Mr. Shunsuke Muroi, Mr. Tsuyoshi Osaki, Mr. Yusuke Takita and Mr. Tomohiro Mikasa for their partnership. The author also thanks to the office administrators of the laboratory, Ms. Shouko Demachi and Ms. Yoshie Kosuge for their advices in his public and private life. And the author wishes to entrust the progress of *Team Takahashi* to Mr. Takuro Shimada and Ms. Mika Takehisa.

The author is thankful to many friends, in particular, Mr. Ikumi Shimoyama, Mr. Hiroki Mano, Mr. Takaaki Yoshida, Mr. Shigetoshi Takasugi and Mr. Wataru Kakihara for their friendship.

Finally, the author is deeply grateful to his parents Toshiyuki and Reiko, his brother Masaya, his sister Hiromi and his grandmother Husai for their understandings, continuous supports and heartwarming encouragement.

Seiya YOKOKURA

Contents

3. FL–TCNQ at 300 K
4. FL–TCNQ at 100 K
5. TET–TCNQ at 300 K

Chapter 1.

General Introduction

1.1. Organic Electronics

Our home electrical appliances, such as TV, PC and smartphone, are composed of many and various electronic devices (transistors and light-emitting devices, etc.). Although these devices mainly consist of inorganic semiconductors composed of such like Si and Ga at present, the devices using organic semiconductor have also been developed actively (organic electronics).[1-4] Because organic materials are assemblies of small molecules and/or polymers with relatively weak interaction (van der Waals' force), organic semiconductors are much more flexible than inorganic semiconductors, which are assembled by covalent bonds and/or ionic bonds. Advantages such as light-weight and flexiblity will be given by organic electronics since we can fabricate organic devices by embrocation or evaporation of organic semiconductors on plastic substrates.[3-5] Organic electronics are called as “flexible electronics” and “plastic electronics” from these aspects. By applying the printing technique for the device fabrication,[6-8] additionally, large-area organic devices can be obtained with decreasing the process cost. Because of these attractive features, researches of organic electronics are developed actively as the next-generation electronic devices.

1.2. Organic Semiconductors

Organic electronics is supported by organic semiconducting materials, which mainly involve π-conjugated electron systems. Typical organic semiconductors are polyacene type, such as tetracene and pentacene, phthalocyanine type, and polymer type materials.[9] Because of the closed-shell electronic systems in these molecules, the single component crystals become intrinsic semiconductor (insulator) generally, where the valence band and conduction band are separated by the band gap (Figure 1.2.1).

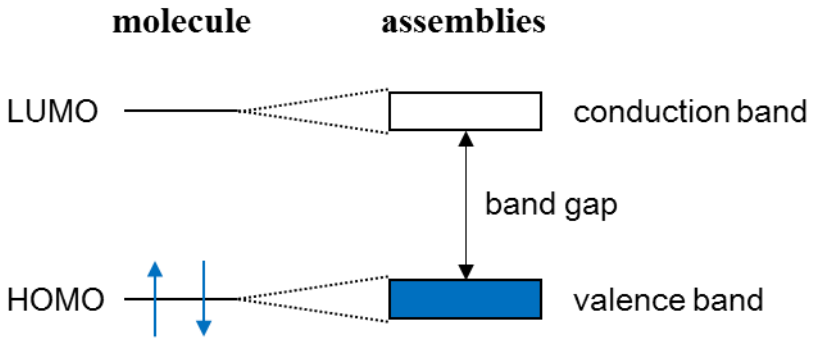

Figure 1.2.1. Formation of band structure of single component molecular crystals.

One of the most important parameters for applying organic semiconductor to organic electronics is the mobility,[10] which represents how smoothly carriers can move through a semiconductor, when an electric field is applied. The Hall-effect measurement[11] is one of the method to know the intrinsic mobility of the material, by which we can obtain not only the mobility but also the type of carriers; the hole in the valence band or the electron in the conduction band. But, the resistivity of these organic semiconductors are too high to measure the intrinsic mobility by the Hall-effect measurement. The mobility is usually estimated from field-effect mobility of the field-effect transistor,[10] which is one of the most important devices

for organic electronics (see 1.3). In organic semiconductors, three kinds of carrier transport models, which are the band transport, hopping transport, and disorder transport models, are proposed from the temperature dependence of the mobility (Figure 1.2.2).[12] The band or hopping transport model can be used when the mobility increase or decrease with lowering the temperature, respectively. The disorder transport model is applied for the system whose mobility is temperature independent.

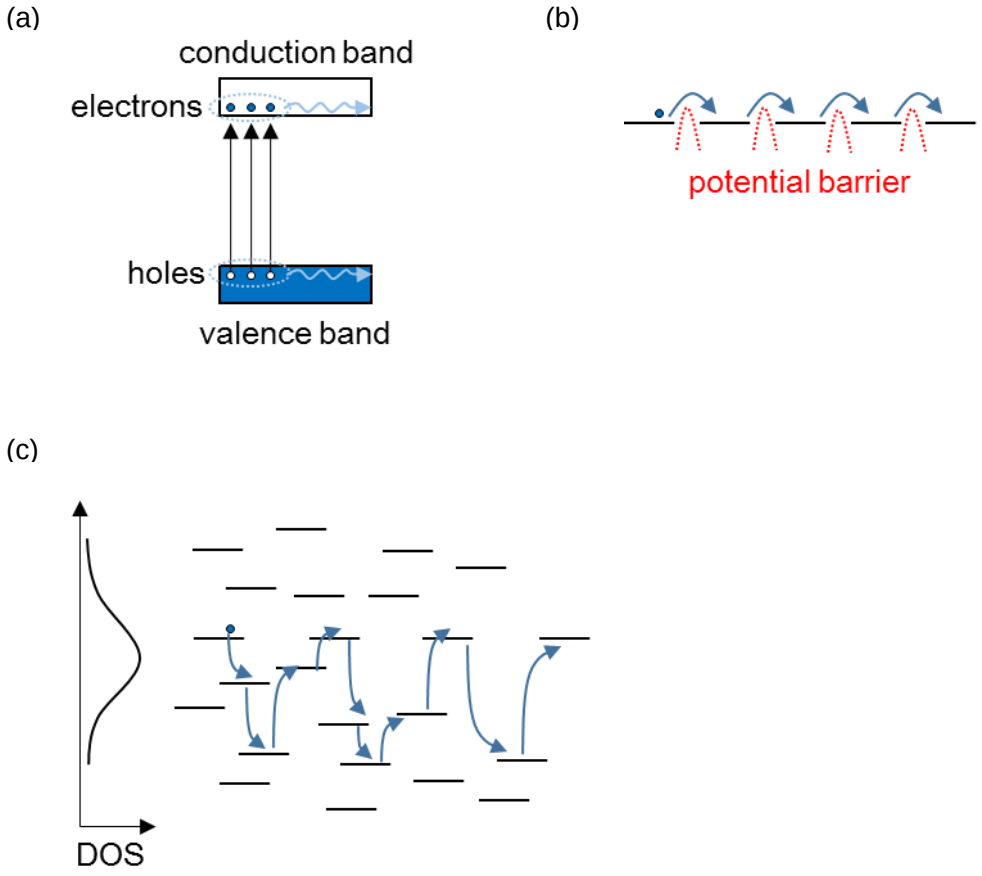

Figure 1.2.2. Schematics of transport models; (a) band transport, (b) hopping transport, and (c) disorder transport model.

The carriers in inorganic materials exhibit band transport since the electrons are delocalized

through the covalent bonds. On the other hand, the carriers in organic semiconductors had been considered not to be band transport, because of the relatively small overlap between molecular orbitals and the significant coupling to thermal molecular vibrations, both of which play a significant roles even at room temperature.[13] Until the end of the 20th century, the mobility of organic transistor was low and exhibited thermally activated behavior with decreasing the temperature. Thus, the hopping transport model was usually applied to the transport in organic semiconductors. In this century, many high mobility organic transistors, such as the single-crystal transistors were reported,[6,14,15] including those using newly synthesized materials. The mobility of some transistors showed the increase with decreasing the temperature, indicating that band-like transport can occur also in organic semiconductors. In addition, the disorder model has been found to be applied to the liquid crystal materials where the intermolecular interaction operates randomly.[16]

1.3. Organic Field-Effect Transistors (OFETs)

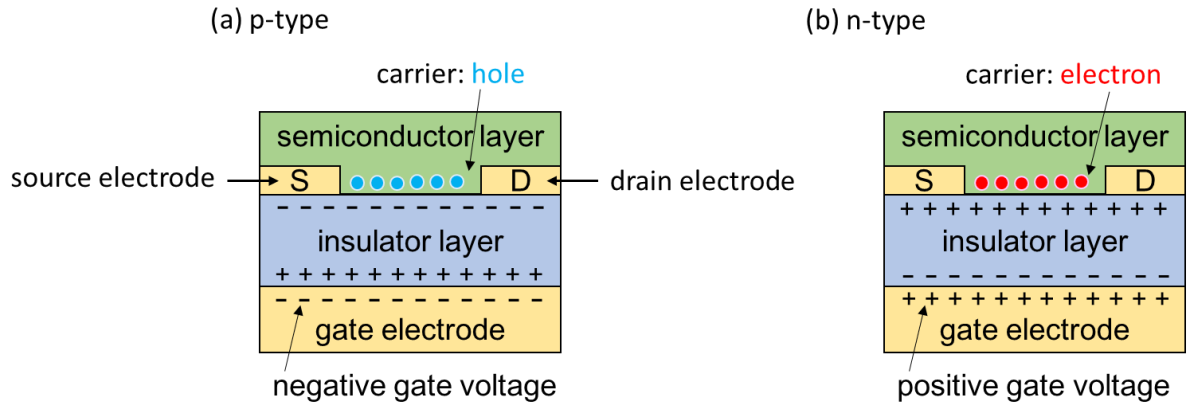

Figure 1.3.1. Schematic of transistor. (a) p-type and (b) n-type.

Organic field-effect transistors (OFETs) is the transistors using organic semiconductors as

the channel (semiconductor) layer. Typical structure of OFETs is shown in Figure 1.3.1.[14] OFETs are composed of an insulator layer, a semiconductor layer, source-drain electrodes and gate electrode. The source-drain current was enhanced by applying gate voltage since the carriers were accumulated in the insulator-semiconductor interface by the field-effect. When the current is enhanced by positive (negative) gate voltage, the FET is called as n-type (p-type) since the carriers are electrons (holes), respectively. The word, n-type or p-type semiconductor, is used also in organic semiconductors, though it does not mean that electrons or holes exist in the semiconductor. Whether the OFETs show n-type or p-type behavior mainly depends on the relationship between the Fermi level of the source-drain electrodes and the energy of the conduction and valence bands of the semiconductor, i.e. n-type (p-type) behavior is observed in the device where the Fermi level is located near the conduction (valence) band, respectively (Figure 1.3.2).[14] In general, organic semiconductors with high energy of the valence band composed by the HOMO, which is usually electron donor molecule, tend to show p-type behavior. On the other hand, those with low energy of the conduction band composed by the LUMO, which is usually electron acceptor molecule, tend to show n-type behavior. Typical p-type and n-type materials are shown in Figure 1.3.2. In addition, the carrier injection can be tuned by varying the electrode material. Although the FET utilizing rubrene as the semiconductor layer shows p-type behavior with using Au electrodes, the device with Ca electrodes shows n-type behavior.[17] Thus, not only the electronic structure of semiconductor, but also the semiconductor-electrodes interface is important for the design of devices with desirable properties. The transfer properties of OFETs can also be varied by gas adsorption on the semiconductor layer. The gas adsorption induce the change of electronic state of semiconductor, resulting in change of the transport property.[18] The solution processable and high mobility TFTs (thin-film transistors) have also been reported with using the soluble and

high crystallinity molecules tuned by substituent groups.[6,7,19]

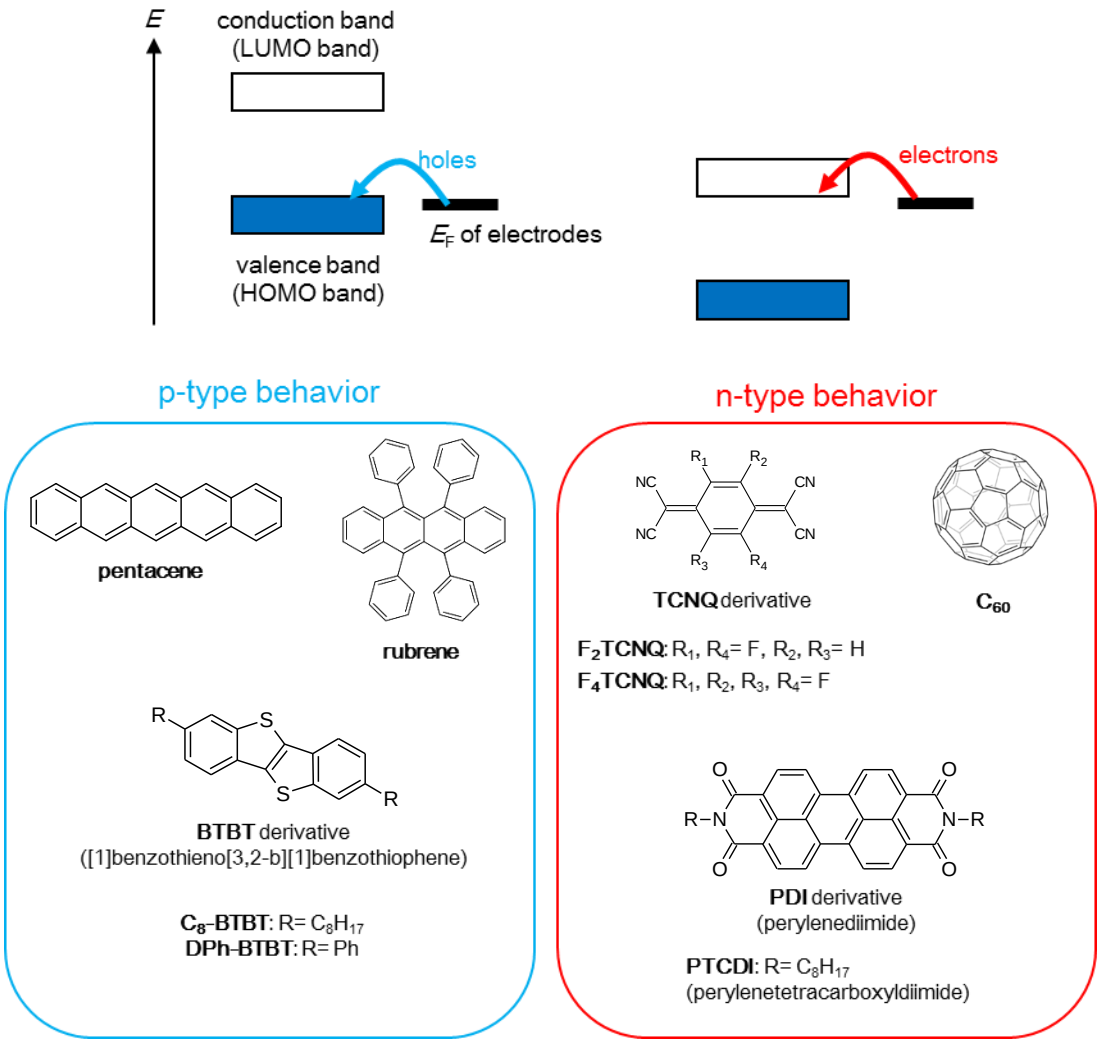

Figure 1.3.2. Schematic of carrier injection (top) and typical p-type and n-type materials (bottom).

Although TFTs are important for practical application of organic semiconductors, single-crystal transistors are relatively more useful for investigation of the transport mechanism since the thin-films in the transistor tend to be polycrystalline, resulting in grain boundary resistance. Until now, single crystal transistors have also been improved and the devices with high mobilities have also been reported. The Hall-effect measurements of the transistor using rubrene single crystal were reported by Takeya,[20] where the field-effect mobility was almost

consistent with the mobility estimated from the Hall-effect at room temperature. Thus, I considered that the fabrication technique of transistor is improved enough to be applied for basic investigation of transport properties in organic crystals. In this thesis, I discuss the transport properties of charge-transfer complexes by fabricating the FETs using the crystals of CT complexes and by investigating their performance.

1.4. Charge-Transfer (CT) Complexes

Charge-transfer (CT) complexes consist of electron donor and acceptor molecules with CT interaction. The crystals of CT complexes are of great interest and importance in the field of molecular materials, showing high electrical conductivity and superconductivity.[21-23] These properties are observed in CT crystals with segregated-stacks of donor and acceptor molecules, forming independent π-electron systems based on each component as shown in Figure 1.4.1a. On the other hand, a CT complex whose donor and acceptor are alternately stacked with face-to-face stacking is classified as a mixed-stacked CT complex (Figure 1.4.2a). As mentioned above, the CT crystals with segregated-stack structure show high electrical conductivity such as TTF–TCNQ crystal,[24] which shows metallic transport. The HOMO of TTF and the LUMO of TCNQ were partially occupied by the CT from TTF to TCNQ in the crystal of TTF–TCNQ, resulting in the metallic bands (Figure 1.4.1).

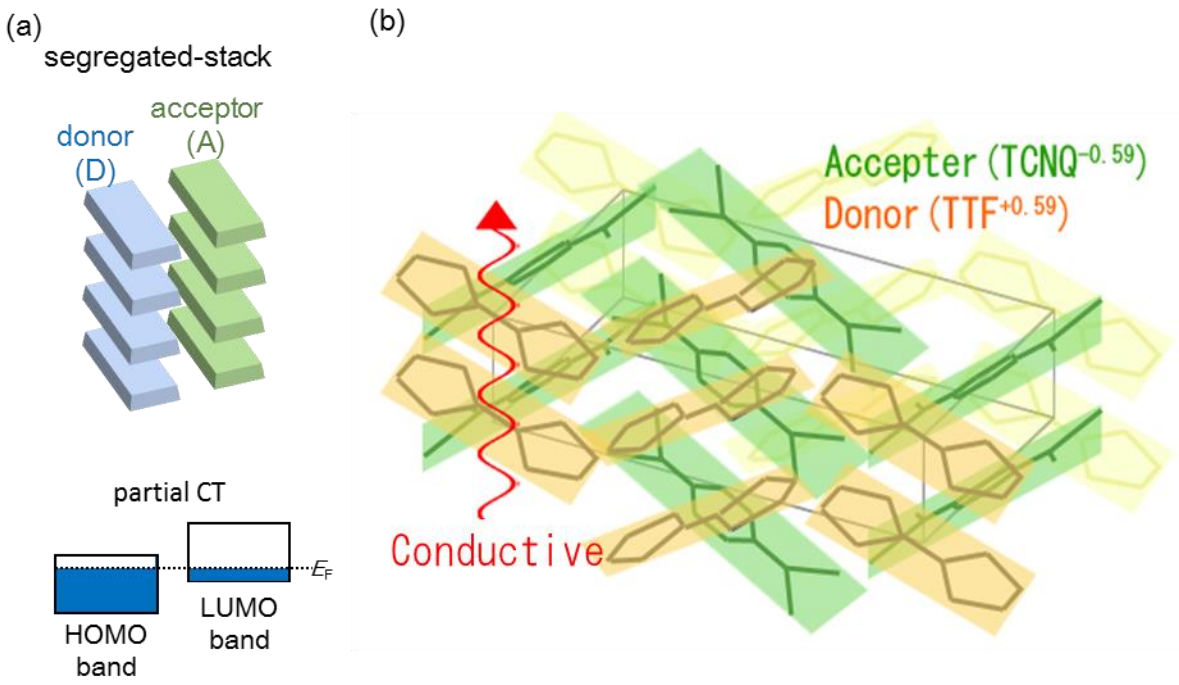

Figure 1.4.1. (a) Schematics of crystal and electronic structures of segregated-stack CT complex. (b) The crystal structure of TTF–TCNQ.

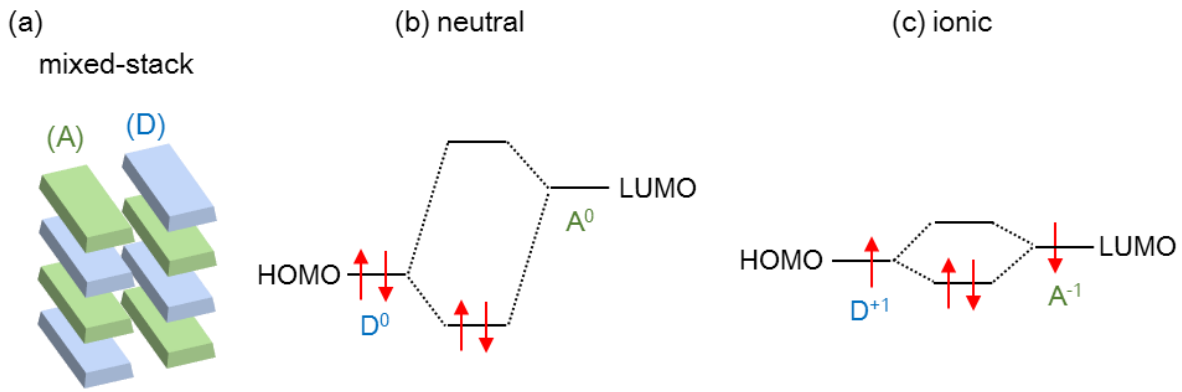

Figure 1.4.2. (a) Schematic of crystal structure of mixed-stack CT complex. Mixed-stacked DA pairs with (a) the neutral ground state and (b) the ionic ground state.

On the other hand, the mixed-stack CT complexes form fully occupied bands because of the alternately stacking structure, as shown for the energy level diagram of the mixed-stacking pair of D and A with either neutral or ionic ground state (Figure 1.4.2). Thus, mixed-stack CT

complexes must be semiconductors (insulators). It is considered that the band width is narrow because the π-stack column is composed of different molecules. Generally, the crystal, where the degree of CT is lower than 0.5, is regarded as having a neutral ground state, and that, where the degree of CT is not less 0.5, is regard as having an ionic ground state. The ground state can be assumed from the strength of electron donating and accepting abilities, which are correlated with the ionization potential of donor molecule and the electron affinity of acceptor molecule.[21] But in fact, because these parameters are not always available for all the components, especially the measurement of electron affinity is difficult, the oxidational and reduction potentials obtained by the electrochemistry in the solution state, namely by the cyclic voltammetry (CV) are approximately used for the estimation of the strength of electron donating and accepting abilities, respectively.[21]

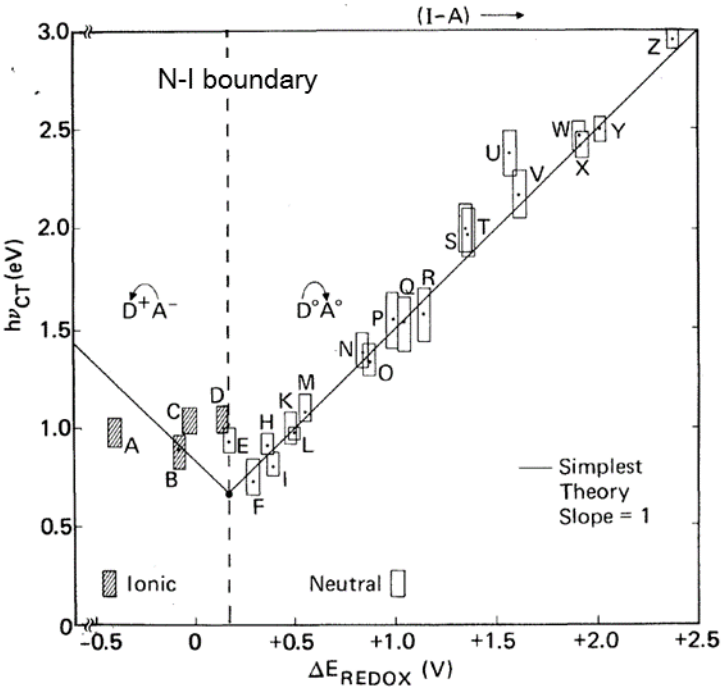

Figure 1.4.3. Ionicity diagram proposed by Torrance et al. (ref.25).

Torrance et al. discovered the V-shape relationship between the $h\nu_{CT}$ and ΔE, where $h\nu_{CT}$ is the CT energy and the ΔE is the difference between the redox potentials of the first oxidation

process of the donor and the first reduction process of the acceptor ($\Delta E = E_{ox}^{1/2}(D) - E_{red}^{1/2}$ (A)) (Figure 1.4.3).[25] The valley of the plot corresponds to the boundary of the neutral and ionic ground state (N-I boundary). They uncovered that the neutral-to-ionic transition occur in TTF–CA complex by decreasing the temperature, which located in the N-I boundary in the diagram (F in the plot). The TTF–CA crystal was investigated as a typical N-I transition material and confirmed various unique features; ferroelectricity at the ionic state,[26,27] pressure- and photo-induced N-I transition[28,29] and etc.[30,31] The mechanism of the N-I transition was also investigated by characterization of other complexes located at the N-I boundary. These complexes near the N-I boundary show higher conductivity than single component organic materials because of the narrow band gap, and the activation energy may become lower than that estimated from the band gap because of the 1D-fluctuation. Thus, the physical properties of the complexes located at the N-I boundary have actively been investigated and uncovered by many researchers. On the other hand, the complexes located far from the N-I boundary are insulators with high resistivity as well as single component materials, resulting in few discussion about the transport mechanism so far.

I focus attention of the neutral CT complexes with weak CT interaction, which located far from the N-I boundary. In such CT complexes, molecular dynamics such as in-plane reorientation can occur.[32-34] I consider that such molecular motion causes change of relative orientation of donor and acceptor molecules. The relative orientation is important in CT crystals since the CT interactions occur by overlap of π-orbitals of these molecules. In such crystals, it is expected that the CT interactions and electronic structures change by reorietational motion, resulting in unique transport property. Although the molecular dynamics in some of the CT crystals has been studied from a crystallographic aspect,[35] the dynamic nature of the molecules has not been linked to the transport property. Because of its high resistivity, it is difficult to

measure the temperature dependence down to low temperature, and it is not clear how the carriers transport in the crystal; which transfer model and which kind of carrier? The Hall-effect measurements are also difficult from the same reason as mentioned in section 1.3.

1.5. FETs of CT Complexes

I considered that characterization using transistor structure is useful for the investigation of the physical property. The mobility can be estimated by measuring the FET property, which is an important parameter for organic semiconductors. It is considered that the temperature dependence of the resistivity can be measured down to lower temperature than that performed for the conventional conductivity measurements because the current is enhanced by the gate voltage and the hole current and electron current can be detected individually. We can investigate the transport mechanism of each carrier separately. In addition, the transfer characteristics of OFETs can be varied by the change of the electronic state of the semiconductor layer. For example, gas sensors using OFET were reported, where the transport properties were varied by the electronic structure change which caused by gas adsorption on the semiconductor layer. I considered that the transfer properties of OFETs are also affected by the change of electronic and crystal structure of the semiconductor itself by phase transitions. Thus, I think characterization using transistor structure is more useful than the 2-probe resistivity measurement.

The FETs using CT complexes as the semiconductor layer had been reported.[36-38] Takahashi et al. reported the FET using single crystal of DBTTF–TCNQ, which is a neutral mixed-stack CT complex located near the N-I boundary (H in the plot of Figure 1.4.3).[25] The device showed high electron mobility (~1 $cm^2/(V \cdot s)$)[36] at room temperature because of the strong CT

interaction. In addition, they also reported tunability of carrier injections by using conductive CT complexes as electrodes (Figure 1.4.4).[37]

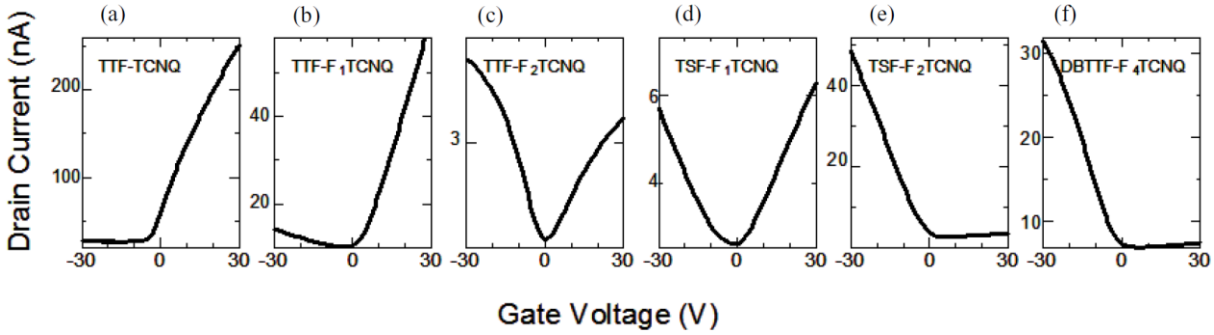

Figure 1.4.4. Transfer characteristics at V_D = 5 V of DBTTF–TCNQ single-crystal field effect transistors with source and drain electrodes composed of (a) TTF–TCNQ, (b) TTF–F_1TCNQ, (c) TTF–F_2TCNQ, (d) TSF–F_1TCNQ, (e) TSF–F_2TCNQ and (f) DBTTF–F_4TCNQ measured along the crystal long axes (reproduced from ref. 37).

From the another perspective, the FET using Mott-insulator CT compound, κ-(BEDT-TTF)$_2$Cu[N(CN)$_2$]Cl, was reported by Suda et al., in which the phase distribution tuning between Mott-insulator and superconductor phases could be achieved by the gate voltage (Figure1.4.5).[38]

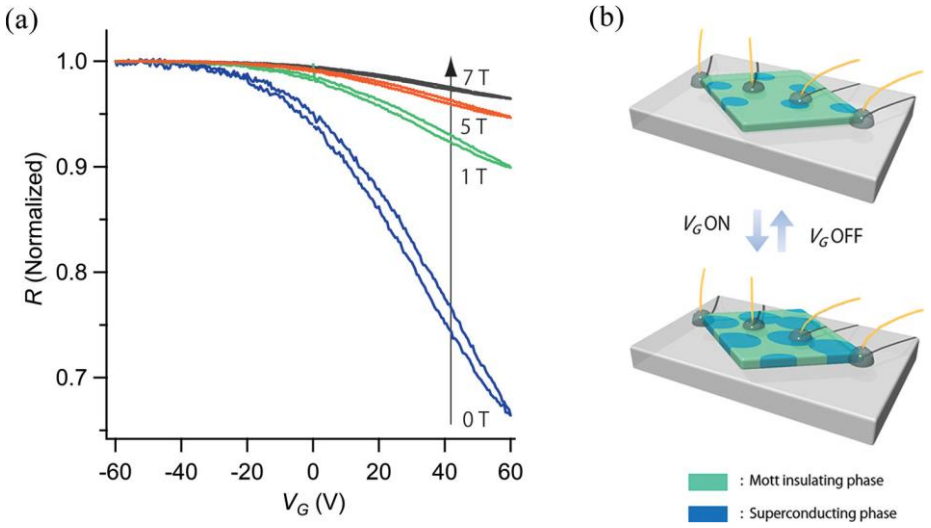

Figure 1.4.5. Plot of Normalized resistance versus applied gate voltage V_G for the FET using κ-(BEDT-TTF)$_2$Cu[N(CN)$_2$]Cl single crystal at 11 K with S = 0.67%, where S is the percentage of the extended length in the substrate. Blue, green, orange and black plots show the field-effects under external magnetic field of 0 T, 1 T, 5 T and 7 T, respectively. (b) Schematic illustrations for representing V_G OFF and V_G ON states of the device. When gate voltage is applied, the ratio of the superconducting fraction increases (reproduced from ref. 38).

Thus, although FETs using CT complexes have been investigated from some perspectives, only the complexes with strong CT interactions are used as semiconductor materials, whose transport properties can also be measured by 2- or 4-probe measurements because of their high enough conductivity. In this thesis, I tried to apply the FET measurements for the characterization of the transport properties of the CT complexes with weak CT interaction, whose transport properties have not been clarified because of the high resistivity. I fabricated and investigated FETs using seven kinds of CT complexes.

1.6. Outline of This Thesis

In Chapter 1, general introduction of this study is given. In this chapter, I introduced the back ground of organic electronics, material concepts of organic semiconductors and CT

complexes, and the methodological concept of FET.

In Chapter 2, an organic field-effect transistor have been fabricated using an anthracene–TCNQ single-crystal CT complex as the semiconductor material. The temperature dependence of the device is investigated. The CT complex shows molecular dynamics related to reorientational motion of anthracene molecule at room temperature. From thermal analysis, this complex undergoes two phase transitions with decreasing the temperature. The relationship between the transport property and the crystal and electronic structures of the complex is discussed based on the FET performance measurements.

In Chapter 3, FETs have been fabricated using fluorene–TCNQ and tetracene–TCNQ single-crystal CT complexes. The temperature dependence of the performance of these devices has been measured. The structural phase transitions are also confirmed in these complexes, resulting in transformation from the single crystal to the twinned crystal. The relationship between the transport property and the twinning of these complexes is mainly discussed.

In Chapter 4, FETs have been fabricated using four kinds of CT complexes, which are composed of the same donor molecule and four different acceptor molecules. The crystal structure of these complexes are different from each other. The relationship between the device properties and their molecular packing has been investigated.

Chapter 5 summarizes the importance of this research and contains the concluding remarks.

1.7. REFERENCES

1. Forrest, S. R. *Nature* **2004**, *428* (6986), 911.
2. Müller, C. D.; Falcou, A.; Reckefuss, N.; Rojahn, M.; Wiederhirn, V.; Rudati, P.; Frohne, H.; Nuyken, O.; Becker, H.; Meerholz, K. *Nature* **2003**, *421* (6925), 829.
3. Wang, C.; Hwang, D.; Yu, Z.; Takei, K.; Park, J.; Chen, T.; Ma, B.; Javey, A. *Nat. Mater.* **2013**, *12* (10), 899.
4. Sekitani, T.; Nakajima, H.; Maeda, H.; Fukushima, T.; Aida, T.; Hata, K.; Someya, T. *Nat. Mater.* **2009**, *8* (6), 494.
5. Webb, R. C.; Bonifas, A. P.; Behnaz, A.; Zhang, Y.; Yu, K. J.; Cheng, H.; Shi, M.; Bian, Z.; Liu, Z.; Kim, Y.-S.; Yeo, W.-H.; Park, J. S.; Song, J.; Li, Y.; Huang, Y.; Gorbach, A. M.; Rogers, J. A. *Nat. Mater.* **2013**, *12* (10), 938.
6. Minemawari, H.; Yamada, T.; Matsui, H.; Tsutsumi, J.; Haas, S.; Chiba, R.; Kumai, R.; Hasegawa, T. *Nature* **2011**, *475* (7356), 364.
7. Diao, Y.; Tee, B. C.-K.; Giri, G.; Xu, J.; Kim, D. H.; Becerril, H. a; Stoltenberg, R. M.; Lee, T. H.; Xue, G.; Mannsfeld, S. C. B.; Bao, Z. *Nat. Mater.* **2013**, *12* (7), 665.
8. Fukuda, K.; Takeda, Y.; Yoshimura, Y.; Shiwaku, R.; Tran, L. T.; Sekine, T.; Mizukami, M.; Kumaki, D.; Tokito, S. *Nat. Commun.* **2014**, *5*, 4147.
9. Wang, C.; Dong, H.; Hu, W.; Liu, Y.; Zhu, D. *Chem. Rev.* **2012**, *112* (4), 2208–2267
10. Anthony, J. E. *Chem. Rev.* **2006**, *106* (12), 5028.
11. Kittel, C. *Introduction to Solid State Physics* 6th edn, Ch. 6 (Wiley, 1986)
12. Coropceanu, V.; Cornil, J.; da Silva Filho, D. A.; Olivier, Y.; Silbey, R.; Brédas, J.-L. *Chem. Rev.* **2007**, *107* (4), 926.
13. Pope, M; Swenberg, C.E. *Ann. Rev. Phys. Chem.***1984**. 35, 613

14. Hasegawa, T.; Takeya, J. *Sci. Technol. Adv. Mater.* **2009**, *10*, 024314.
15. Krupskaya, Y.; Gibertini, M.; Marzari, N.; Morpurgo, A. F. *Adv. Mater.* **2015**, *27* (15), 2453.
16. Kreouzis, T.; Donovan, K. J.; Boden, N.; Bushby, R. J.; Lozman, O. R.; Liu, Q. *J. Chem. Phys.* **2001**, *114* (4), 1797.
17. Takenobu, T.; Takahashi, T.; Takeya, J.; Iwasa, Y. *Appl. Phys. Lett.* **2007**, *90* (1), 013507.
18. Jeong, J. W.; Lee, Y. D.; Kim, Y. M.; Park, Y. W.; Choi, J. H.; Park, T. H.; Soo, C. D.; Won, S. M.; Han, I. K.; Ju, B. K. *Sensors Actuators B Chem.* **2010**, *146* (1), 40–45.
19. Gundlach, D. J.; Royer, J. E.; Park, S. K.; Subramanian, S.; Jurchescu, O. D.; Hamadani, B. H.; Moad, a J.; Kline, R. J.; Teague, L. C.; Kirillov, O.; Richter, C. a; Kushmerick, J. G.; Richter, L. J.; Parkin, S. R.; Jackson, T. N.; Anthony, J. E. *Nat. Mater.* **2008**, *7* (March), 216.
20. Takeya, J.; Kato, J.; Hara, K.; Yamagishi, M.; Hirahara, R.; Yamada, K.; Nakazawa, Y.; Ikehata, S.; Tsukagoshi, K.; Aoyagi, Y.; Takenobu, T.; Iwasa, Y. *Phys. Rev. Lett.* **2007**, *98* (19), 196804.
21. Saito, G.; Yoshida, Y. *Bull. Chem. Soc. Jpn.* **2007**, 80, 1.
22. Ferraris, J.; Cowan, D. O.; Walatka, V.; Perlstein, J. H. *J. Am. Chem. Soc.* **1973**, 95, 948.
23. Jérome, D. *Chem. Rev.* **2004**, 104, 5565.
24. Ferraris, J.; Cowan, D. O.; Walatka, V.; Perlstein, J. H. *J. Am. Chem. Soc.* **1973**, *95* (3), 948.
25. Torrance, J. B.; Vazquez, J. E.; Mayerle, J. J.; Lee, V. Y. *Phys. Rev. Lett.* **1981**, *46* (4), 253.
26. Okamoto, H.; Mitani, T.; Tokura, Y.; Koshihara, S.; Komatsu, T.; Iwasa, Y.; Koda, T.; Saito, G. *Phys. Rev. B* **1991**, *43* (10), 8224.
27. Kobayashi, K.; Horiuchi, S.; Kumai, R.; Kagawa, F.; Murakami, Y.; Tokura, Y. *Phys. Rev. Lett.* **2012**, *108* (23), 237601.
28. Tokura, Y.; Okamoto, H.; Koda, T.; Mitani, T. *Solid State Commun.* **1986**, *57* (8), 607.
29. Koshihara, S.; Tokura, Y.; Mitani, T.; Saito, G.; Koda, T. *Phys. Rev. B* **1990**, *42* (10), 6853.

30. Tokura, Y.; Okamoto, H.; Koda, T.; Mitani, T.; Saito, G. *Phys. Rev. B* **1988**, *38* (3), 2215–2218.
31. Guérin, L.; Hébert, J.; Buron-Le Cointe, M.; Adachi, S.; Koshihara, S.; Cailleau, H.; Collet, E. *Phys. Rev. Lett.* **2010**, *105* (24), 246101.
32. Lefebvre, J.; Odou, G.; Muller, M.; Mierzejewski, A.; Luty, T. *Acta Crystallogr. Sect. B Struct. Sci.* **1989**, 45, 323.
33. Fyfe, C. A. *J. Chem. Soc., Faraday Trans. 2* **1974**, 70, 1633.
34. Fyfe, C. A.; Harold-Smith, D.; Ripmeester, J. *J. Chem. Soc., Faraday Trans. 2* **1976**, 72, 2269.
35. Herbstein, F. H. *Crystalline Molecular Complexes and Compounds*; Oxford University Press: Oxford, U.K., **2005**; Vol. 2, Chapter 16.
36. Takahashi, Y.; Hasegawa, J.; Abe, Y.; Tokura, Y.; Nishimura, K.; Saito, G. *Appl. Phys. Lett.* **2005**, *86*, 1.
37. Takahashi, Y.; Hasegawa, T.; Abe, Y.; Tokura, Y.; Saito, G. *Appl. Phys. Lett.* **2006**, *88*, 073504.
38. Suda, M.; Kawasugi, Y.; Minari, T.; Tsukagoshi, K.; Kato, R.; Yamamoto, H. M. *Adv. Mater.* **2014**, *26* (21), 3490.

Chapter 2.

Switching of Transfer Characteristics of the Anthracene–TCNQ Field-Effect Transistor by Phase Transitions: Sensitive Response to Molecular Dynamics and Charge Fluctuation

2.1. INTRODUCTION

Planar molecules, such as naphthalene and pyrene, often undergo in-plane reorientation in crystals. In mixed-stack charge-transfer (CT) complexes, molecular dynamics was also reported to occur with using planer donor molecules such as anthracene–tetracyanobenzene, pyrene–tetracyanobenzene and pyrene–pyromellitic-dianhydride.[1-3] It is known that these complexes undergo phase transitions at low temperature, which are related to the order–disorder behavior of molecular orientation of these molecules.[4] Although the molecular dynamics in some of the CT crystals has been studied from a crystallographic aspect, the dynamic nature of the molecules has not been linked to CT interaction between donor and acceptor molecules. I consider that the reorientational motion causes a certain change of relative orientation of donor and acceptor molecules. The relative orientation is important in CT crystals since the CT interactions are originated from overlap of π-orbitals of these molecules. In such crystals, it is expected that the CT interactions and electronic structures change by reorietational motion. I consider that if one use such CT complexes as the semiconductor component of the field effect

transistors (FETs), the changes of electronic structure and reorientational motion in CT complex crystals caused by phase transition might be detected.

In this work, a FET was fabricated utilizing anthracene–tetracyanoquinodimethane (AN–TCNQ) single crystal and tetrathiafulvalene–TCNQ (TTF–TCNQ) metallic thin films as the semiconductor layer and the source and drain electrodes, respectively (Figure 2.1). AN–TCNQ is a classical mixed-stack CT complex whose crystal structure at room temperature was first reported in 1968.[5] Observed molecular structure of AN showed large atomic displacement parameters (temperature factors), which were interpreted as orientational disorder.[4] I have found that the transfer characteristics of the device show drastic changes with decreasing the temperature; n-type → ambipolar-type → p-type → ambipolar-type from room temperature to 90 K. The drastic changes can be explained by molecular dynamics and two structural phase transitions. This study showed that the measurement of FET characteristics of semiconductor materials is useful to investigate their electronic structures.

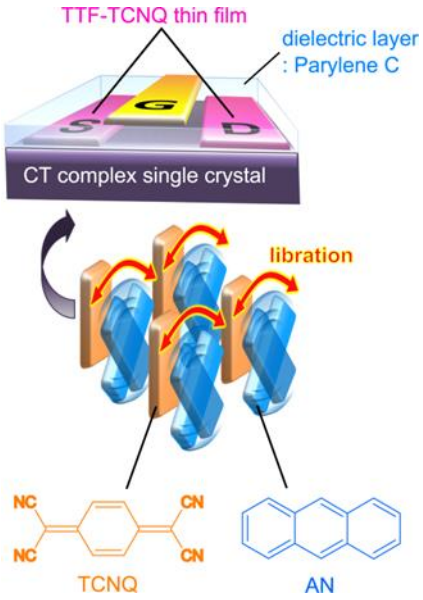

Figure 2.1 Schematic of the FET (top) and reorientation in the AN–TCNQ crystal (bottom).

In this chapter, the crystal preparation, the device fabrication and temperature dependence of the device properties AN–TCNQ of are shown at first. Then, molecular dynamics and phase transitions are described from the results of DSC measurements and single crystal X-ray analyses. In addition, the electronic structure was studied based on the optical and magnetic properties. Finally, the relationship between the device property and the molecular dynamic and electronic structure will be discussed.

2.2. EXPERIMENTAL SECTION

2.2.1. Materials

AN, TCNQ and TTF were purchased from Tokyo Chemical Industry Co., Ltd. and purified by vacuum sublimation. Single crystals of the AN–TCNQ complex (black blocks and sticks with a typical size of 0.2 × 0.4 × 1.0 mm^3) were prepared by a co-sublimation method in a sealed vacuum glass tube. The growth tube setup is presented in Figure 2.2.1. I used a three-zone-type electric furnace, where the temperature at each zone can be controlled individually. The source materials were located in the growth tube at the positions that correspond to 180 °C (TCNQ) and 150 °C (AN), respectively. The crystals of the complex were grown in the middle area, where the temperature was kept at 120 °C. The crystal structure of the crystals at room temperature was the same as that in a previous report.[32] TTF–TCNQ polycrystallites were obtained by mixing of each acetone solution of TTF and TCNQ.

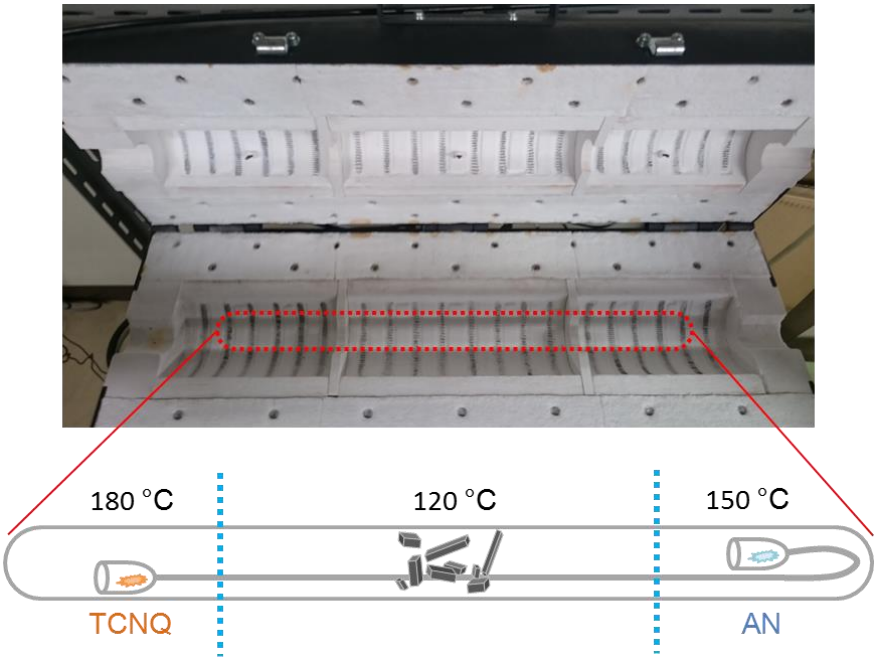

Figure 2.2.1. The furnace and growth tube used for the co-sublimation method for crystal growth.

2.2.2. Device Fabrication

Devices with gold or silver as the source and drain electrodes were also fabricated, but their transfer characteristics could not be measured at low temperature because of their large contact resistance. To improve the interfacial electrical contact for electron injection into the AN–TCNQ crystals, we used TTF–TCNQ metallic thin films as the source and drain electrodes (Figure 2.2.2). By thermal evaporation through shadow masks, metallic thin films were deposited on the (110) plane of a bulk single crystal of AN–TCNQ whose thickness was 200 μm. The channel width and length (*W* and *L*) of the obtained device were 675 and 50 μm, respectively. The two electrodes were arranged for the current to flow parallel to the molecular stacking axis of the AN–TCNQ crystal (*c* axis). A 0.5-μm layer of Parylene C was deposited as the gate dielectric layer (C_i = 5.1 nF/cm^2) by using specialized vacuum deposition equipment (A Specialty Coating Systems Company, PDS 2010). The process of fabricating the Parylene C film is summarized in Figure 2.2.2. Powder of starting material, dimer, was placed in furnace 1, and was vaporized into a dimeric gas (150 °C, 1.0 torr). The dimeric gas was pyrolyzed into monomeric gas in furnace 2 (650 °C, 0.5 torr). The monomeric gas entered the ambient temperature coating chamber and polymerized on the crystal surface. Gold gate electrodes were then formed on the top of the insulator layer.

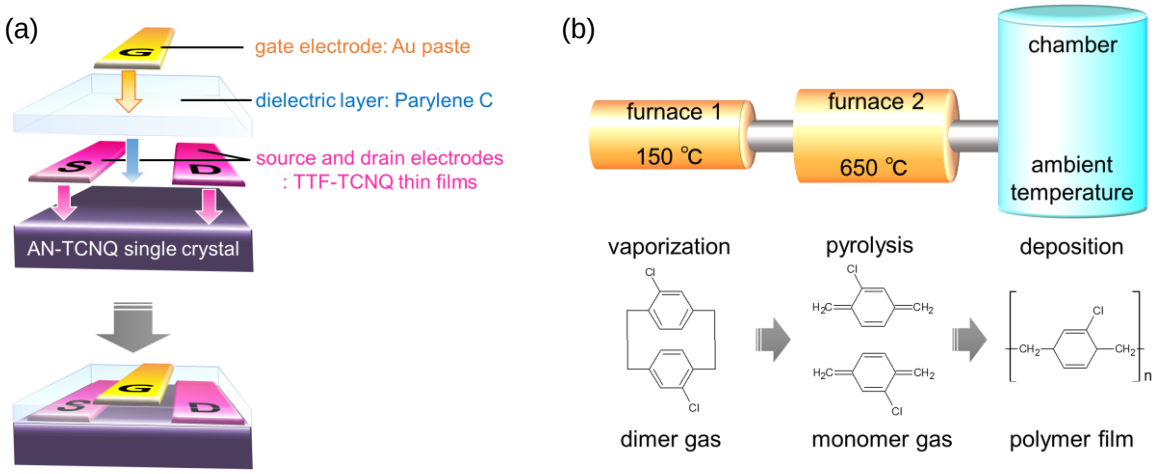

Figure 2.2.2. (a) Schematics of device fabrication and (b) thermal deposition of Parylene C.

2.2.3. Crystallographic Study

All of the diffraction measurements were performed on a Bruker SMART APEX II ULTRA diffractometer with a TXS rotating anode (Mo Kα radiation, λ = 0.71073 Å) and multilayer optics. The data collection was carried out using a DX-CS190LD N_2-gas-flow cryostat (Japan Thermal Engineering, Sagamihara, Japan). The temperature in the nozzle was kept constant within ±0.2 K during the measurement. Low-temperature measurements were performed by cooling the same crystal. The structures were solved by direct methods (SHELXT) and refined by full-matrix least-squares on F^2 using SHELXL-2014.[6] All of the H atoms were refined using a riding model. For the crystal structures without disorder, all of the non-H atoms were refined anisotropically. For the crystal structures with disorder of AN molecule, disordered molecules were restrained to be the same structure each other (SAME restraint). The ADPs were also restrained by rigid bond restraints (RIGU restraint). The details of the refinement are provided in the Appendix as the SHELXL-2014 res files. The crystal and experimental data are summarized in Table 2.2.1.

Table 2.2.1 Crystallographic Data for Each Phase of AN–TCNQ

	300 K	155 K	100 K
formula		$C_{26}H_{14}N_4$	
formula weight		382.41	
crystal size (mm^3)		0.30 × 0.20 × 0.20	
crystal system	monoclinic	monoclinic	triclinic
space group	$C2/m$	$P2_1/a$	$P\bar{1}$
a (Å)	11.5276(3)	11.5730(15)	11.370(3)
b (Å)	12.9749(4)	12.8479(16)	12.818(3)
c (Å)	7.0126(2)	6.9092(9)	6.9180(17)
α (°)	90	90	90.884(4)
β (°)	105.5838(14)	107.053(2)	107.171(4)
γ (°)	90	90	94.998(4)
V ($Å^3$)	1010.31(5)	982.2(2)	958.8(4)
Z	2	2	2
R_{int}	0.0166	0.0317	0.0312
R_1 [$I > 2\sigma(I)$]	0.0452	0.0413	0.0449
R_w (all reflection)	0.1477	0.1331	0.1174

2.2.4. Calculation

The overlap integrals between the highest occupied molecular orbital (HOMO) and next HOMO (nHOMO) of AN and the lowest unoccupied molecular orbital (LUMO) of TCNQ and band structure for each phase were calculated under the extended Hückel approximation[7,8] using the CAESAR program package.[9] The optimization and energy calculations of isolated single molecules were performed using Gaussian 09W at the B3LYP/6-31G(d,p) level.[10]

2.2.5. Measurements.

The device properties of the AN–TCNQ single-crystal FET were measured using a dual channel system source meter (Keithley 2636A). Temperature was controlled using a closed cycle cryostat system. Thermal analyses were performed by differential scanning calorimetry (DSC, Mettler Toledo Thermal Analysis System, DSC 1) with a heating and cooling rate of 5 K/min. The DSC profile was confirmed to be reproduced in the repeated thermal cycles. To

obtain the optical spectra of AN–TCNQ in the ultraviolet–visible (UV/vis) and infrared (IR) regions were measured by Prof. Okamoto's group at the University of Tokyo. A specially designed spectrometer with a 25-cm-grating monochromator (JASCO M25-GT) and an optical microscope and a Fourier transform IR spectrometer with an optical microscope, respectively were used. In the low-temperature measurements, a specially designed conduction-type cryostat was used. Magnetic susceptibility measurements were performed on a Quantum Design MPMS superconducting quantum interference device (SQUID) susceptometer with a static field of 1 T in the temperature range 2–300 K using randomly oriented polycrystalline sample. The diamagnetic core contribution was estimated based on Pascal's constants.[11]

2.3. RESULTS AND DISCUSSION

2.3.1. Field-Effect Transistor of an AN–TCNQ Single Crystal

The AN–TCNQ FET using gold as source and drain electrodes showed n-type behavior at 300 K, where the drain current (I_{SD}) is enhanced by positive gate voltage (V_G) (Figure 2.3.1). The mobility μ was estimated 5.4×10^{-7} cm^2/(V·s) applying the formula $\mu = (dI_{SD}/dV_G)\times[L/(WC_iV_D)]$ to the linear region of transfer characteristics. The device showed n-type behavior until 240 K with gradual decrease of μ. Below 240 K, current enhancement was not observed. The device could not work at low temperature since the contact between electrodes and semiconductor was not good enough. It is considered that the crystal surface was damaged by radiation heat during the vapor deposition of gold.

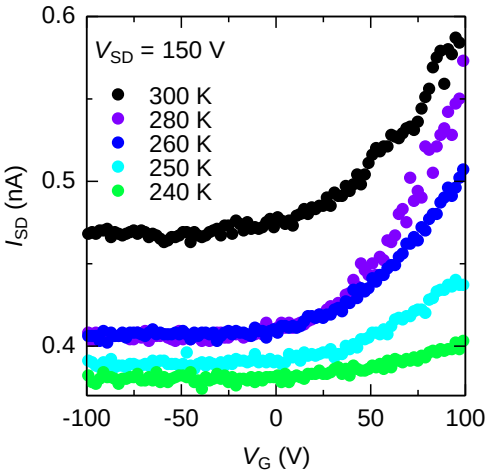

Figure 2.3.1. Temperature dependence of transfer characteristics of the AN–TCNQ FET using gold as source and drain electrodes. V_{SD} = 150 V in all temperature range.

Figure 2.3.2 shows the transfer characteristics in variable temperature with silver electrodes. The device also showed n-type behavior between 298-230 K. The device exhibited normally on behavior, the threshold voltage (V_{th}) was −0.3 V. The mobility μ was estimated 1.2×10^{-5}

$cm^2/(V \cdot s)$ at 298 K. It is considered that interfacial contact was improved because the deposition of silver can be done with lower radiation heat compared to gold. At 210 K, although the dominant carrier was electrons, slight p-type behavior was also observed. At 190 K, the device showed clear ambipolar behavior, where the I_{SD} is enhanced by both positive and negative V_G. At 170 K, the transfer characteristic could not be measured since the current was too small to detect.

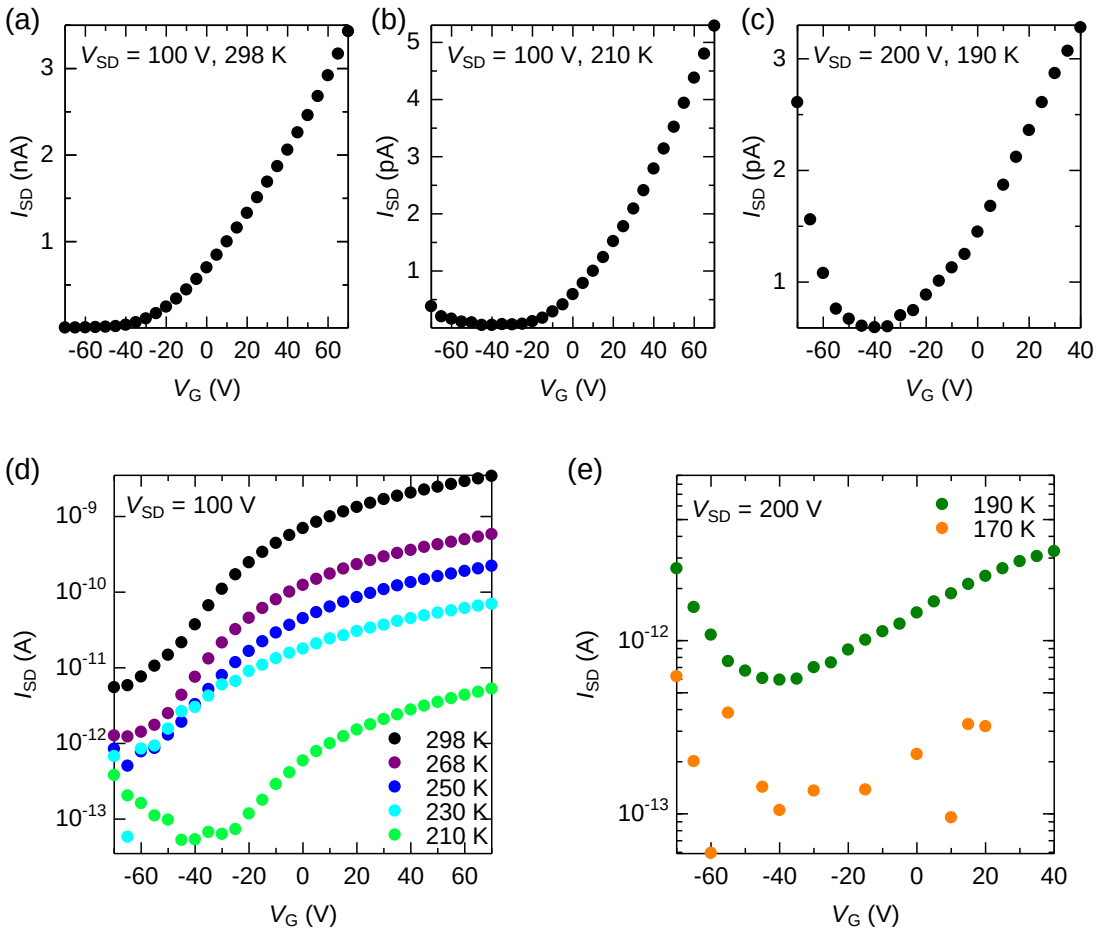

Figure 2.3.2. Temperature dependence of transfer characteristics of the AN–TCNQ FET using silver as source and drain electrodes. .V_{SD} = 100 V at the temperature range 300-210 K and V_{SD} = 200 V at the temperature range 190-170 K. (a) 298 K, (b) 210 K, (c) 190 K, (d) and (e) are log plot.

Devices with gold or silver as the source and drain electrodes were found to work at room

temperature, but their transfer characteristics could not be measured at low temperature because of their large contact resistance. To improve the interfacial electrical contact for electron injection into the AN–TCNQ crystals, we used TTF–TCNQ metallic thin films as the source and drain electrodes.

Figure 2.3.3 shows the device properties of the AN–TCNQ single-crystal FET in variable temperatures. The device showed typical n-type behavior at 300 K. The device exhibited normally on behavior, the threshold voltage (V_{th}) was −20.2 V. The mobility μ was estimated 4.5×10^{-5} $cm^2/(V \cdot s)$. At 250 K, although the dominant carrier was electrons, slight p-type behavior was also observed. The contribution of the p-type behavior of the device became significant than n-type with decreasing temperature: The device became clearly ambipolar at 220 K, and mostly p-type at 200 K, and exclusively p-type at 150 K. However, At 100 K, the device again showed ambipolar-type behavior with a relatively weak p-type contribution. The ambipolar behavior was maintained to the lowest temperature available (90 K). Thus, the transfer characteristics of the AN–TCNQ single-crystal FET drastically changed from n-type → ambipolar-type → p-type → ambipolar-type when the temperature decreased from room temperature to 100 K. The μ values of the n-type (μ_n) and p-type (μ_p) contributions, and the V_{th} values at each temperature are summarized in Table 2.3.1.

Table 2.3.1 Temperature Dependence of the Mobility in the AN–TCNQ FET with TTF–TCNQ Electrodes.

	300 K	250 K	220 K	200 K	150 K	100 K
μ_n ($cm^2/(V \cdot s)$)	4.5×10^{-5}	2.4×10^{-6}	3.2×10^{-7}	7.1×10^{-7}	-	6.2×10^{-8}
μ_p ($cm^2/(V \cdot s)$)	-	1.5×10^{-6}	5.7×10^{-7}	5.3×10^{-7}	5.0×10^{-7}	1.2×10^{-8}

It is well known that organic FETs show that increase or decrease of mobility by decreasing temperature, but switching between n-type and p-type has never been reported to my knowledge.

As shown below, the drastic changes in transfer characteristics of AN–TCNQ FET are related to the changes of molecular dynamics and electronic structure by two structural phase transitions, as presented in succeeding sections.

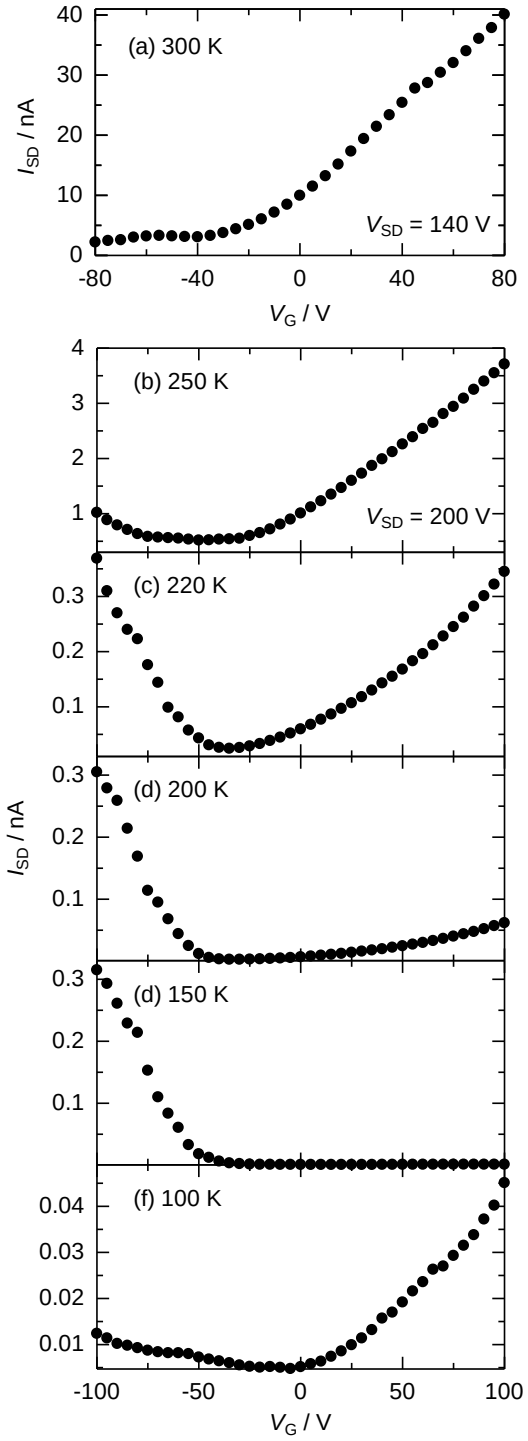

Figure 2.3.3. Transfer characteristics of the AN–TCNQ FET at (a) 300 K with V_{SD} = 140 V, (b) 250 K with V_{SD} = 200 V, (c) 220 K with V_{SD} = 200 V, (d) 200 K with V_{SD} = 200 V, (e) 150 K with V_{SD} = 200 V, and (f) 100 K with V_{SD} = 200 V.

2.3.2. Phase Transitions of AN–TCNQ

DSC measurements show the presence of two reversible structural phase transitions in AN–TCNQ at low temperatures (Figure 3). Two phase transitions are present in both processes (139 K, 160K in heating / 139 K, 161 K in cooling process). The transition enthalpy (entropy) values at low and high temperatures were calculated by integrating the areas of the DSC peaks as ΔH = 0.70 kJ mol^{-1} (ΔS = 5.0 J K^{-1} mol^{-1}) and ΔH = 0.49 kJ mol^{-1} (ΔS = 3.1 J K^{-1} mol^{-1}), respectively. I use the following nomenclature for each phase: HT phase (high-temperature phase, T > 160 K), IM phase (intermediate-temperature phase, 139 K< T <160 K), and LT phase (low-temperature phase, T < 139 K). The relationship between the device behavior and the phase transitions of the AN–TCNQ crystal can be summarized as follows. In the HT phase, with decreasing temperature, the FET of the AN–TCNQ single crystal changed from n-type to p-type behavior via ambipolar behavior (Figure 2a–d). In the IM phase, p-type behavior is maintained (Figure 2e), and the LT phase showed ambipolar behavior (Figure 2f).

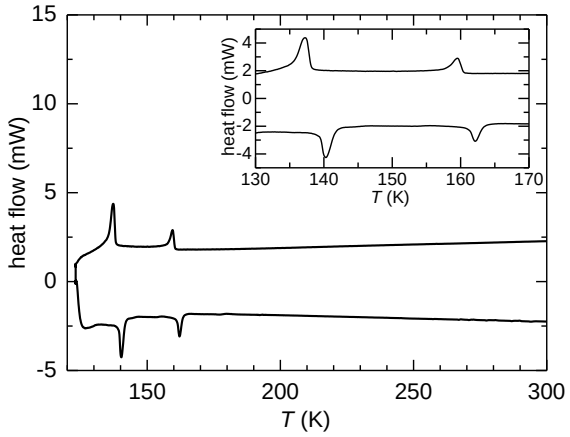

Figure 2.3.4. DSC profile of polycrystalline AN–TCNQ. The inset is that around phase transitions.

2.3.3. Crystal Structure of AN–TCNQ

The crystal structures in the HT (300 K), IM (155 K), and LT (100 K) phases were

determined by single-crystal X-ray structure analysis. In the HT phase the space group of the crystal is *C*2/*m*, and each molecule is located on the 2/*m* sites (Figure 2.3.5). The AN molecules were refined as the overlap of three different orientations, two of which were related to each other by the symmetry of the sites. In these two arrangements (blue and green), the molecular long axes of AN significantly deviate from the mirror plane, while both TCNQ (orange) and the remaining AN (gray) share the same mirror plane. The occupancies were refined to be 35.6(17) % (blue and green AN) and 28.8(34) % (gray AN). In the HT phase, it is considered that exchanging of these three orientations occur by in-plane molecular reorientation of AN. The molecular planes of AN and TCNQ were perpendicular to the stacking axis *c* and the inter-planer distance was estimated as 3.50 Å. All the mixed-stack columns are translationally related with each other.

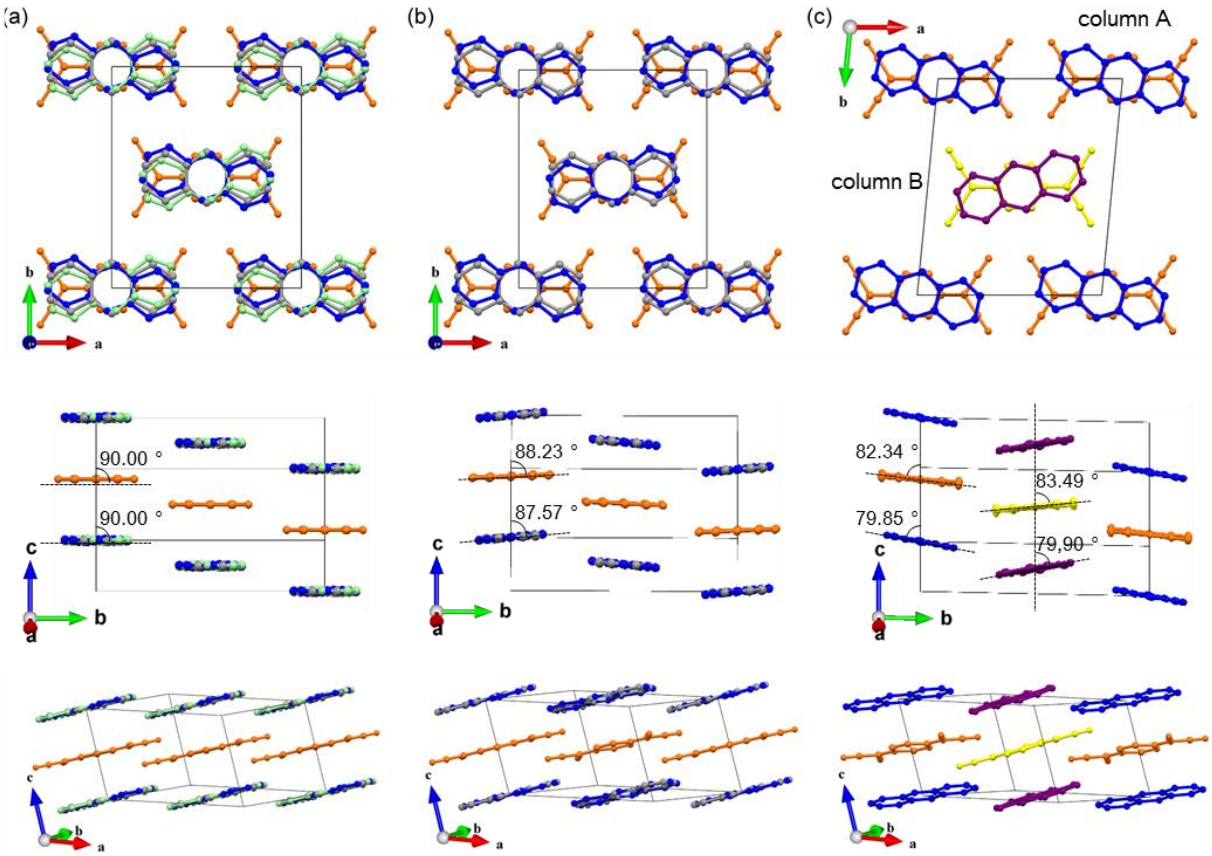

Figure 2.3.5 Crystal structures of AN–TCNQ at (a) 300, (b) 155, and (c) 100 K. Each top projection is viewed along the *c* axis, and middle is viewed along molecular long axes, and bottom perspective view indicates the mixed-stack columns at (0, 0, *z*), (1/2, 1/2, *z*), and (0, 0, *z*).

In the IM phase (155 K), the space group of the crystal is $P2_1/a$, which is lower symmetry than the HT phase (Figure 2.3.5b). In this space group, mirror symmetry is absent. Although orientational disorder was also observed in this phase, the number of orientation in the IM phase was different to that in the HT phase. There are two orientations of the AN molecule, and the occupancies are refined to be 65.2(13) % (blue AN) and 34.8(13) % (gray AN). The decrease of the number of orientation from three to two at the phase transition is consistent with the magnitudes of transition entropy, $\Delta S = R \ln(1.45)$ ($\sim R \ln(3/2) = 3.37$ J K^{-1} mol^{-1}), where R is the gas constant. The molecular plane of each molecule was not perpendicular to the stacking axis *c*. The angles between the molecular long axes of AN and TCNQ and (100) plane were

estimated as 88.23 and 87.57 °, respectively. The angles between the molecular short axes of AN and TCNQ and (100) plane were estimated as 85.20 and 86.76 °, respectively. The inter-planer distance (3.45 Å) is smaller than that in the HT phase. The mixed-stack column at (0, 0, *z*) is related by the *a*-glide plane with that at (1/2, 1/2, *z*).

In the LT phase (100 K), the symmetry of the space group of AN–TCNQ is further lowered to *P*−1. Two independent mixed-stacked columns are present in the unit cell, where each molecule located in the inversion center (Figure 4c). In Figure 2.3.5c, the AN and TCNQ molecules of these columns are either blue AN and orange TCNQ (column A) or purple AN and yellow TCNQ (column B). In the LT phase, there is no orientational disorder of AN, suggesting that reorientational motion is suppressed. The magnitude of transition entropy also suggest order−disorder phase transition with two different orientations, $\Delta S = R \ln(1.82)$ (~$R \ln(2) = 5.76$ J K^{-1} mol^{-1}). The mixed-stack column at (0, 0, *z*) is no longer related with that at (1/2, 1/2, *z*). They are completely independent to each other. The molecular plane of each molecule was further titled to the stacking axis *c* than in the IM phase. The angles between the molecular long axes of AN and TCNQ and (100) plane were estimated as 85.76 and 85.10 ° for the mixed-stack column at (0, 0, z) and 89.83 and 89.77 ° for the column at (1/2, 1/2, z). The angles between the molecular long axes of AN and TCNQ and (010) plane were estimated as 79.85 and 82.34 ° for the mixed-stack column at (0, 0, z) and 79.90 and 83.49 ° for the column at (1/2, 1/2, z).

By the phase transition from the IM phase to LT phase, the crystal tend to be twin because the crystal system was changed from monoclinic to triclinic. There are two kinds of twin domains (TDs) in the LT phase, which are called TD1 and TD2 in this thesis. The TD2 can be obtained by 180° rotation of TD1 about the reciprocal axis [0 1 0].

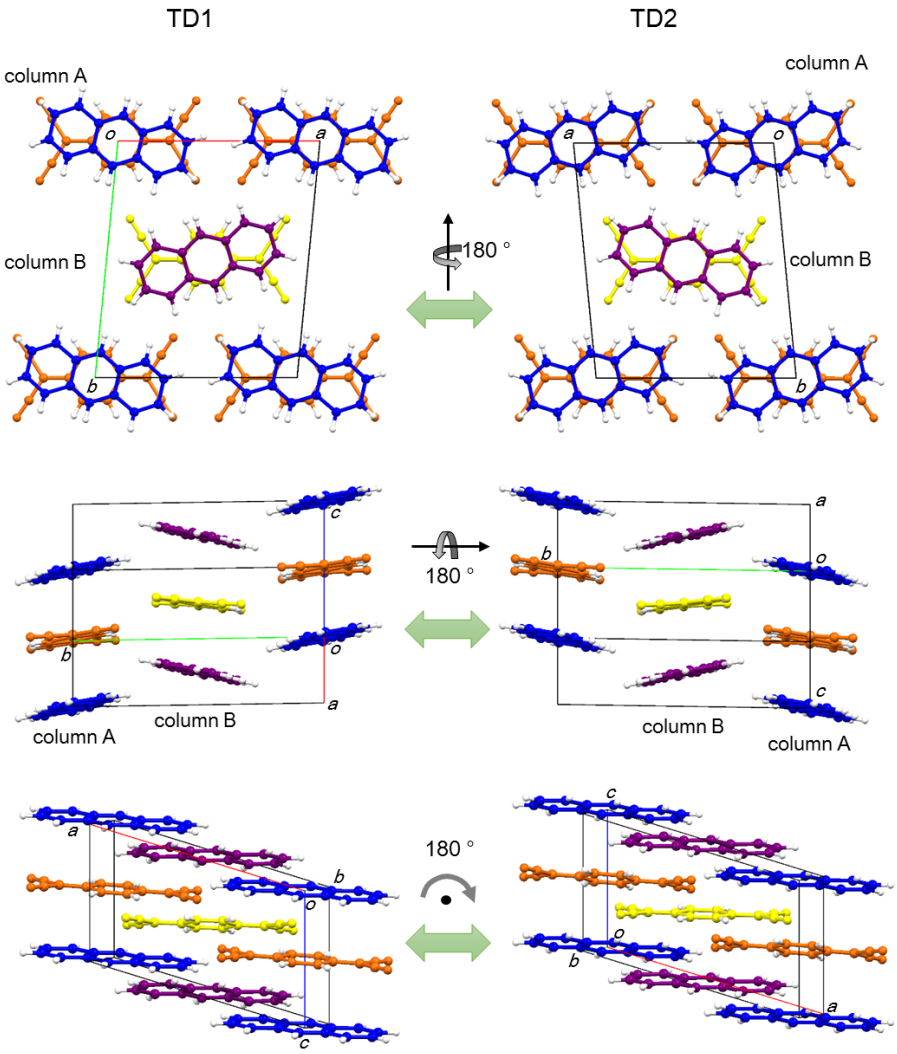

Figure 2.3.6. The relationship between TD1 and TD2.

It is considered that these TDs coexist randomly in the crystal, but, there are some limits of arrangement of these TDs with taking into account the crystal structure of the IM phase. In the IM phase, because the π-stack column at (0, 0, z) is related by the *a*-glide plane with that at (1/2, 1/2, *z*), the direction of deviation of AN molecule from the mirror plane is decided in each column (Figure 2.3.5b). Although the *a*-glide symmetry was absent in the LT phase, the direction might be kept also in the LT phase. In fact, the directions are different in column A and column B in the unit cell of the LT phase (Figure 2.3.5c). However, with considering the

twin law, 180° rotation about the b^* axis, the direction of column A (B) in TD1 and TD2 is different, respectively (Figure 2.3.6). The π -stack columns in the crystal are formed by the combination of the column A (B) of the TD1 and the column B (A) of the TD2, resulting in the coexistence of crystallographically independent two kinds of DA pairs in the column (Figure 2.3.7a). It is considered that the coexistence also occur along the *a* and *b* axes with the same reason (Figure 2.3.7b and c).

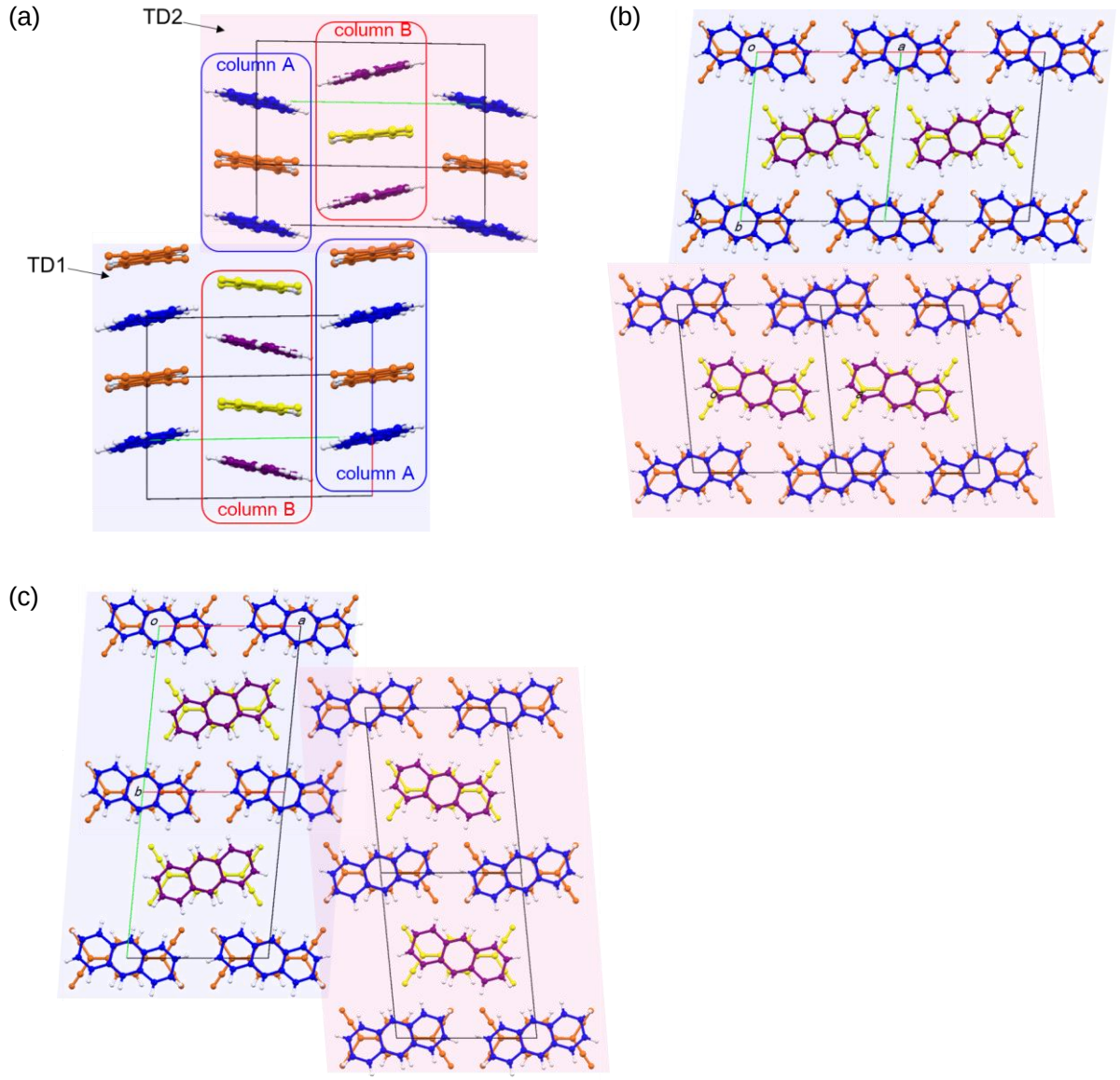

Figure 2.3.7 The twin boundaries considered in the LT phase along the (a) *c* axis, (b) *b* axis, and *a* axis.

Thus, the AN–TCNQ complex showed two structural phase transitions when the temperature decreased from room temperature to 100 K, and the reorientational motion of AN changed at the phase transition temperatures, resulting in twinning of the lattice.

2.3.4. Overlapping Modes

In this section, the molecular orbitals contributing to carrier transport and the CT degree between AN and TCNQ are discussed based on the geometry obtained from the X-ray structure analyses. As shown in Figure 2.3.5, there are three overlapping modes (OMs) of AN and TCNQ molecules in the HT phase, two OMs in the IM phase, and two OMs in the LT phase. Thus, there are a total of seven OMs. These seven OMs are called OM1 to OM7 (Figure 2.3.8). For these OMs, the overlap integrals between the LUMO of the TCNQ molecule and the HOMO or nHOMO of the AN molecule were calculated. The three molecular orbitals are illustrated in Figure 2.3.8a. The overlap integrals and molecular orbitals are summarized in Table 2.3.2.

Table 2.3.2. Overlap Integral of Each Overlapping Mode (OM).

	overlapping mode	overlap integral (10^{-3}) HOMO–LUMO
300 K	OM1, 3	3.5
(HT phase)	OM2	14.3[a]
155 K	OM4	5.7
(IM phase)	OM5	0.9
100 K	OM6	8.3
(LT phase)	OM7	8.7

[a]Overlap integral between nHOMO of AN and LUMO of TCNQ

In the HT phase, three OMs are exchanging in the molecular stacking column by

reorientational motion of the AN molecule. The two OMs in which the AN molecule is located out of the TCNQ mirror plane are called OM1 and OM3. In the OM2, both molecules are located in the mirror plane. According to the orthogonality of the HOMO of AN and LUMO of TCNQ, there is no CT interaction in OM2, which was also suggested by Wright.[12] We considered that the CT interaction in OM2 was generated between the nHOMO of AN and the LUMO of TCNQ. The overlap integral in OM2 is 14.3×10^{-3}. However, in OM1 and OM3, CT interaction occurs between the HOMO of AN and the LUMO of TCNQ because the molecular long axis of AN is not located on the TCNQ mirror plane. Because OM1 and OM3 are crystallographically equivalent, the overlap integral for both OM1 and OM3 is the same (3.5×10^{-3}).

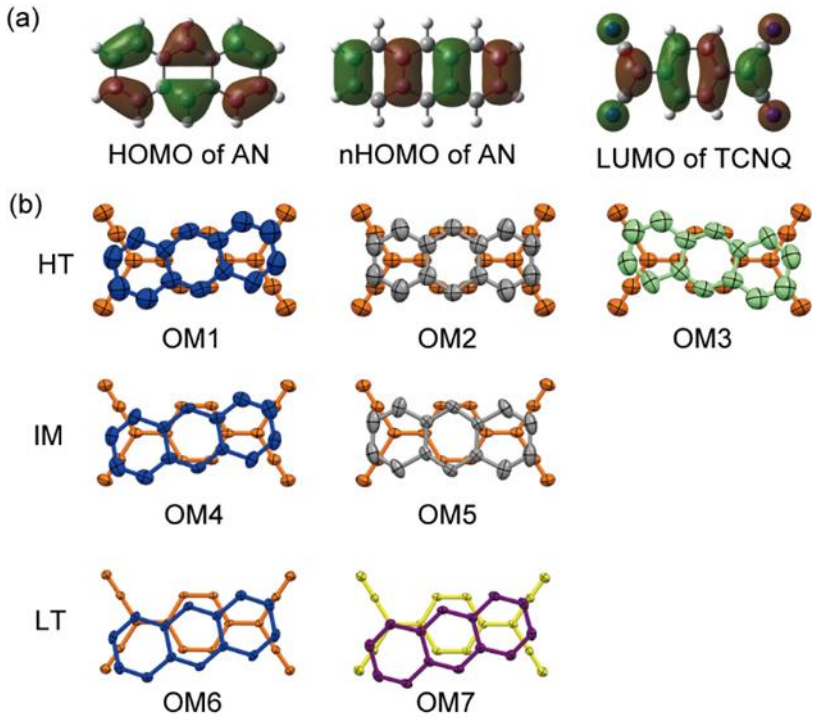

Figure 2.3.8. (a) HOMO and nHOMO of the AN molecule, and the LUMO of the TCNQ molecule, which were calculated at the DFT-B3LYP/6-31G(d,p) level. (b) Top views of AN and TCNQ overlap at 300, 155, and 100 K. The ellipsoids are drawn at the 50% probability level.

In the IM phase, there are two OMs (OM4 and OM5) in the crystal. The two OMs are exchanging in the stacking column by reorientation motion of AN. The OM4 is similar to OM1 and OM3, in which the each molecular long axis are crossed. In this OM, a large overlap integral between the HOMO of AN and the LUMO of TCNQ is observed (5.7×10^{-3}). In OM5, the molecular long axes are almost parallel. Although this relative arrangement looks the same as OM2, a non-zero overlap integral between the HOMO of AN and the LUMO of TCNQ is generated in OM5 (0.9×10^{-3}) since the mirror symmetry was extinct in the IM phase.

In the LT phase, the AN molecule does not show orientational disorder. Two OMs (OM6 and OM7) occur for the two crystallographically independent columns. Reorientation from OM6 to OM7 does not occur in a column. Both of the OMs are similar to OM1, OM3, and OM5. The overlap integrals of OM6 and OM7 are 8.3×10^{-3} and 8.7×10^{-3}, respectively.

Table 2.3.3. Averagd Bond Lengths and the Estimated Degrees of CT.

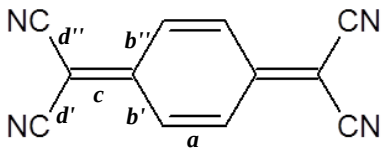

	TCNQ[14]	Rb–TCNQ[15]	AN–TCNQ			
T / K	room temp.	Room temp.	300 K	155 K	100 K (1/2, 1/2, *z*)	100 K (0, 0, *z*)
a / Å	1.346(3)	1.373(4)	1.3368(19)	1.3404(14)	1.3457(22)	1.3401(23)
b / Å	1.448(4)	1.423(4)	1.4386(11)	1.4412(8)*	1.4427(14)*	1.4440(13)*
c / Å	1.374(3)	1.420(4)	1.3749 (20)	1.3727(14)	1.3788(23)	1.3735(20)
d / Å	1.441(3)	1.416(4)	1.4307(13)	1.4314(8)*	1.4335(15)*	1.4346(15)*
c/(***b***+***d***)	0.476	0.500	0.4792	0.4779	0.4794	0.4771
Predicted CT	0	1	0.13	0.08	0.14	0.05

****b*** and ***d*** values are average of ***b'*** and ***b''*** and ***d'*** and ***d''***, respectively.

It is well known that the degree of CT of TCNQ complexes can be estimated roughly by the

geometry of TCNQ.[13] The participation of an electron in the LUMO of TCNQ should cause the two double bonds (***a*** and ***c***) to be weakened, and thus their bond lengths to increase. Likewise the bond lengths of ***b*** and ***d*** should decrease. Kistenmacher et al. suggested a method to estimate the degree of CT based on the ratio ***c***/(***b***+***d***). They assumed a linear relationship between the ratio and degree of CT, using the geometry of pristine TCNQ[14] and Rb–TCNQ[15] as the reference value of $TCNQ^0$ and $TCNQ^{-1}$, respectively. Table 2.3.3 lists the bond length of TCNQ and the degree of CT in each temperature. The degree of CT in the bulk did not significantly change through the two phase transitions. It should be noted that AN–TCNQ takes a neutral ground state in all the phases. The difference between the oxidation potential of AN and the reduction potential of TCNQ (ΔE = 1.2 V) indicates that the electronic state of the complex situates far from the neutral-ionic boundary defined by Torrance.[16] Therefore, it is reasonable that the degree of CT determined from the structural analysis of the balk crystal is nearly zero in all the phases. However, as shown below, a small but important ionic contribution was found to exist.

2.3.5. Ionic Domain in the Crystal

Optical measurements were taken to investigate the electronic state at low temperature. Figure 2.3.9a shows the temperature dependence of the reflectivity in the UV/vis and near-IR region with the electric field of light parallel to the π-stacking direction along the *c* axis (perpendicular to the molecular planes). The CT transition from the HOMO of AN to the LUMO of TCNQ (indicated by ♦ in Figure 2.3.9a) occurs at around 1.5 eV and that from the nHOMO to the LUMO (□ in Figure 2.3.9a) occurs at around 2.6 eV. The intensity of the former peak greatly increases below the second phase transition with decreasing temperature. The transition from the nHOMO to the LUMO shifts to lower energy below the first phase transition with decreasing temperature. Figure 2.3.9b shows the spectra with light perpendicular to the

stack (*c* axis). In the spectra, a weak peak corresponding to transition from the single-occupied molecular orbital to the LUMO of $TCNQ^{-1}$ (LUMO to next LUMO of TCNQ) is observed around 2.5 eV.[17] This peak might indicate the existence of ionic domains in the crystal even at room temperature. Below 140 K, the peak intensity markedly increases. These results indicate that the electronic state changes at the phase transitions and the ionic character are clearer in the LT phase than in the HT phase.

The degree of CT was investigated by IR spectroscopy. Figure 2.3.9c shows the temperature dependence of the reflectivity around 2200 cm^{-1} with the electric field of light perpendicular to the stack (*c* axis). The observed peaks are caused by the IR-active CN stretching (b_{1u}) mode of TCNQ polarized along the long molecular axis. The frequency is known to closely depend on the degree of CT (ρ).[18] As the temperature decreases below 200 K, the single band located at 2218 cm^{-1} splits into two bands, and the lower frequency (higher frequency) band shifts to lower (higher) frequency. This indicates that two types of TCNQ molecules with different ρ values are generated. The blue and red broken lines in Figure 6c show the frequencies of the CN stretching mode for $TCNQ^0$ and $TCNQ^{-1}$ determined from the IR spectra of TCNQ and K-TCNQ crystals, respectively.[18, 19] With lowering temperature, the CN stretching mode of $TCNQ^{-1}$ shows a slight higher-frequency shift.[19] We assumed the same magnitude of the temperature-dependent shift for the mode of $TCNQ^0$. We determined the ρ values using these two lines assuming a linear relationship between ρ and the frequency, and ρ is plotted as a function of temperature in Figure 2.3.9d. Below 200 K, two ρ values appear. As the temperature decreases, the larger value of ρ gradually increases (reaching 0.49 at 20 K), while the smaller value of ρ remains almost constant (~0.25-0.3). These optical measurements suggest that the electronic structure of AN–TCNQ drastically changes at the two phase transitions. Because of large molecular dynamics and one-dimensional fluctuation, a small number of ionic domains

are present even at room temperature. Thus, the electronic structure of AN–TCNQ is rather complicated because of the molecular dynamics in the crystal.

The magnetic susceptibility also indicates the presence of fractional ionic domains in the AN–TCNQ crystal (Figure 2.3.9e). Although the magnetic susceptibility of typical neutral mixed-stacked CT complexes only show Curie behavior originating from impurities or defects, the magnetic susceptibility of AN–TCNQ shows a paramagnetic contribution with an anti-ferromagnetic interaction around the phase transition from the HT to the IM phase. This result indicates the presence of ionic domains in the HT and IM phases of the AN–TCNQ crystal. The blue and red dotted lines in Figure 6e show Curie and singlet–triplet fitting, respectively. Fitting function is as follows:

$$\chi = \frac{Ng^2\beta^2}{k_B T\left[3+\exp(|J|/k_B T)\right]} + \frac{C}{T}$$

where N stands for the number of the spins, β is the Bohr magneton, k_B is the Boltzmann constant, J is the exchange magnetic interaction, and C is the Curie constant. The Curie constant obtained by fitting was 1.906×10^{-4} emu K mol^{-1} (the spin density was 0.5%), indicating that the Curie component originated from lattice defects. The exchange interaction $|J/k_B|$ and the spin density of the singlet–triplet component were 539 K and 2%, respectively.

Thus, the presence of ionic pairs has been confirmed by optical and magnetic measurements. In the HT and IM phases, the proportion of ionic pairs is 2%. Although the actual number of ionic pairs is difficult to estimate in the LT phase, the results of optical measurements indicate that the density of ionic species gradually increases with decreasing temperature.

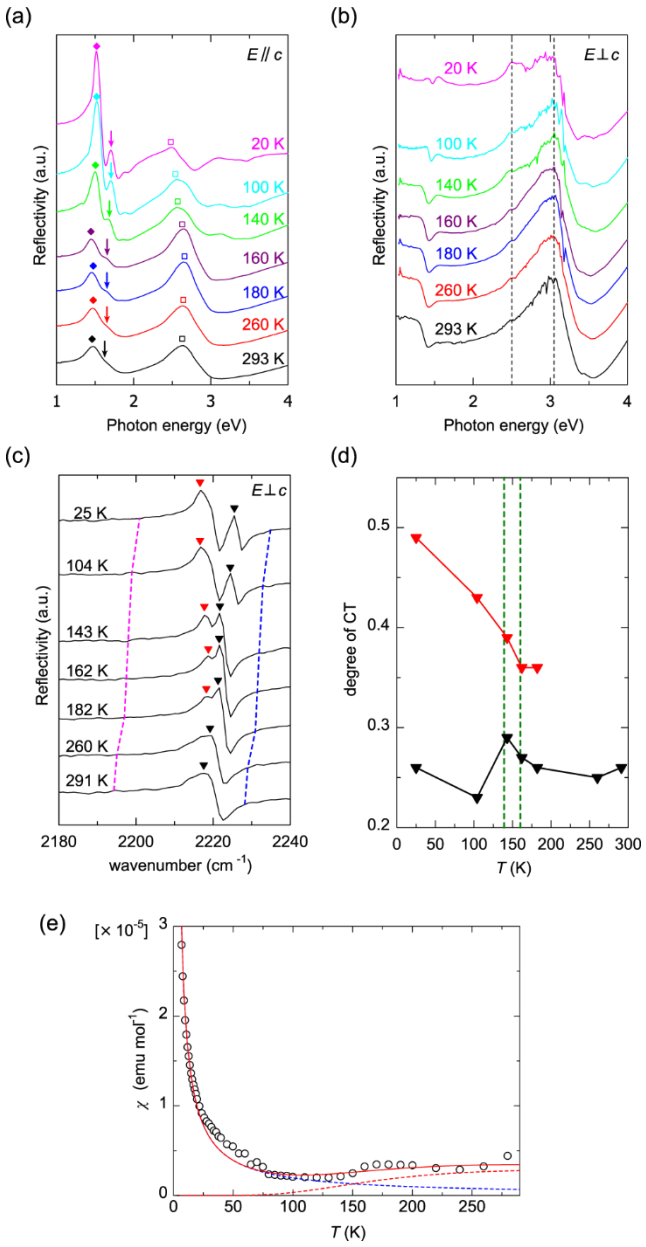

Figure 2.3.9. Temperature dependence of the reflectivity spectra of AN–TCNQ polarized (a) parallel to the stack *c* axis and (b) perpendicular to the stack *c* axis. (c) Temperature dependence of the IR reflectance spectra. The polarization direction was perpendicular to the stack *c* axis. The blue and red broken lines show the frequencies of the CN stretching mode of $TCNQ^0$ and $TCNQ^{-1}$ at each temperature determined from the IR spectra of TCNQ and K–TCNQ crystals, respectively. (d) Temperature dependence of the degree of CT in AN–TCNQ. The black and red triangles are the degree of CT calculated using the frequency of CN stretching in the IR spectra (black and red triangles in (c), respectively). (e) Magnetic susceptibility of AN–TCNQ. The red dotted line is singlet–triplet fitting, the blue dotted line is Curie fitting, and red solid line is the sum of these two components.

2.3.6. Relationship between the Device Property and Dynamics

Here, we discuss the relationship between the transfer characteristics and molecular dynamics of AN–TCNQ. The I_{SD} values of the AN–TCNQ FET at V_G = 100, 0, and −100 V are plotted against the reciprocal temperature in Figure 2.3.10. In the HT phase, the I_{SD} value at V_G = 100 V, which is related to the n-type character, decreases with thermally activated behavior. The thermal activation energy is estimated to be about 0.37 eV. In the IM phase, the activation energy decreases to 0.10 eV, which is considered to be because of the enhancement of the overlap integrals between AN and TCNQ molecules. In the HT phase, the I_{SD} value at V_G = −100 V, which is related to p-type behavior, is almost independent of temperature.

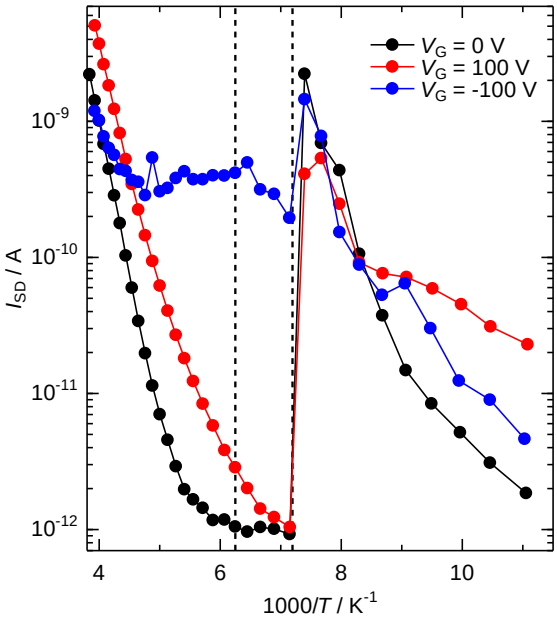

Figure 2.3.10. Temperature dependence of I_{SD} with V_G = 0 (black), 100 (red), and −100 V (blue). The two dashed lines indicate the transition temperatures.

In the IM phase, the current gradually decreases with decreasing temperature. Around the phase transition from the IM to the LT phase, both of the I_{SD} values greatly increase. This is considered to be caused by an increase of the ionic domains at the phase transition. After the large increase of the current, the current decreases in accordance with thermal activation. These

results indicate that the transport mechanism of the injected holes is different to that of electrons in the HT and IM phases of AN–TCNQ. From the thermally activated behavior, the electron transport mechanism is considered to be hopping between the LUMOs of TCNQ.[20] However, the hole is considered to transport through AN's HOMOs and nHOMOs, which are converting by the reorientational motion of the AN molecule. Thus, the molecular orbitals of the hole transport are dynamically disordered. It is considered that the current in disordered systems flows without temperature dependence.[21]

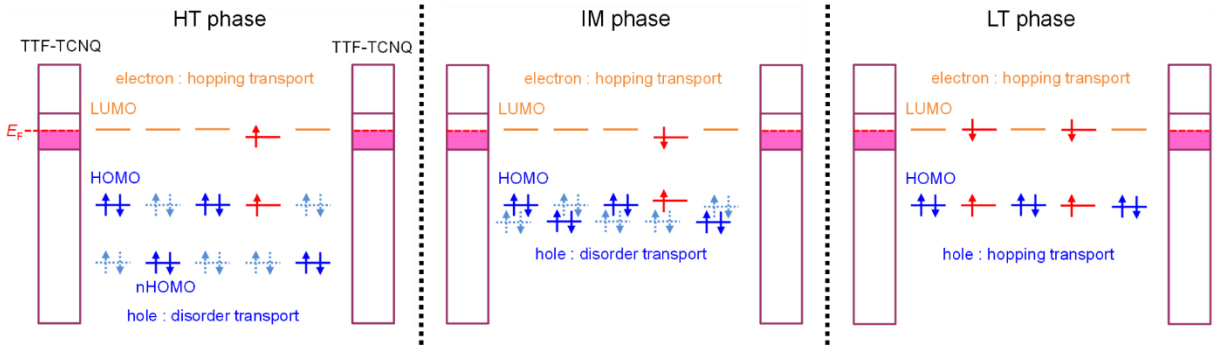

Figure 2.3.11. Schematics of the interfaces between the TTF–TCNQ electrodes and AN–TCNQ single crystal in each phase.

From these results, the mechanism for the drastic changes of the transfer characteristics of the AN–TCNQ-based FET can be speculated as follows. Schematics of the interface between the TTF–TCNQ electrodes and the AN–TCNQ single crystal in each phase are shown in Figure 2.3.11. The band widths of AN–TCNQ, which were calculated in extended Hückel approximation, are quite narrow because of their mixed-stacked arrangement (Figure 2.3.12). Therefore, I considered that the carrier transport in the AN–TCNQ crystal occur by hopping between their molecular orbitals (valence levels which mainly composed of HOMO or nHOMO of AN for holes and conduction levels which mainly composed of LUMO of TCNQ for electrons).

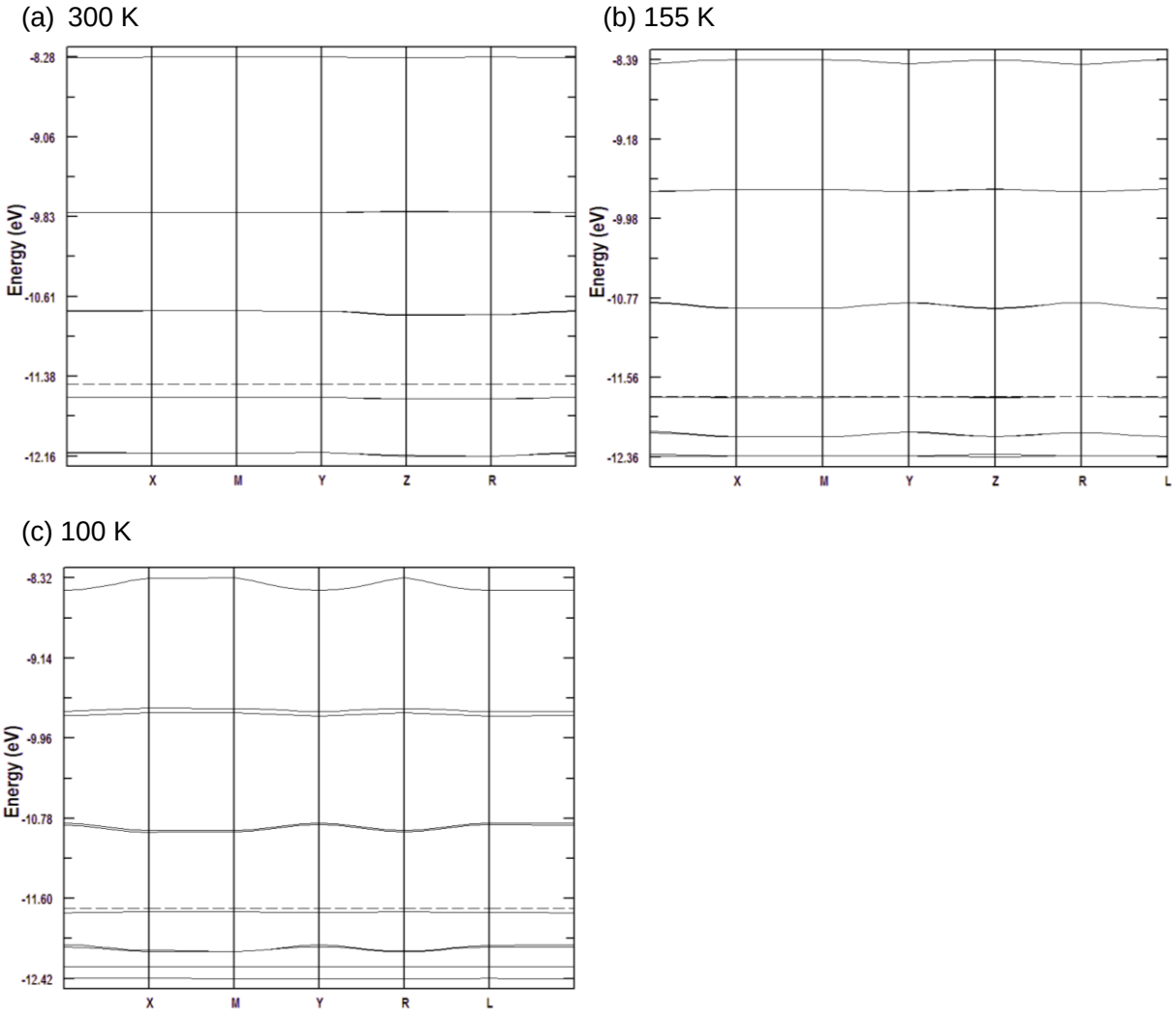

Figure 2.3.12 Band structure of AN-TCNQ at (a) 300 K (HT-phase, the orientation of AN is that of OM2), (b) 155 K (IM phase, the orientation of AN is that of OM4), and (c) 100 K (LT phase).

Because TTF–TCNQ used for the electrodes material contains the TCNQ molecule, the Fermi level of the electrodes is located near the LUMO of TCNQ in AN–TCNQ. In addition, there are ionic pairs in AN–TCNQ throughout the temperature range considered. The orbitals of the ionized pair might be stabilized because of one-dimentional fluctuation and reorientational motion of AN. Based on these aspects, the energy diagram of the HT phase is shown in Figure 2.3.11. At room temperature, the dominant carrier is electrons, which are

injected into the LUMO of TCNQ because of the relationship between the Fermi level of the electrode and the energy levels of the semiconductor. Thus, the transfer characteristics at room temperature show n-type behavior (Figure 2.3.3a). At this temperature, very few holes are injected into the semiconductor crystal. However, the p-type characteristic might be masked by the large n-type contribution. The injected electrons are strongly trapped at ionized and/or crystal defect sites, which cause thermal activation. At this time, the ionized site does not become a hole trap, because molecular orbitals participating in the CT interaction are disordered by reorientational motion of AN. As a result, p-type behavior is uncovered below 250 K (Figure 2.3.3b-d). In the IM phase, the reorientational motion of the AN molecule remains. The dominant carrier becomes holes, and the two HOMO levels in Figure 2.3.11 represent the two OMs with different transfer energies in the IM phase (Figure 2.3.3e). However, energy disorder is lowered, because the nHOMO of AN cannot contribute to hole transport. In the LT phase, reorientational motion stops. The mechanisms of both hole and electron transport follow the hopping model. The carriers are mainly transported on the LUMO of TCNQ because of the relationship between the Fermi level of the electrode and the energy levels of the semiconductor. However, slight hole transport is permitted, because the orbital of the ionic pair changes the trap into a molecular orbital for hole transport (Figure 2.3.3f). The large increase of I_{SD} at the transition temperature is caused by an increase of the overlap integral and carrier density associated with the phase transition.

Overall, the AN–TCNQ single-crystal FET with molecular dynamics and charge fluctuation shows drastic changes with decreasing temperature. The results and discussion in this paper might be useful for fabricating devices that can be switching between n-type and p-type. Furthermore, investigation of the device characteristics of the FET has been shown to be a useful method to clarify the band and electronic structures of semiconductor materials.

2.4. SUMMARY

A FET was fabricated using an AN–TCNQ single crystal, which underwent two phase transitions related to in-plane reorientational motion. The transfer characteristics drastically changed when decreasing the temperature from room temperature to 90 K: n-type → ambipolar-type → p-type → ambipolar-type.

Two reversible structural phase transition was confirmed by DSC measurements and single crystal X-ray analyses. In the HT phase, three orientations of AN were observed, which exchange by in-plane reorientational motion. The number of the orientation was lowered to two in the IM phase and disorder was not observed in LT phase, indicating that the reorientational motion of AN was changed by phase transitions and suppressed in the LT phase.

The electron and hole transport paths in the AN–TCNQ FET were different in the HT phase because of the molecular motion. The electron transport was hopping-type transport, while holes were transported disordered orbital by reorientational motion of AN molecules, resulting in gradual change of transfer characteristic from n-type to p-type with decreasing temperature. Ambipolar behavior in the LT phase is considered to be caused by the presence of ionic pairs in the crystal from the optical measurements. The ionic pair became the trap site in the high-temperature region, while it was involved in carrier transport in the low-temperature region.

This work showed that molecular dynamics in crystals can induce drastic changes in device properties. This work also showed that transport characteristics can be used to determine the change of molecular overlap and electronic structure. A detailed study of the FET characteristics is useful for both device design and investigation of the electronic structure or molecular dynamics.

2.5. REFERENECES

1. Lefebvre, J.; Odou, G.; Muller, M.; Mierzejewski, A.; Luty, T. *Acta Crystallogr. Sect. B Struct. Sci.* **1989**, 45, 323–336.
2. Fyfe, C. A. *J. Chem. Soc., Faraday Trans. 2* **1974**, 70, 1633−1641.
3. Fyfe, C. A.; Harold-Smith, D.; Ripmeester, J. *J. Chem. Soc., Faraday Trans. 2* **1976**, 72, 2269−2282.
4. Herbstein, F. H. *Crystalline Molecular Complexes and Compounds*; Oxford University Press: Oxford, U.K., **2005**; Vol. 2, Chapter 16.
5. Williams, R. M.; Wallwork, S. C. *Acta Crystallogr. Sect. B Struct. Crystallogr. Cryst. Chem.* **1968**, 24, 168–174.
6. Sheldrick, G. M. *Acta Crys-tallogr., Sect. A* **2008**, 64, 112−122.
7. Hoffmann, R. *J. Chem. Phys.* **1963**, 39, 1397.
8. Whangbo, M.-H.; Hoffmann, R.; Woodward, R. B. *Proc. R. Soc. A Math. Phys. Eng. Sci.* **1979**, 366, 23–46.
9. Ren, J.; Liang, W.; Whangbo, M.-H. *CAESAR*; Prime-Color Software, Inc.: Raleigh, NC, 1998.
10. Frisch, M. J.; Trucks, G. W.; Schlegel, H. B.; Scuseria, G. E.; Robb, M. A.; Cheeseman, J. R.; Scalmani, G.; Barone, V.; Men-nucci, B.; Petersson, G. A.; Nakatsuji, H.; Caricato, M.; Li, X.; Hratchian, H. P.; Izmaylov, A. F.; Bloino, J.; Zheng, G.; Sonnen-berg, J. L.; Hada, M.; Ehara, M.; Toyota, K.; Fukuda, R.; Hasegawa, J.; Ishida, M.; Nakajima, T.; Honda, Y.; Kitao, O.; Nakai, H.; Vreven, T.; Montgomery, J. A., Jr; Peralta, J. E.; Ogliaro, F.; Bearpark, M.; Heyd, J. J.; Brothers, E.; Kudin, K. N.; Staroverov, V. N.; Kobayashi, R.; Normand, J.; Raghavachari, K.; Rendell, A.; Burant, J. C.; Iyengar, S. S.; Tomasi, J.; Cossi, M.; Rega,

N.; Millam, N. J.; Klene, M.; Knox, J. E.; Cross, J. B.; Bakken, V.; Adamo, C.; Jaramillo, J.; Gomperts, R.; Stratmann, R. E.; Yazyev, O.; Austin, A. J.; Cammi, R.; Pomelli, C.; Ochterski, J. W.; Martin, R. L.; Morokuma, K.; Zakrzewski, V. G.; Voth, G. A.; Salvador, P.; Dannenberg, J. J.; Dapprich, S.; Daniels, A. D.; Farkas, Ö.; Foresman, J. B.; Ortiz, J. V.; Cioslowski, J.; Fox, D. J. Gaussian 09, Revision C.01; Gaussian, Inc.: Wallingford, CT, **2010**.

11. Bain, G. A.; Berry, J. F. *J. Chem. Educ.* **2008**, 85, 532.
12. Wright, J. D. *Molecular Crystals*, 2nd ed.; Cambridge University Press: Cambridge, U.K., **1995**.
13. Kistenmacher, T. J.; Emge, T. J.; Bloch, A. N.; Cowan, D. O. *Acta Crystallogr. Sect. B Struct. Crystallogr. Cryst. Chem.* **1982**, 38, 1193–1199.
14. Long, R. E.; Sparks, R. A.; Trueblood, K. N. *Acta Crystallogr.* **1965**, *18* (5), 932–939.
15. Hoekstra, A.; Spoelder, T.; Vos, A. *Acta Crystallogr. Sect. B Struct. Crystallogr. Cryst. Chem.* **1972**, *28* (1), 14–25.
16. Torrance, J. B.; Vazquez, J. E.; Mayerle, J. J.; Lee, V. Y. *Phys. Rev. Lett.* **1981**, 46 (4), 253–257.
17. Jonkman, H. T.; Kommandeur, J. *Chem. Phys. Lett.* **1972**, 15, 496–499.
18. Chappell, J. S.; Bloch, A. N.; Bryden, W. A.; Maxfield, M.; Poehler, T. O.; Cowan, D. O. *J. Am. Chem. Soc.* **1981**, 103, 2442–2443.
19. Okamoto, H.; Tokura, Y.; .Koda, T. *Phys. Rev. B* **1987**, 36, 7, 3858-3867.
20. Szu, S. M. *Semiconductor Devices: Physics and Technology*; **1985**.
21. Bässler, H. *Phys. status solidi* **1993**, 175, 15–56.

Chapter 3.

The Effect of Twinning by Structural Phase Transition for the Carrier Transport Property.

3.1. INTRODUCTION

The performances of OFETs were improved by using chemically-modified various molecules, because their performances strongly depend on the molecular orientation and electronic state of organic crystal forming semiconductor layer (see chapter 1). Even though the same material was used as semiconductor layer, single-crystal transistors exhibit higher mobility than thin-film transistor, which is caused by the grain boundary resistance in the thin-film.[1, 2]

There is a possibility of twinning during crystal growth, which are called as the growth twins.[3] The origin of the growth twin is a perturbation (impurity, dislocation or other defects) during the crystal growth, or the coalescence of nano, micro or macro-crystals with a precise mutual orientation. Thus, the growth twin has clear boundaries between twin domains, which are usually the same lattice plane in both twin domains. On the other hand, it is generally known that a single crystal can also become twin, if the crystal system changes during phase transitions.[3] As mentioned in Chapter 2, FETs can detect the change of molecular motion and electronic state. In this chapter, I fabricated OFETs using CT complexes which show twinning

by phase transitions, and investigated whether the FETs can detect the change from single crystal to twinned crystal.

Two kinds of CT complexes, fluorene–TCNQ (FL–TCNQ) and tetracene–TCNQ (TET–TCNQ) were used as semiconductor layer in this study. FL and TET have weaker and stronger electron donating ability than AN, respectively.[4, 5] These two crystals of TCNQ complexes are monoclinic system with the space group *C*2/*m* and donor molecules are disordered, which are similar to the features observed in AN–TCNQ. By decreasing temperature, both the crystal systems of FL–TCNQ and TET–TCNQ change to triclinic by structural phase transitions. The temperature dependences of OFETs using each single crystal were measured and the relationship between the twinning and the property of the device was investigated in this chapter. The discussion includes comparison with the data of AN–TCNQ since these two crystals show similar structure to AN–TCNQ.

3.2. EXPERIMENTAL SECTION

3.2.1. Materials

FL, TET and TCNQ were purchased from Tokyo Chemical Industry Co., Ltd. and purified by vacuum sublimation. Single crystals of the FL–TCNQ and TET–TCNQ complexes were prepared by a co-sublimation method in a sealed vacuum glass tube (see chapter 2). The crystal structure of FL–TCNQ at room temperature was the same as that in a previous report.[6] The temperature of each zone was set as 180 °C (TCNQ), 80 °C (FL), 190 °C (TET) and 130 °C (crystal growth).

3.2.2. Device Fabrication

We used TTF–TCNQ metallic thin films as the source and drain electrodes (Figure 2.2.1). By thermal evaporation through shadow masks, metallic thin films were deposited on the (110) plane of each bulk single crystal. The two electrodes were arranged for the current to flow parallel to the molecular stacking axis of each crystal (*c* axis). A 0.5-μm layer of Parylene C was deposited as the gate dielectric layer (C_i = 5.1 nF/cm^2). Gold gate electrodes were then formed on the top of the insulator layer.

3.2.3. Crystallographic Study

All of the diffraction measurements were performed on a Bruker SMART APEX II ULTRA diffractometer with a TXS rotating anode (Mo Kα radiation, λ = 0.71073 Å) and multilayer optics. The data collection was carried out at 300 and 100 K using a DX-CS190LD N_2-gas-flow cryostat (Japan Thermal Engineering, Sagamihara, Japan). The temperature in the nozzle was kept constant within ±0.2 K during the measurement. Low-temperature measurements were

performed by cooling the same crystal. The structures were solved by direct methods (SHELXT) and refined by full-matrix least-squares on F^2 using SHELXL-2014.[7] All of the H atoms were refined using a riding model. For the crystal structures without disorder, all of the non-H atoms were refined anisotropically. For the crystal structures with disorder, disordere molecules were restrained to be the same structure each other (SAME restraint). The ADPs were also restrained by rigid bond restraints (RIGU restraint). The details of the refinement are provided in the Appendix as the SHELXL-2014 res files. The crystal and experimental data are summarized in Table 3.2.1.

Table 3.2.1 Crystallographic Data for Each Phase of FL–TCNQ and TET–TCNQ

	FL–TCNQ		TET–TCNQ	
	300 K	100 K	300 K	100 K
formula	$C_{25}H_{14}N_4$		$C_{30}H_{16}N_4$	
formula weight	382.41		432.47	
crystal size (mm^3)	0.45 × 0.43 × 0.40		0.45 × 0.22 × 0.20	
crystal system	monoclinic	triclinic	monoclinic	triclinic
space group	*C*2/*m*	$P\bar{1}$	*C*2/*m*	$P\bar{1}$
a (Å)	11.0034(9)	8.2094(10)	11.8966(10)	8.5947(14)
b (Å)	13.0967(11)	8.7608(11)	12.8846(11)	8.8204(14)
c (Å)	6.7931(6)	6.6384(8)	7.2567(6)	7.1458(11)
α (°)	90	98.6193(18)	90	88.956(2)
β (°)	103.5837(13)	98.4392(18)	90.1902(14)	87.577(3)
γ (°)	90	100.1572(17)	90	85.600(2)
V ($Å^3$)	951.56(14)	457.23(10)	1112.32(16)	539.57(15)
Z	2	1	2	1
R_{int}	0.0143	0.0262	0.0312	0.0289
R_1 [$I > 2\sigma(I)$]	0.0359	0.0306	0.0449	0.0339
R_w (all reflection)	0.1124	0.0917	0.1174	0.1008

3.2.4. Calculation

The overlap integrals between the highest occupied molecular orbital (HOMO) and next

HOMO (nHOMO) of each donor and the lowest unoccupied molecular orbital (LUMO) of TCNQ for each crystal were calculated under the extended Hückel approximation[8, 9] using the CAESAR program package.[10] The optimization and energy calculations of isolated single molecules were performed using Gaussian 09W at the B3LYP/6-31G(d,p) level.

3.2.5. Measurements

The device properties of the single-crystal FETs were measured using a dual channel system source meter (Keithley 2636A). Temperature was controlled using a closed cycle cryostat system. Thermal analyses were performed by differential scanning calorimetries (DSC) with a heating and cooling rate of 5 K/min. Mettler Toledo Thermal Analysis System, DSC 1 was used for FL-TCNQ and Rigaku DSC-8230 was used for TET-TCNQ. Diffuse reflectance UV-vis-NIR spectra were obtained diluting the sample in KBr powder (JASCO V-570 UV/VIS/NIR spectrophotometer). The spectra were converted to the Kubelka-Munk function.

3.3. RESULTS ANT DISCUSSION

3.3.1. DSC measurements

DSC measurements show no peak in the measured temperature range for both crystals (Figure 3.3.1). As mentioned below, structural phase transition occurs in both crystal. Thus, the phase transitions might be second order.

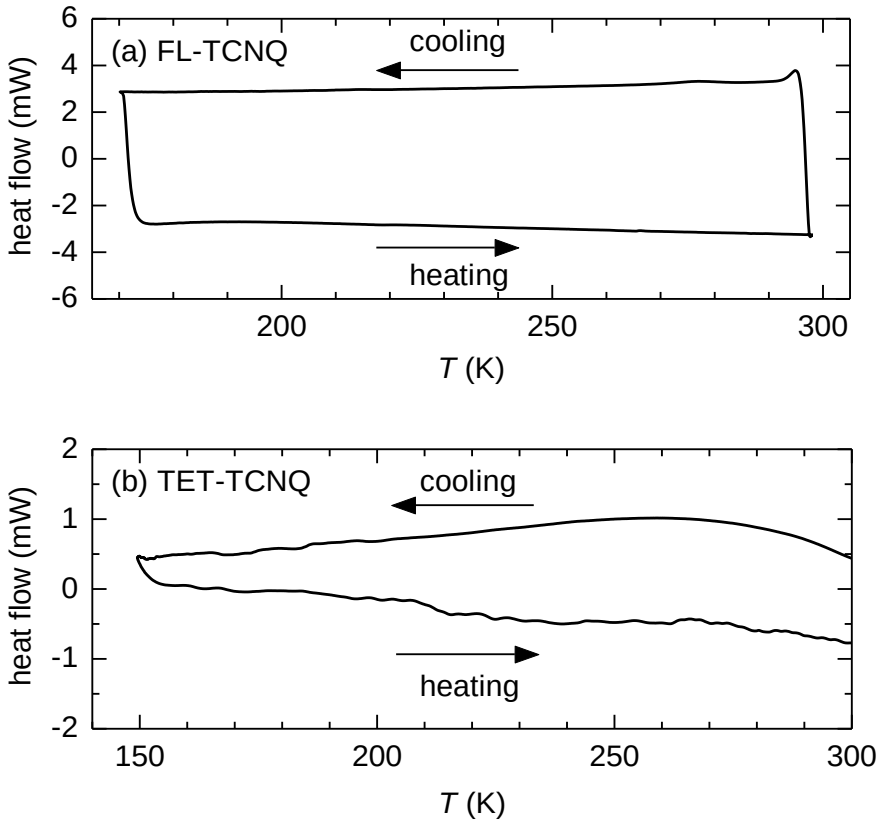

Figure 3.3.1 DSC profile of polycrystalline (a) FL–TCNQ and (b) TET–TCNQ.

3.3.2. Crystal Structure

The crystal structures of each crystal at 300 K and 100 K were determined by single-crystal X-ray structure analysis. Structural phase transition, which is accompanied with twinning, was observed in each crystal.

FL–TCNQ. At room temperature, the space group of the crystal obtained by co-sublimation is *C*2/*m*, which is the same structure as that the crystal grown by slow evaporation.[6] Each molecule is located on the 2/*m* site (Figure 3.3.2). We call it as the HT phase. The FL molecules were refined as the overlap of two different orientations, which were related to each other by the symmetry of the site. Thus, the occupancy was refined to be 50 % each other, and the two overlapping modes (OMs) are equivalent. According to the matching of the nodal structures of the HOMO of FL and LUMO of TCNQ, the overlap integral was estimated as a large value, 20.9×10^{-3}. The molecular planes of FL and TCNQ were perpendicular to the stacking axis *c* and the inter-planer distance was estimated as about 3.40 Å.

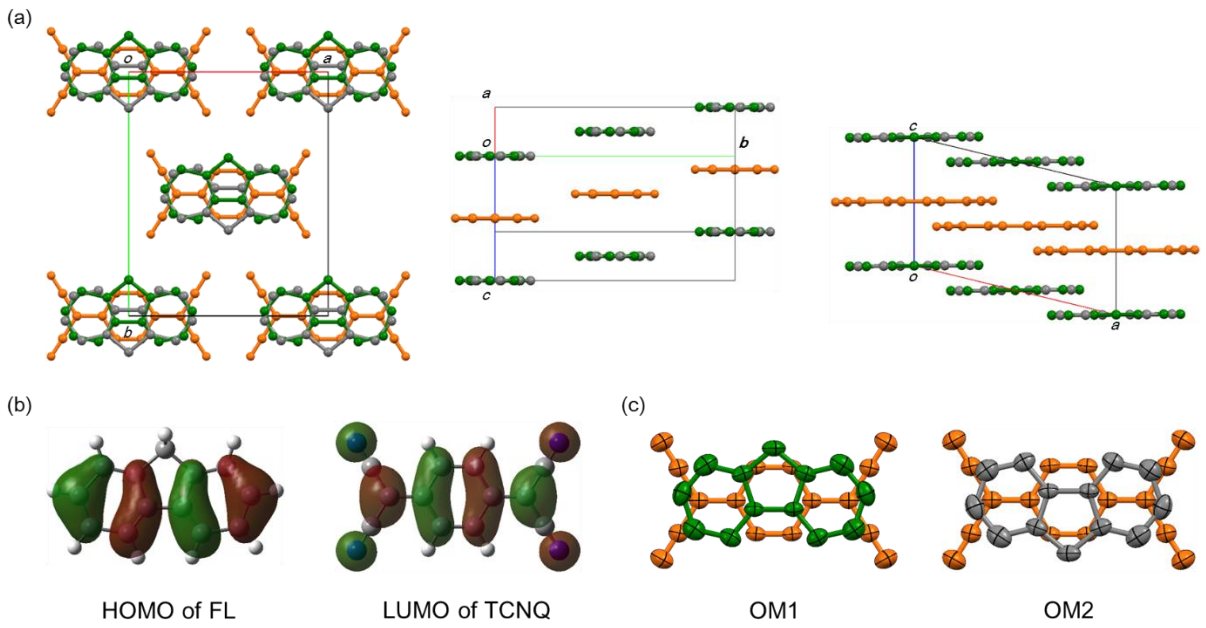

Figure 3.3.2. (a) Crystal structure of the HT phase. (b) HOMO of the FL molecule and the LUMO of the TCNQ molecule. (c) Top views of FL and TCNQ overlap at 300 K. The ellipsoids are drawn at the 50% probability level.

At 100 K, the symmetry of the space group of FL–TCNQ is lowered to *P*−1 with *Z* = 1, which indicates that a structural phase transition occurs (Figure 3.3.3). We call it as the LT

phase. Although the transition temperature cannot be determined correctly since peaks were not observed in the heat flow of the DSC, the lattice parameter changed gradually between 220-200 K and the phase transition was completed at 100 K. The unit cell axes were translated from the HT phase as follows; (*a*, *b*, *c*) → ((*a*-*b*)/2, (*a*+*b*)/2, *c*). Each molecule located at the inversion center of the unit cell. The orientational disorder of FL molecule was also observed at this temperature with 1:1 occupancy ratio, which is the same as the HT phase. This suggests that reorientation between them do not occur in this crystal in this temperature range. The two orientations of the disordered FL molecule are almost the same as that of room temperature, and the OMs are also similar to those in the HT phase. The molecular planes were almost perpendicular to the stacking axis *c* also in the LT phase. The inter-planer distance was shorter than that in the HT phase (3.32 Å), resulting in higher overlap integral (23.3×10^{-3}). The intra-column structure do not change largely by the phase transition.

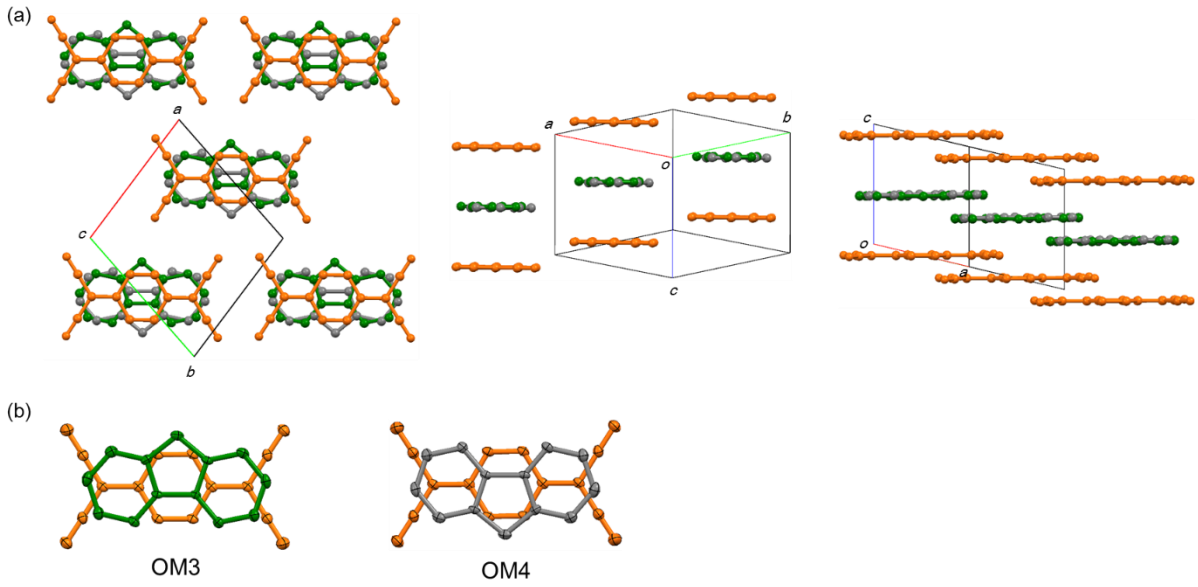

Figure 3.3.3. (a) Crystal structure of the LT phase. (b) Top views of FL and TCNQ overlap at 100 K. The ellipsoids are drawn at the 50% probability level.

The phase transition is related to the change of relative orientation between the columns. In

the HT phase, the π-stack column is related by the *a*-glide plane each other. By the phase transition, displacement of the π-stack column occur along the *a* axis of the HT phase, resulting in the loss of the monoclinic symmetry at the LT phase. In order to compare the lattice parameters between the HT and LT phases, the cell parameters of the LT phase were expanded by translation the axes with an operation (*a*, *b*, *c*) → ((*a*+*b*), (*a*-*b*), *c*) (Table 3.3.1). Because of the decreasing temperature, lattice parameters become shorter in the LT phase. The values of α and β are almost the same compared to those of the HT phase, on the other hand, the value of γ is largely deviated from that of the HT phase, which indicates that the displacement of π-stack column mainly occur along the *a* axis of the HT phase. In the HT phase, weak hydrogen bonds were formed between TCNQ molecules and TCNQ and FL molecules, respectively (Figure 3.3.4). In the LT phase, the displacement results in anisotropic hydrogen bonds, where the bond length along the *a* and *b* axes of the LT phase is different with each other. From these results, the phase transition is related to the change of inter-column relative orientation, which is considered as displacement along the *a* axis of the HT phase.

Table 3.3.1 Comparing the Cell Parameter of FL–TCNQ between HT and LT Phase

	FL–TCNQ	
temperature (K)	300	100*
crystal system	monoclinic	triclinic
space group	*C*2/*m*	$P\bar{1}$
a (Å)	11.0034	10.899
b (Å)	13.0967	13.020
c (Å)	6.7931	6.6384
α (°)	90	90.48
β (°)	103.5837	103.36
γ (°)	90	86.22

* The unit cell was obtained by translation the axes with an operation (*a*, *b*, *c*) → ((*a*+*b*), (*a*-*b*), *c*)

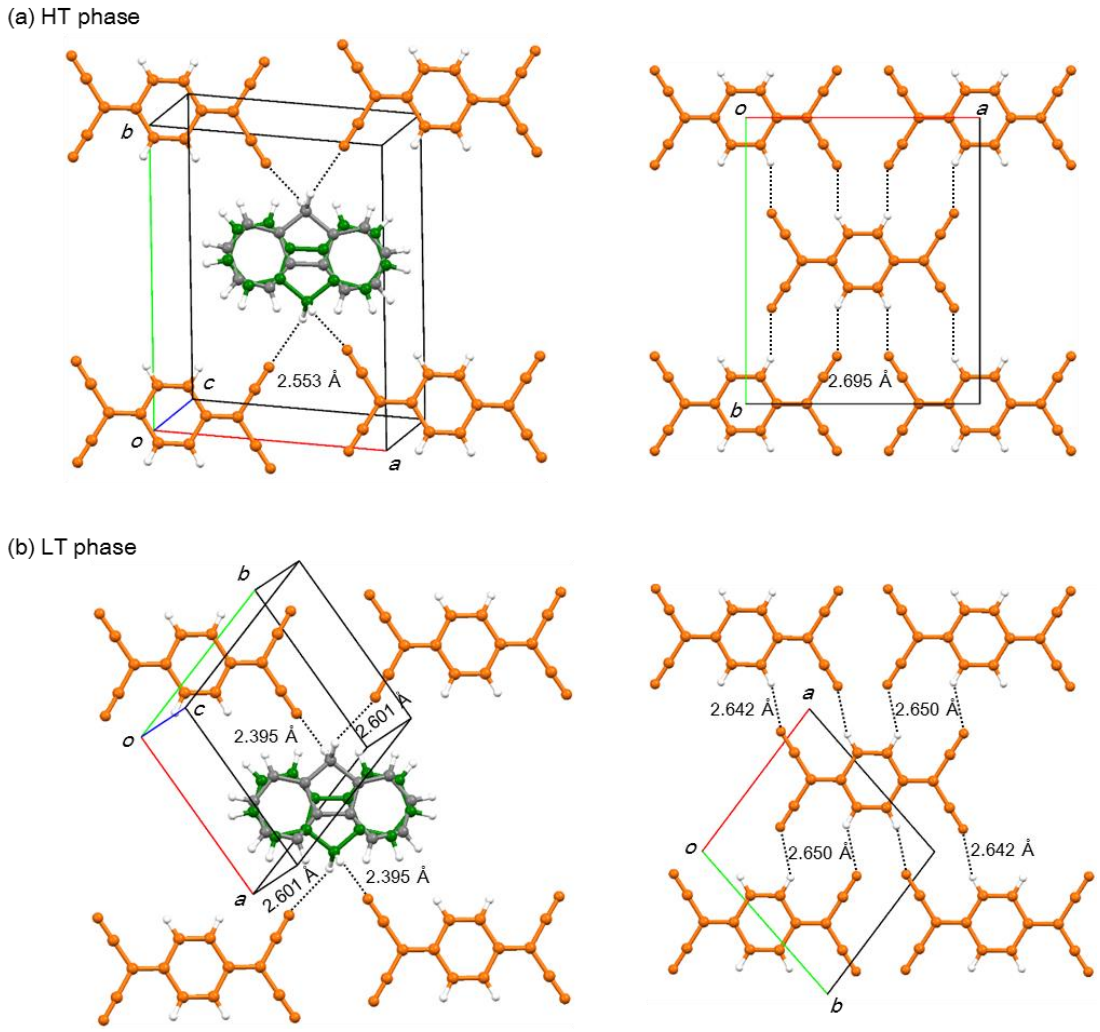

Figure 3.3.4. Hydrogen bonds in FL–TCNQ. (a) HT phase and (b) LT phase.

The crystal of FL–TCNQ complex become twin by phase transition from the HT phase to the LT phase. The twinned crystal is composed of two kinds of twin domains (TDs), which are called TD1 and TD2 in this thesis. The TD2 can be obtained by rotation of TD1 by 180° degrees about reciprocal axis [1 -1 0], which corresponds to the *b* axis of the HT phase. Such a kind of twinning always occurs more or less, when the crystal system changes. In the FL–TCNQ crystal, the twinning was caused by the change of crystal system from monoclinic to triclinic. The difference between TDs is mainly related to the direction of the displacement of the π-stack column (Figure 3.3.5). It is considered that the crystal is more disordered in the LT phase by

these TDs, which might affect the device properties.

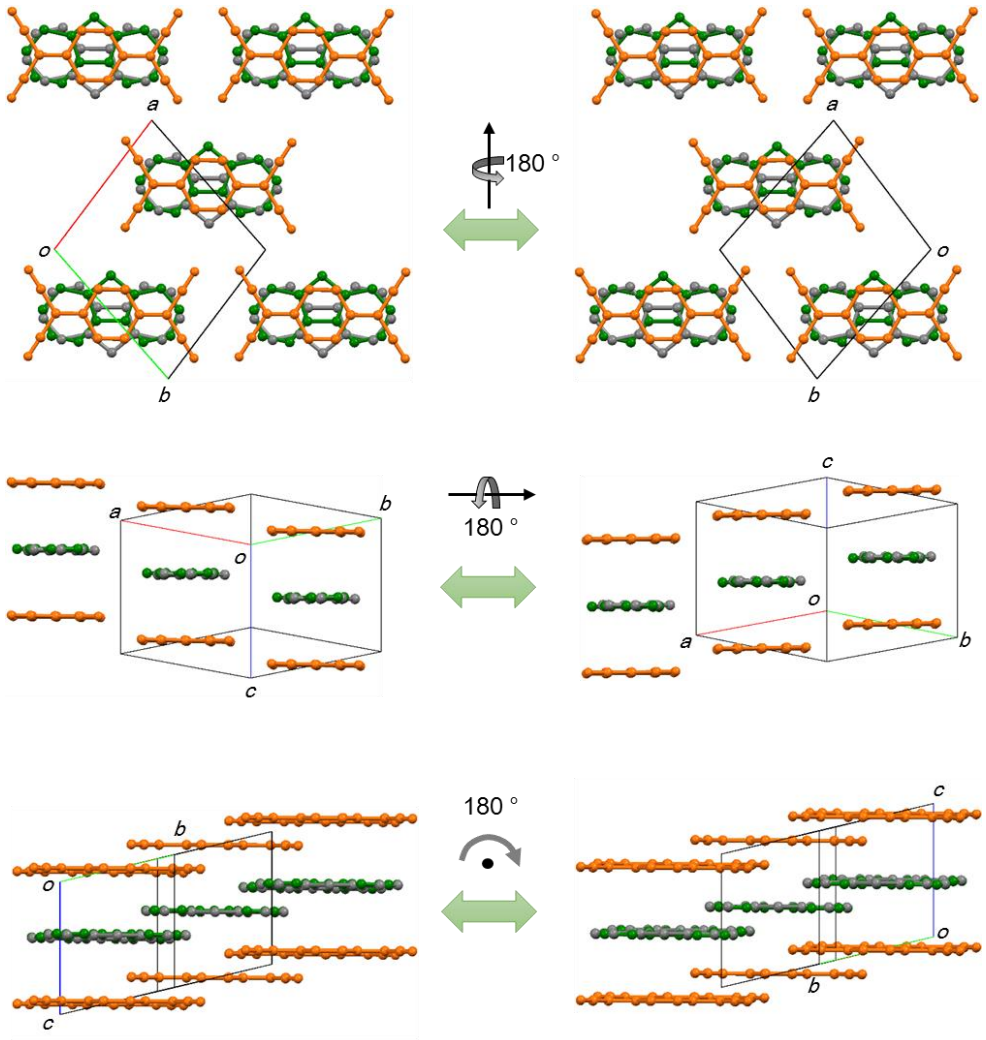

Figure 3.3.5. The TDs in the LT phase of FL–TCNQ.

TET–TCNQ. The space group of the crystal is also *C*2/*m*, and each molecule is located on the 2/*m* site (Figure 3.3.6). The TET molecules were refined as the overlap of three different orientations, two of which were related to each other by the symmetry of the site. In these two arrangements (purple and light green), the molecular long axes of TET significantly deviate from the mirror plane, while both TET (gray) and TCNQ (orange) share the same mirror plane in another arrangement, which is similar to the disorder observed in AN–TCNQ crystal. The

occupancies were refined to be 33(2) % (purple and light green TET) and 35(4) % (gray TET). In the HT phase, it is considered that exchanging of these three orientations occurs by in-plane molecular reorientation of TET. Although the crystal have the same space group as AN–TCNQ and FL–TCNQ, it is not an isomorphous structure because the molecules in the π-stack column are titled. The angles between the molecular planes of TET and TCNQ and the stacking axis *c* are estimated as 74.34 and 75.06 °, respectively. The inter-planer distance was estimated as 3.49 Å. All the mixed-stack columns are translationally related with each other.

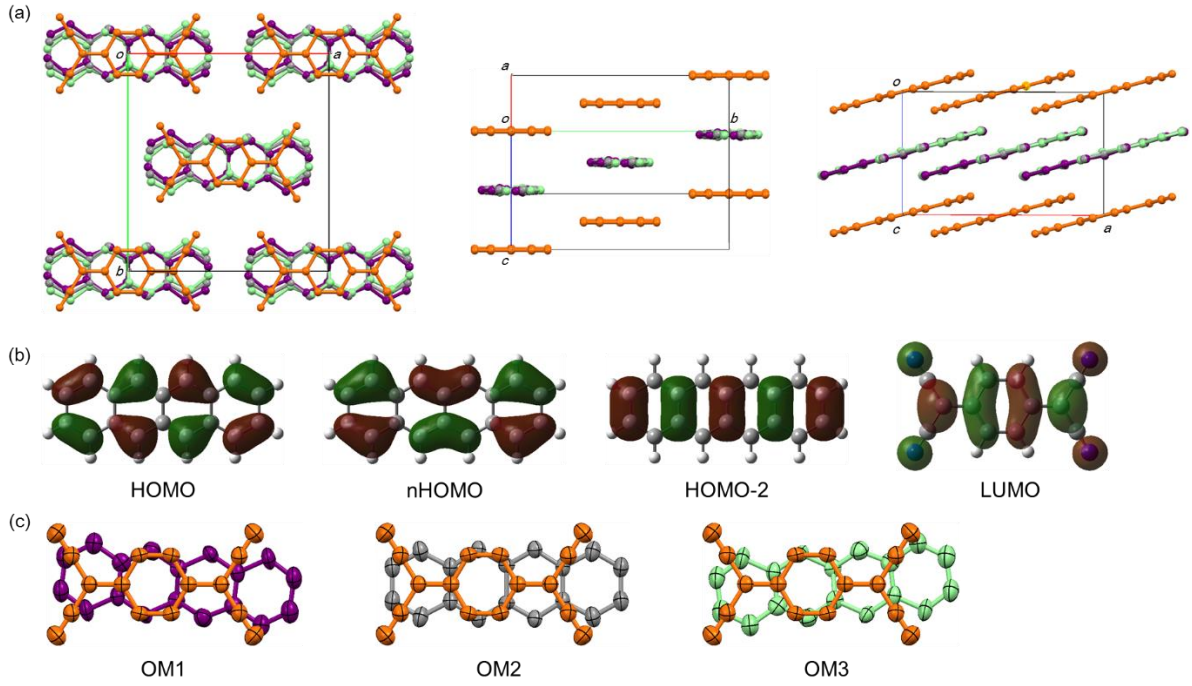

Figure 3.3.6. (a) Crystal structure of the HT phase. (b) HOMO of the FL molecule and the LUMO of the TCNQ molecule. (c) Top views of FL and TCNQ overlap at 300 K. The ellipsoids are drawn at the 50% probability level.

At 100 K, the symmetry of the space group of TET–TCNQ is lowered to $P\bar{1}$ with $Z = 1$, which indicates that a structural phase transition occurs also in this crystal (Figure 3.3.7). Although the transition temperature cannot be determined correctly since peaks were not

observed in heat flow of the DSC, the lattice parameter changed gradually between 185-180 K and the phase transition was completed at 100 K. The unit cell axes were translated from the HT phase to the LT phase by (a, b, c) → ((a-b)/2, (a+b)/2, c). Each molecule is located at the inversion center of the unit cell. The orientational disorder of TET molecule was not observed in the LT phase, suggesting that reorientational motion is suppressed. The inter-planer distance was estimated as 3.41 Å.

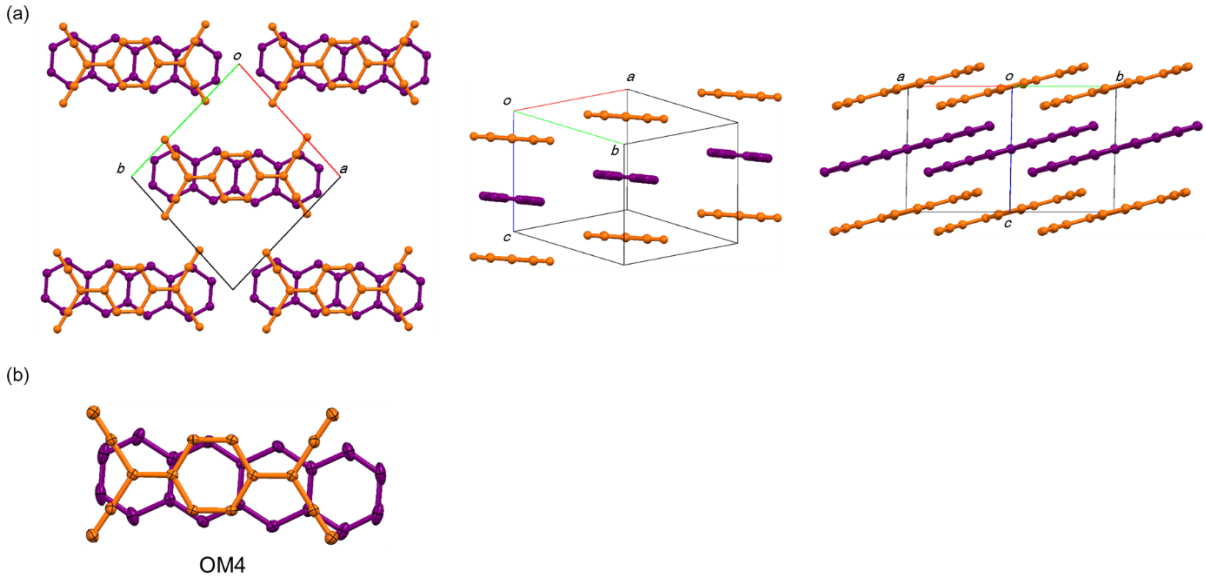

Figure 3.3.7. (a) Crystal structure of the LT phase. (b) Top views of FL and TCNQ overlap at 100 K. The ellipsoids are drawn at the 50% probability level.

In this complex, both the intra-column and inter-column displacements occur by the phase transition. In order to compare the lattice parameters between the HT and LT phases, the cell parameters of the LT phase were expanded by translation the axes with an operation (a, b, c) → ((a-b), (a+b), c) (Table 3.3.2). Compared to FL–TCNQ, the cell lengths show relatively small change, but the cell angles show relatively large changes by phase transition. In the LT phase, the angle between the molecular long axis of each molecule and the stacking axis c was not

changed largely (73.24 ° for TET and 74.06 ° for TCNQ). On the other hand, molecular short axis of each molecule was tilted to the *c* axis (85.37 ° for TET and 85.37 ° for TCNQ) in this phase, resulting in the relatively large change of α and β. In addition to intra-column displacement, the π-stack column displacement occurs along the *a* axis of the HT phase. The change of γ value of TET–TCNQ was smaller than that of FL–TCNQ, indicating that the magnitude of the displacement is smaller in this crystal.

Table 3.3.2 Compairing the Cell parameter of TET–TCNQ between HT and LT Phase

	TET–TCNQ	
temperature (K)	300	100*
crystal system	monoclinic	triclinic
space group	*C*2/*m*	$P\bar{1}$
a (Å)	11.8966(10)	11.834
b (Å)	12.8846(11)	12.779
c (Å)	7.2567(6)	7.146
α (°)	90	87.75
β (°)	90.1902(14)	89.02
γ (°)	90	91.49

*The unit cell was obtained by translation the axes with an operation (*a*, *b*, *c*) → ((*a*-*b*), (*a*+*b*), *c*)

The crystal of the TET–TCNQ complex become twin by phase transition from the HT phase (monoclinic) to the LT phase (triclinic). The twinned crystal is composed of two TDs, which are called TD3 and TD4 in this thesis. The TD4 can be obtained by rotation of TD3 by 180° degrees about reciprocal axis [0.043 0.955 1.000] and real axis [-0.002 0.999 1.000], which correspond to *a*+*b* axis of the LT phase (Figure 3.3.8).

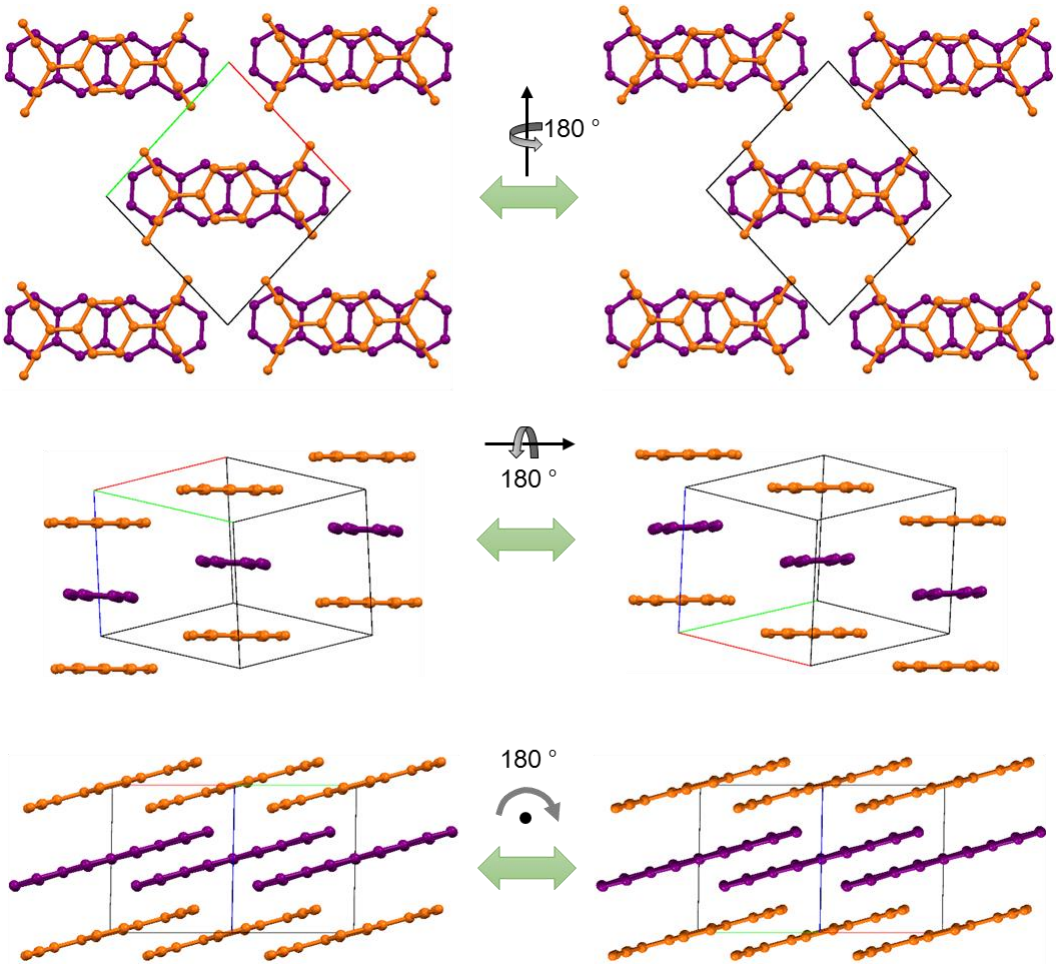

Figure 3.3.8. The TDs in the LT phase of TET–TCNQ.

The OMs in the HT phase are similar to those of AN–TCNQ. The two OMs in which the TET molecule is located out of the TCNQ mirror plane are called OM1 and OM3. In the OM2, both molecules are located in the mirror plane. According to the orthogonality of the HOMO of TET and LUMO of TCNQ, there is no CT interaction in OM2. In addition, CT interaction cannot occur between the nHOMO of TET and LUMO of TCNQ by the same reason (Figure 3.3.6b). In the OM2, CT interaction occur by the overlap between the HOMO-2 of TET and LUMO of TCNQ with the overlap integral 14.0×10^{-3}. In the OM1 and OM3, CT interaction can occur between the HOMO of TET and LUMO of TCNQ, even though the overlap integral is small (0.6×10^{-3}). These OMs can be exchanged by reorientational motion of TET. Thus, it

is considered that the transfer path of holes are disordered in the HT phase, which was observed in AN–TCNQ. In the LT phase, the orientational disorder was not observed and overlap integral of OM4 was estimated as 1.0×10^{-3}.

The degree of CT was estimated by using the ratio ***c***/(***b***+***d***) of TCNQ.[11] Table 3.3.3 lists the bond length of TCNQ and the degree of CT in each crystal. The degree of CT in the bulk did not significantly change through the phase transitions in both complexes.

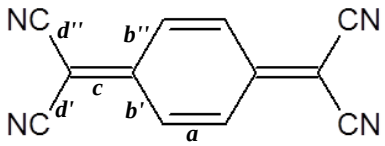

Table. 3.3.3. Estimation of the Degree of CT in FL–TCNQ and TET–TCNQ

	TCNQ	Rb–TCNQ	FL–TCNQ		TET–TCNQ	
T / K	room temp.	Room temp.	300 K	100 K	300 K	100 K
a / Å	1.346(3)	1.373(4)	1.3414(16)	1.3480(14)	1.3425(18)	1.3476(12)
b / Å	1.448(4)	1.423(4)	1.4423(9)	1.4427(8)	1.4356(10)	1.4434(8)
c / Å	1.374(3)	1.420(4)	1.3720(16)	1.3770(14)	1.3763(17)	1.3775(12)
d / Å	1.441(3)	1.416(4)	1.4296(10)	1.4301(8)	1.4296(14)	1.43415(8)
c/(***b***+***d***)	0.476	0.500	0.4777	0.4793	0.4804	0.4787
Predicted CT	0	1	0.07	0.14	0.18	0.11

3.3.3. Optical Measurements

In order to estimate the band gap of these two CT complexes, diffuse reflectance spectroscopy measurements were executed (Figure3.3.9). The optical band gap of FL–TCNQ and TET–TCNQ is estimated as 1.9 eV and 0.9 eV, respectively. The CT band of each complex is attributed to the transition from HOMO of each donor to LUMO of TCNQ. As shown in chapter 2, the optical band gap of AN–TCNQ was 1.4 eV. These values of optical band gap

show correlation with the half-wave oxidation potential ($E_{ox}^{1/2}$). Larger (smaller) band gap was observed in the complex with weaker (stronger) donor (Table 3.3.3).

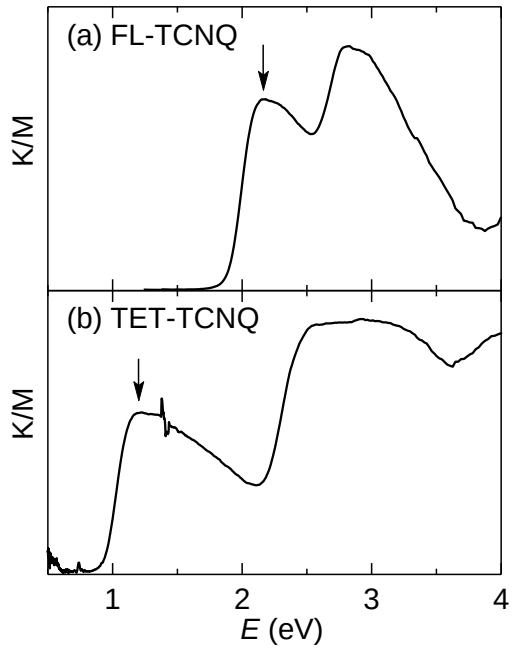

Figure 3.3.9. Diffuse reflectance spectra of (a) FL–TCNQ and (b) TET–TCNQ. The arrows indicate the CT band.

Table 3.3.3 Optical band gap of each complexes and half-wave oxidation potential of each donor.

	Optical band gap (eV)*	$E_{ox}^{1/2}$ (V)**
TET–TCNQ	0.9	0.77
AN–TCNQ	1.4	1.09
FL–TCNQ	1.9	1.55

***The values of optical band gap were obtained from the edge of each CT band.**

****ref [4] and [5]**

3.3.4. Field-Effect transistors of FL–TCNQ and TET–TCNQ

Figure 3.3.10 shows the device properties of the FL–TCNQ single-crystal FET in variable temperatures. The device showed n-type behavior at 300 K. The device exhibited normally on behavior, the threshold voltage (V_{th}) was −37.2 V. The mobility μ was estimated as 4.8×10^{-3}

$cm^2/(V \cdot s)$. The FET show lower V_{th} and higher μ compared to that using AN–TCNQ. The lower V_{th} indicate that the amount of thermally activated carrier is larger than that of AN–TCNQ. However the optical band gap of FL–TCNQ crystal is wider than that of AN–TCNQ since the overlap integral of the crystal is much larger than that of AN–TCNQ, indicating that there are larger amount of thermally activated carriers at room temperature. The higher μ can be also explained by the larger overlap integral.

The device showed n-type behavior at the temperatures below and above the phase transition. The Arrhenius plots of the mobility are shown in Figure 3.3.10d. Although the overlap integral is larger in the LT phase than in HT phase, the activation energy E_a of the mobility was gradually increased from 250 K to 200 K. At the higher and lower temperatures, the E_a values are estimated as 0.17 and 0.30 eV, respectively. It is considered that the increase of E_a is related to the phase transition. The crystal became twin from the HT to LT phase. The boundaries of TDs can be interpreted as defects, which cause the increase of E_a.

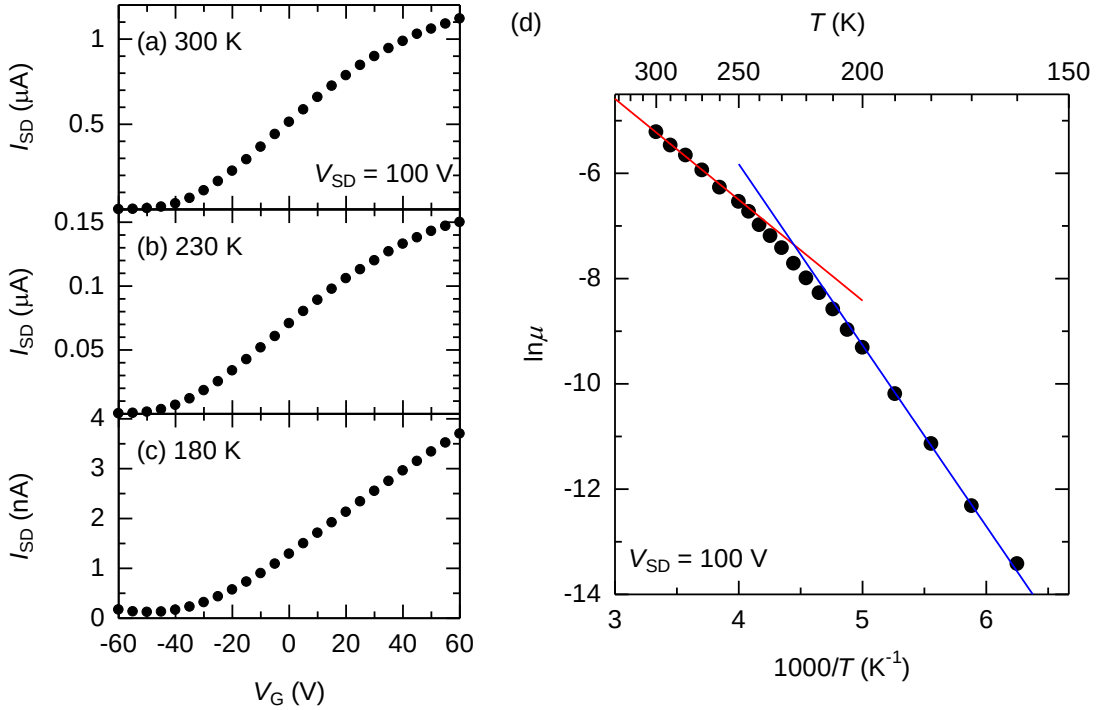

Figure 3.3.10 The transfer characteristics of FL–TCNQ FET at (a) 300 K, (b) 230 K and (c) 180 K. (d) Arrhenius plot of the mobility. Red and blue lines were obtained by least-square fitting at the range 300-250 K and 200-160 K, respectively.

Figure 3.3.11 shows the device properties of the TET–TCNQ single-crystal FET in variable temperatures. The device showed n-type behavior at 300 K. The device also exhibited normally on behavior, the threshold voltage (V_{th}) was −28.9 V. The mobility μ was estimated as 8.2 × 10^{-5} $cm^2/(V \cdot s)$, which is almost the same as that of AN–TCNQ. At 240 K, although the dominant carrier was electrons, slight p-type behavior was also observed. The contribution of the p-type behavior of the device was gradually increased with decreasing temperature. Even at the lowest temperature measured, the dominant carrier of the device was electrons. Below 180 K (around the transition temperature), the transfer characteristic could not be measured since the current was too small to detect.

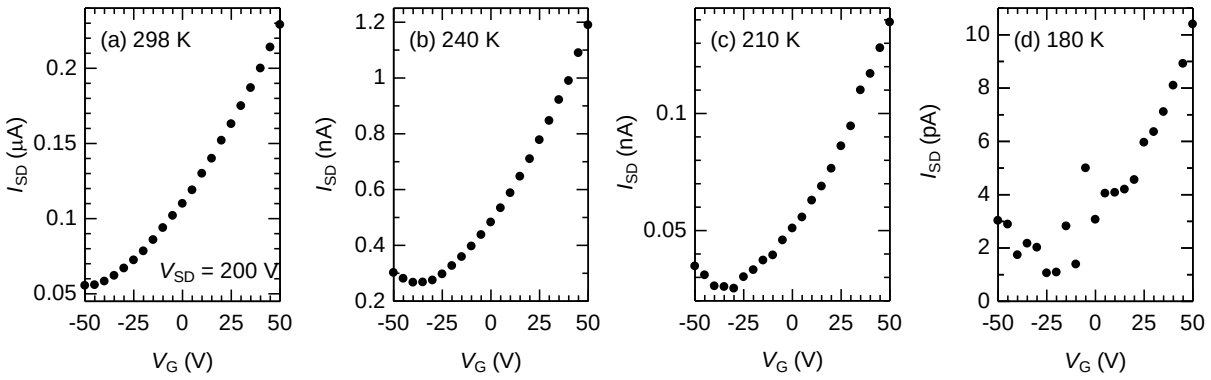

Figure 3.3.11. The transfer characteristics of FL–TCNQ FET at (a) 298 K, (b) 230 K, (c) 210 K and (d) 180 K.

The I_{SD} values of the TET–TCNQ FET at V_G = 50, 0, and −50 V are plotted against the reciprocal temperature in Figure 3.3.12. Each current value thermally decreased with decreasing the temperature. The E_a values of I_{SD} at V_G = 50, 0, and −50 V were estimated as 0.31, 0.34, and 0.31 eV, respectively. As mentioned in 3.3.1, disordered transport of holes can

occur in the device because the reorientational motion of TET molecule occur in the crystal as well as AN–TCNQ FET (Figure 3.3.12b). But, temperature independent hole transport, which was observed in AN–TCNQ FET, was not observed in the TET–TCNQ FET at the temperature range measured. In the TET–TCNQ crystal, there are relatively large amount of thermally activated carriers because the band gap is narrower than that of AN–TCNQ. In TET–TCNQ FET, large positive gate voltage must be applied in order to deplete thermally activated carriers, electron in this case, from the crystal surface. It is considered that not only hole current but also electron current was measured in the I_{SD} at $V_G = -50$ V, resulting in the thermally activated behavior.

The device showed ambipolar behavior by lowering temperature, suggesting similar mechanism to AN–TCNQ. In the AN–TCNQ FET, the origins of ambipolar behavior were disordered transport in the HT phase and ionic domains in the LT phase. At this time, I cannot identify which mechanisms is suitable in the TET–TCNQ FET. Lower temperature measurements of transfer characteristics and characterization of electronic structure at low temperature are needed to understand the mechanism.

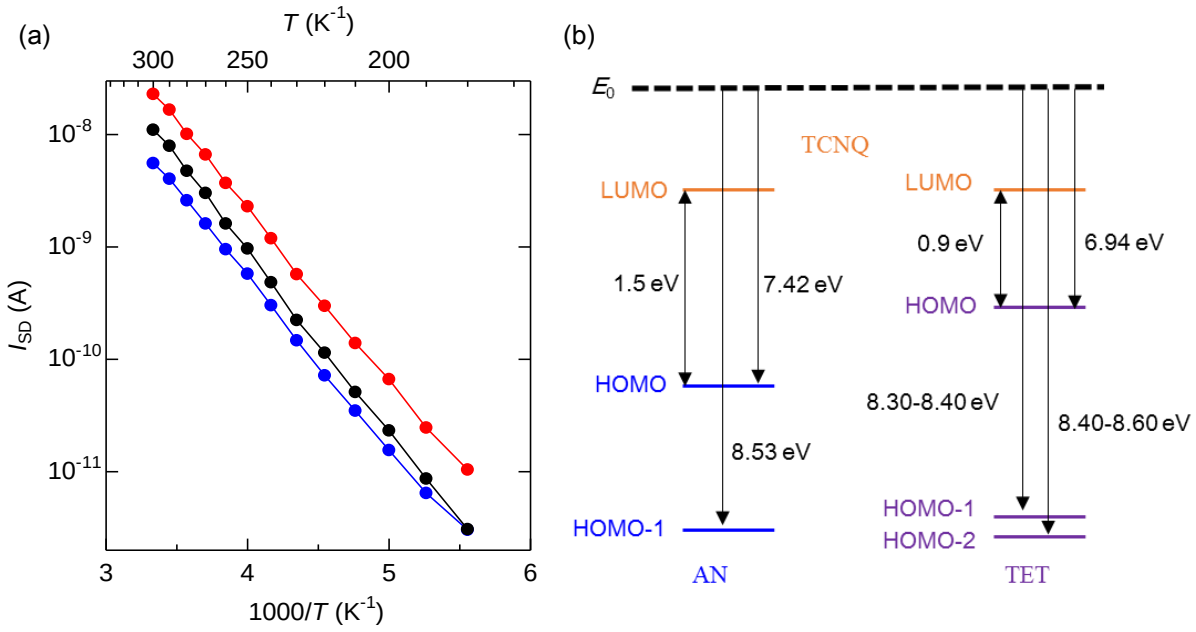

Figure 3.3.12. (a) Temperature dependence of I_{SD} with V_G = 0 (black), 50 (red), and −50 V (blue). (b) Energy diagram of AN–TCNQ and TET–TCNQ. The values of ionization potential were obtained by gas phase UPS measurements in ref. [12].

3.4. SUMMARY

It was revealed that the crystals of FL–TCNQ and TET–TCNQ show structural phase transitions from their XRD structure analyses at 300 and 100 K. Each crystal becomes twin in the LT phase since the crystal system is changed from monoclinic to triclinic.

The transfer characteristics of the FL–TCNQ FET can be measured below the transition temperature. The E_a of the mobility was found to become larger by the twinning. The most likely influence of twinning to the device property, defects formed between the TDs interfere the charge transport, was confirmed.

The transfer characteristics of the FET using TET–TCNQ could not be measured below the transition temperature. The device showed ambipolar behavior with decreasing temperature. In order to understand the mechanism, other detailed measurements are required.

3.5. REFERENCES

1. Roberson, L. B.; Kowalik, J.; Tolbert, L. M.; Kloc, C.; Zeis, R.; Chi, X.; Fleming, R.; Wilkins, C. *J. Am. Chem. Soc.* **2005**, *127* (9), 3069
2. Shtein, M.; Mapel, J.; Benziger, J. B.; Forrest, S. R. *Appl. Phys. Lett.* **2002**, *81* (2), 268.
3. Nespolo, M. *Cryst. Res. Technol.* **2015**, *50* (5), 362.
4. Lund, H. *Acta Chem. Scand.* **1957**, 11**,** 1323.
5. Pysh, E. S.; Yang, N. C. *J. Am. Chem. Soc.* **1963**, 85**,** 2124
6. Arrais, A.; Boccaleri, E.; Croce, G.; Milanesio, M.; Orlando, R.; Diana, E. *CrystEngComm* **2003**, *5* (68), 388.
7. Sheldrick, G. M. *Acta Crys-tallogr., Sect. A* **2008**, 64, 112.
8. Hoffmann, R. *J. Chem. Phys.* **1963**, 39, 1397.
9. Whangbo, M.-H.; Hoffmann, R.; Woodward, R. B. *Proc. R. Soc. A Math. Phys. Eng. Sci.* **1979**, 366, 23.
10. Ren, J.; Liang, W.; Whangbo, M.-H. *CAESAR*; Prime-Color Software, Inc.: Raleigh, NC, 1998.
11. Kistenmacher, T. J.; Emge, T. J.; Bloch, A. N.; Cowan, D. O. *Acta Crystallogr. Sect. B Struct. Crystallogr. Cryst. Chem.* **1982**, 38, 1193.
12. Coropceanu, V.; Malagoli, M.; da Silva Filho, D. a; Gruhn, N. E.; Bill, T. G.; Brédas, J. L. *Phys. Rev. Lett.* **2002**, *89* (27), 275503.

Chapter 4.

The Field-Effect Transistors Using Charge-Transfer Complexes: Relationship between the Performance and Their Molecular Packing

4.1. INTRODUCTION

Recently, a wide variety of organic-based field-effect transistors (FETs) have been fabricated and investigated.[1-5] Their performance of p-type OFETs has been improved in various studies, and many organic-based devices exceeding the performance of amorphous silicon have been reported.[5-13] Some of them show high performance even in thin film transistors, having attractive features for ubiquitous networks such as low-cost, flexibility, or large area.[3-11] In order to realize the efficient logic circuits based on organic FETs, we further need to develop the n-type FETs with high electron mobility, although the attempt has often encountered difficulty due to the instability of single component π-electron materials against the surface oxidation or reduction.

Charge-transfer (CT) complexes that are well-known two-component π-electron materials composed of electron donor (*D*) and acceptor (*A*) molecules are one of the candidate material groups for high performance n-type organic transistors.[14,15] Some n-type transistors exceeded

~1 cm^2 /(V·s) have been reported with using CT complexes such as DBTTF–TCNQ for channel crystals.[16, 17] CT complexes have various band and electronic structures as semiconducting material owing to their CT interactions. The degree of CT interaction may be varied by donor strength of *D* and acceptor strength of *A* and their molecular overlaps in the lattice. It is expected that these parameters also affect transport characteristics of transistors when CT complexes are used as a semiconductor. The n-type transistors are expected to be realized for semiconductors with the conduction band situated at relatively low energy (close to the Fermi level of the electrode metal). For the CT complexes with mixed-stack structures, this situation corresponds to the case where the electron accepting ability of *A* is relatively strong, since the conduction band is mainly composed of LUMO (lowest unoccupied molecular orbital) of the acceptor. Since the conduction band should be empty or contain only a small number of electrons, the degree of charge transfer in the CT complex should be small. For such purpose, the donor component should not be strong. Therefore, I utilized mixed-stack semiconducting CT complexes composed of PXX (*peri*-xanthenoxanthene) as a relatively weak donor component (Figure 1).[18] The strong acceptors adopted are, F_2TCNQ (2,5-difluoro-7,7,8,8,-tetracyanoquinodimethane), Cl_2TCNQ (2,5-dichloro-TCNQ), DDQ (2,3-dichloro-5,6-dicyano-*p*-benzoquinone), F_4TCNQ (2,3,5,6-tetrafluoro-TCNQ). The relationship between the device properties and their molecular packing has been investigated.

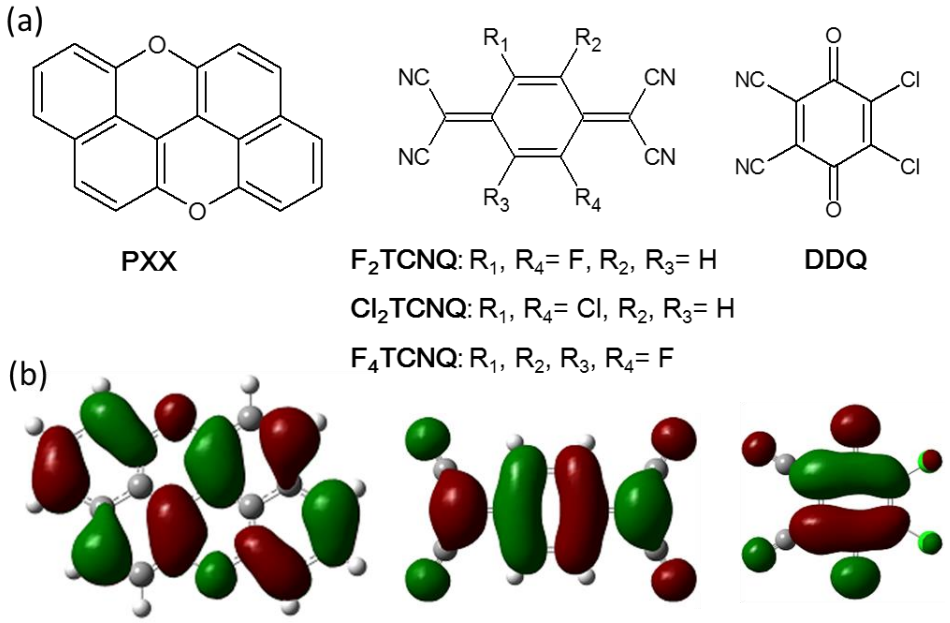

Figure 1 (a) Molecular structures and (b) HOMO of PXX, and LUMOs of TCNQ and DDQ

4.2. EXPERIMENTAL SECTION

4.2.1. Materials

The starting materials were obtained as follows: F_4TCNQ and DDQ were purchased from Tokyo Chemical Industry Co., Ltd. PXX, F_2TCNQ and Cl_2TCNQ were synthesized according to the literature provided.[18-20] These materials were purified by the combination of recrystallization and sublimation. The CT complexes of PXX–F_2TCNQ, PXX–Cl_2TCNQ, PXX–F_4TCNQ and PXX–DDQ were prepared by co-sublimation of the respective molecules in a sealed vacuum glass tube (see chapter 2). The temperature of each zone was set as 180 °C (TCNQ derivate), 140 °C (DDQ), 220 °C (PXX) and 120 °C (crystal growth). Single crystal of each complex was obtained with shiny surfaces with a typical size of 1.0-0.8 × 0.5-0.3 × 0.3-0.1 mm^3. The crystal long axes are parallel to the molecular stacking axis.

4.2.2. Device Fabrication and Measurements

Gold was used as the source and drain electrodes, which were deposited with the thickness of about 30 nm by the thermal evaporation on the top of the as-grown crystal surfaces through shadow masks. The electrodes were arranged to measure current-voltage characteristics along the molecular stacking axis. Typical channel length is about 50 μm. Parylene C was used as the gate dielectric layer with typical thickness of about 500 nm (C_i = 5.1 nF cm^{-2}). Then the gate electrodes of Au were fabricated on top of the insulators. The field-effect properties were measured under the ambient environment using a dual channel system source meter (Keithley 2636A).

4.2.3. Crystallographic Study

The X-ray diffraction intensity data for single crystals of the PXX complexes were obtained using an automated Rigaku R-Axis rapid X-ray diffractometer with graphite monochromated MoKα radiation. The crystal structures were solved by employing the direct methods of SIR2004[21] and SHELX-97[22] in the CrystalStructure4.0[23] crystallographic software package. The crystal data for the complexes are summarized in Table 1. Refinement of the structures was carried out using a full-matrix least-squares refinement on F^2. All of the non-hydrogen atoms were refined anisotropically. The hydrogen atoms were placed at the theoretically calculated ideal positions, related to their respective parent atoms, with a riding model for the structure refinement.

4.2.4. Calculation

The overlap integrals between the highest occupied molecular orbital (HOMO) of *D* and the lowest unoccupied molecular orbital (LUMO) of *A* for each crystal were calculated under the extended Hückel approximation[24, 25] using the CAESAR program package.[26] The optimization and energy calculations of isolated single molecules were performed using Gaussian 09W at the B3LYP/6-31G(d,p) level.

4.3. RESULTS AND DISCUSSION

4.3.1. Crystal Structure and Overlap Integral

The composition ratio of *D* and *A* in the four kinds of PXX complexes in this work was found to be 1:1. The crystallographic data are summarized in Table 4.3.1. The crystals of PXX–F_2TCNQ, PXX–Cl_2TCNQ and PXX–DDQ belong to the triclinic system, space group *P*-1 while the crystal structure of PXX–F_4TCNQ belongs to the monoclinic system, space group $P2_1/n$. These complexes consist of mixed-stacks of *D* and *A* molecules, but their packing patterns are different with each other.

Table 4.3.1 Crystallographic Data for Each PXX Complex

	PXX–F_2TCNQ	PXX–Cl_2TCNQ	PXX–DDQ	PXX–F_4TCNQ
Formula	$C_{32}H_{12}F_2N_4O_2$	$C_{32}H_{12}Cl_2N_4O_2$	$C_{28}H_{10}Cl_2N_2O_4$	$C_{32}H_{10}F_4N_4O_2$
Temperature (K)	293	293	293	293
Crystal System	triclinic	triclinic	triclinic	monoclinic
Space Group	$P\bar{1}$	$P\bar{1}$	$P\bar{1}$	$P2_1/n$
a (Å)	6.5717(6)	7.3979(7)	7.5967(4)	8.5735(7)
b (Å)	8.6755(8)	8.7269(8)	9.2631(6)	12.9533(8)
c (Å)	11.3556(11)	9.7613(9)	16.4080(9)	20.875(2)
α (°)	106.252(3)	74.172(3)	92.8691(18)	90
β (°)	108.956(3)	83.221(2)	90.3446(15)	91.800(3)
γ (°)	94.979(3)	87.320(2)	114.2070(15)	90
V (Å^3)	576.47(10)	601.99(9)	1051.32(10)	2317.1(3)
Z	1	1	2	4
R_{int}	0.0237	0.0341	0.0160	0.0426
R_1 [$I > 2\sigma(I)$]	0.0471	0.0354	0.0360	0.0606
R_w (all refelction)	0.0758	0.0456	0.1109	0.0872

PXX–F_2TCNQ and PXX–Cl_2TCNQ. These two complexes are classified into the typical

mixed-stacked arrangement. In the crystal of PXX–F_2TCNQ and PXX–Cl_2TCNQ, each molecule is located at the inversion center of the unit cell, so the π-stack columns are composed of uniform *DA* stacking, *i.e. DADA-type* arrangement. However, crystal structures of these complexes are not completely isomorphic. In PXX–F_2TCNQ crystal, the molecular plane of each molecule is almost perpendicular to the stacking axis *a* (89.23 ° for PXX and 88.32 ° for F_2TCNQ). On the other hand, the molecular planes in PXX–Cl_2TCNQ are tilted largely to the stacking axis *a* (66.27 ° for PXX and 68.16 ° for Cl_2TCNQ). The inter-planer distance between *D* and *A* is estimated as 3.28 Å for PXX–F_2TCNQ and 3.37 Å for PXX Cl_2TCNQ. The overlapping mode (OM) of *D*'s HOMO and *A*'s LUMO in PXX–F_2TCNQ crystal is largely different from that in PXX–Cl_2TCNQ as shown in Figures 4.3.1b and d. Because of these differences in crystal structure, the overlap integral values in those complexes are quite different (15.8×10^{-3} for PXX–F_2TCNQ and 2.7×10^{-3} for PXX–Cl_2TCNQ).

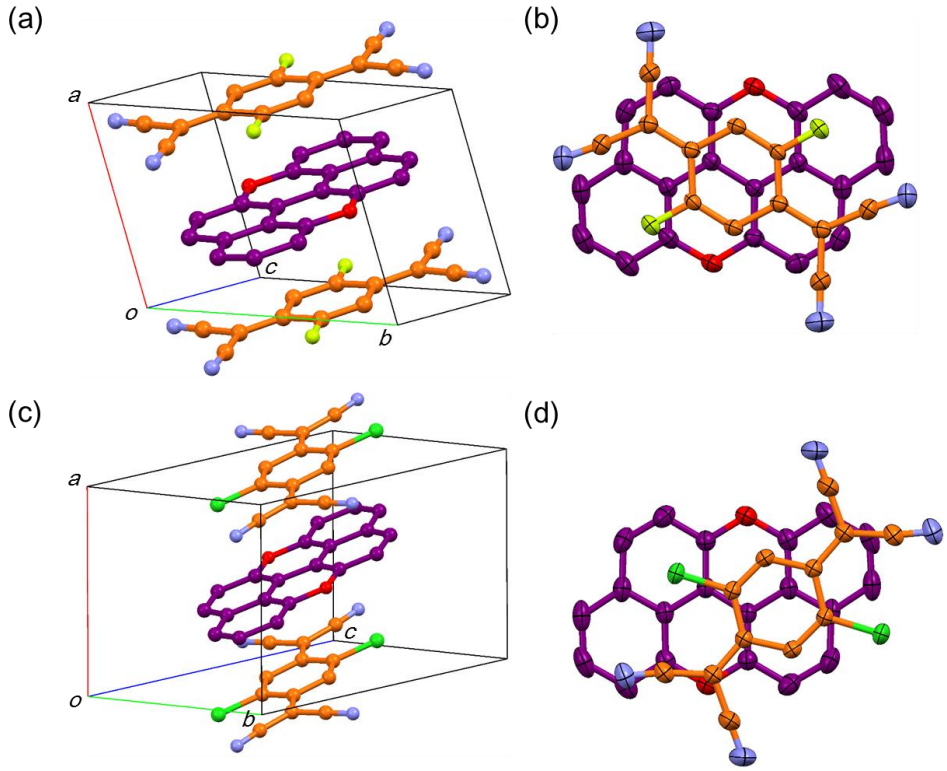

Figure 4.3.1. Crystal structures and overlapping modes of (a), (b) PXX–F_2TCNQ and (c), (d) PXX–Cl_2TCNQ

PXX–DDQ. The crystal also shows mixed-stacked arrangement. In contrast to the above two complexes, the π-stack column is consisted of non-uniform stacks of the components with two kinds of OMs since each molecule is located at a general position of the unit cell (Figure 4.3.2). Such structure indicates that PXX and DDQ molecules form dimer. In addition, the inter-planer distances of intra-dimer and inter-dimer are estimated as 3.21 and 3.25 Å, respectively. The overlap integral of each OM is calculated as 18.2×10^{-3} (intra-dimer, OM1) and 12.0×10^{-3} (inter-dimer, OM2), respectively. In this paper, this arrangement is called as *(DA)(DA)-type* arrangement.

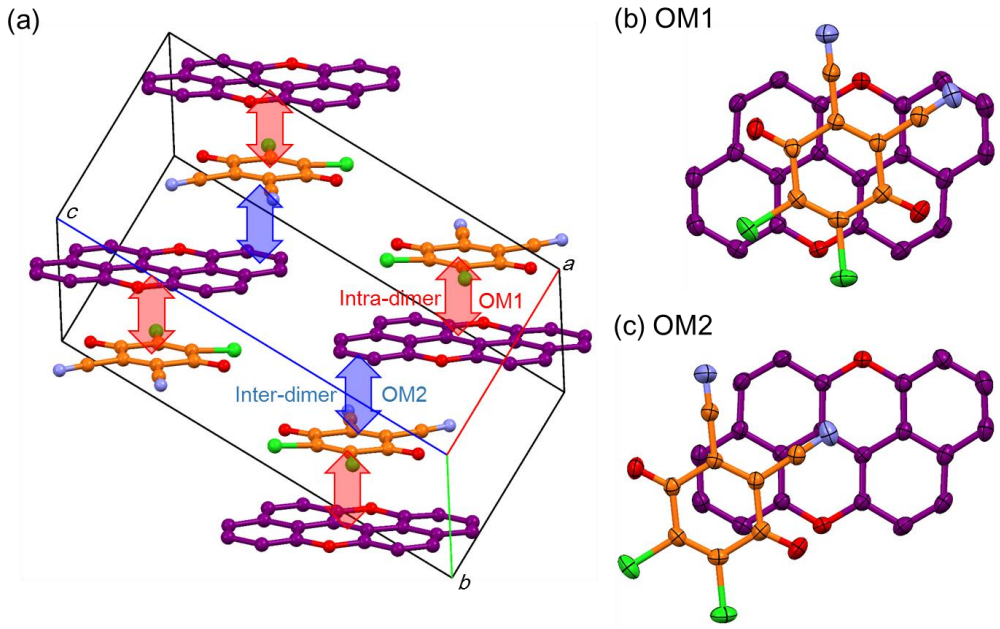

Figure 4.3.2. (a) Crystal structure of PXX–DDQ and (b), (c) OMs of PXX–DDQ

PXX–F$_4$TCNQ. Also in this crystal, *D* and *A* molecules are located at the general positions of the unit cell and form a dimer. The crystal have a 2D π-π network, which is different from the above three complexes (1D π-stack). The OM of intra-dimer is almost the same as that of PXX–F$_2$TCNQ. On the other hand, there are six OMs between the dimers, which indicates that a 2D π-π network is formed in the crystal (Figure 4.3.3). The overlap integral of intra-dimer (OM1) is estimated as 20.0×10^{-3}, which is larger than that in PXX–DDQ. In contrast to PXX–DDQ, the overlap integrals of inter-dimer, especially those of OM2 (*DD*), 5 (*DA*), 6 (*AA*), and 7 (*AA*) are small. Thus, it is considered that these four OMs do not contribute mainly to the π-π network. The largest inter-dimer overlap integral is obtained for OM3 (*DD*), but, if this OM works as the main π-π network, the stacking sequence becomes *(DA)(AD)*, which includes poor overlaps between *A* molecules (OM6 and 7). I consider the π-stack sequence is *(DA)(DA)* in order to exclude the poor overlaps. The 2D π-π network (Figure 4.3.4) can be summarized as

below; the quasi-1D non-uniform π-stack columns are composed of OM1 and OM4 with *(DA)(DA)* sequence and the columns are connected by overlaps of *D* molecules (OM3) as shown in Figure 4.3.4. The molecular stacking pattern of PXX–F_4TCNQ is called as *(DA)(DA)-type* in this thesis.

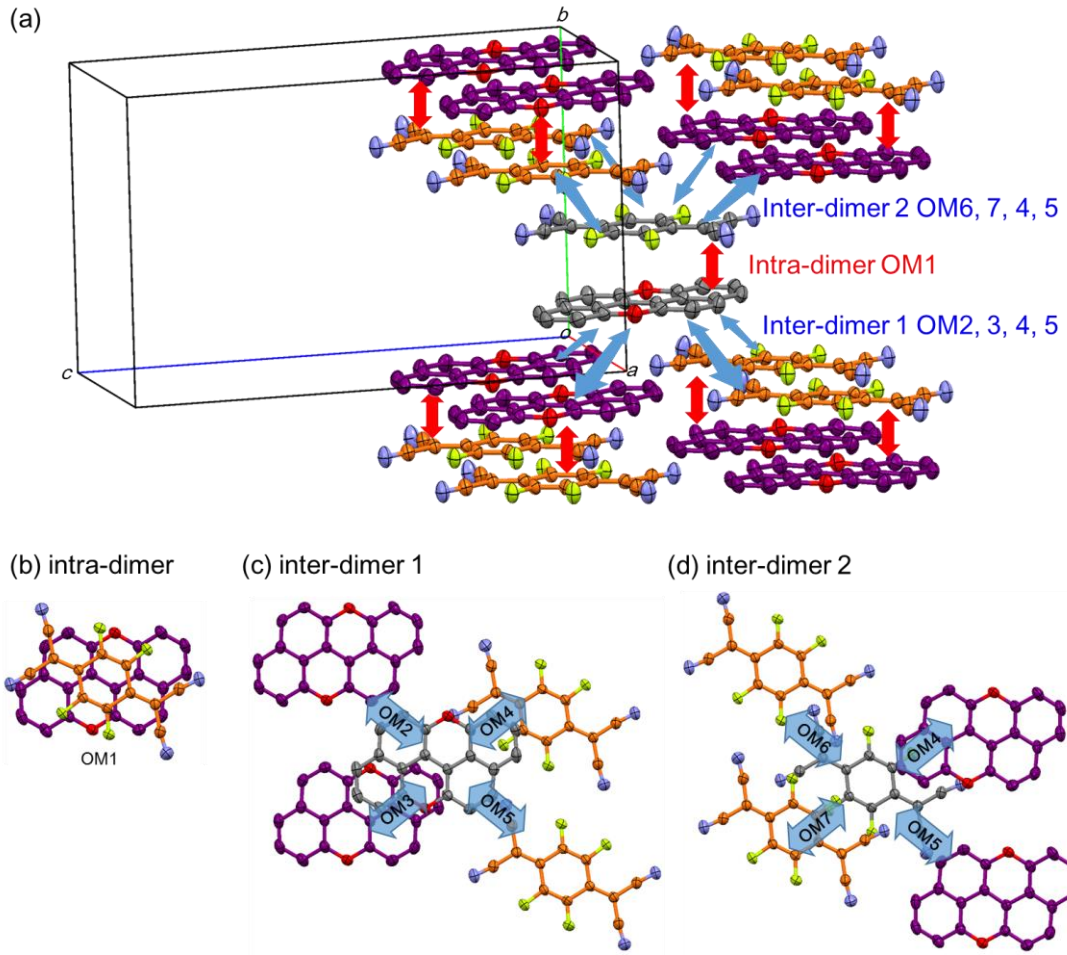

Figure 4.3.3. (a) Crystal structure of PXX–F_4TCNQ. Inter molecular contacts are shown by red (intra-dimer) and blue (inter-dimer) arrows. (b) OM of intra-dimer. (c) and (d) OMs of inter-dimer.

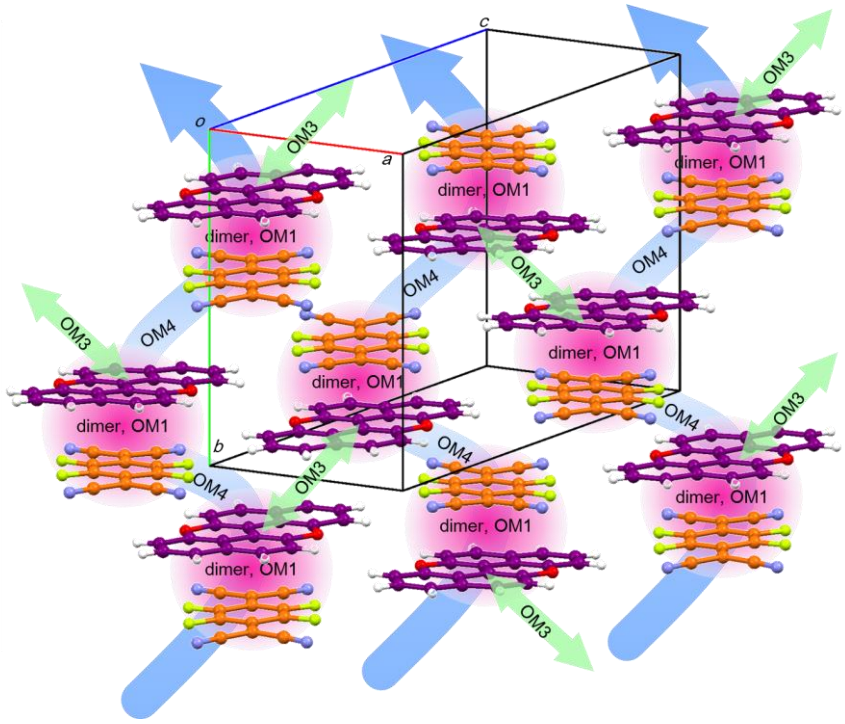

Figure 4.3.4. The 2D π-π network in PXX–F_4TCNQ.

Table 4.3.2. Overlap Integral of Each Overlapping Mode (OM)

complex		Overlap integral (10^{-3})	
PXX–F_2TCNQ		OM1 (*DA*)	15.8
PXX–Cl_2TCNQ		OM1 (*DA*)	2.7
PXX–DDQ	Intra-dimer	OM1 (*DA*)	12.0
	Inter-dimer	OM2 (*DA*)	18.2
PXX–F_4TCNQ	Intra-dimer	OM1 (*DA*)	20.0
	Inter-dimer	OM2 (*DD*)	0.1
	Inter-dimer	OM3 (*DD*)	5.7
	Inter-dimer	OM4 (*DA*)	1.7
	Inter-dimer	OM5 (*DA*)	0.5
	Inter-dimer	OM6 (*AA*)	0.3
	Inter-dimer	OM7 (*AA*)	0.1

The π-π network of these four complexes can be summarized as follows. PXX–F_2TCNQ

has uniform 1D π-stack with relatively large overlap integral. PXX–Cl_2TCNQ also has uniform 1D π-stack, however, the overlap integral is quite small. In PXX–DDQ, dimerization of *D* and *A* occur and non-uniform 1D π-stack is formed with relatively large inter-dimer overlap integral. PXX–F_4TCNQ has a 2D π-π network which is composed of non-uniform 1D π-stack and inter-column interaction by overlap of PXX molecules. The inter-dimer overlap integrals are relatively small.

Up to here, the difference of crystal structure of the four PXX complexes has been discussed, but these crystals also have a similar structural feature. Along the molecular short axis, paired hydrogen bonds (C–H•••O) were formed between PXX molecules, which also occurred in pristine PXX crystal (Figure 4.3.5).[18] In each crystal, ribbon structure is formed by paired hydrogen bonds (C–H•••O) between PXX molecules (Figure 4.3.6). Generally, this type of supra-molecular interaction is not so stable in CT complexes, because of the Coulomb repulsive interaction between *D* and *D* or *A* and *A* molecules. Thus, *D* (*A*) molecules tend not to form sheet or ribbon structure in order to reduce Coulomb repulsion between *D* (*A*) molecules and to increase Madelung energy. However, it is considered that stabilization energy by the supra-molecular interactions is relatively strong in the PXX CT crystals compared with the cost for the destabilization energy from the D•••D contacts. Other three PXX complexes were reported by Asari, which also have similar supra-molecular structure.[18] Thus, the supra-molecular structure is preferred in CT complexes using PXX as a donor component.

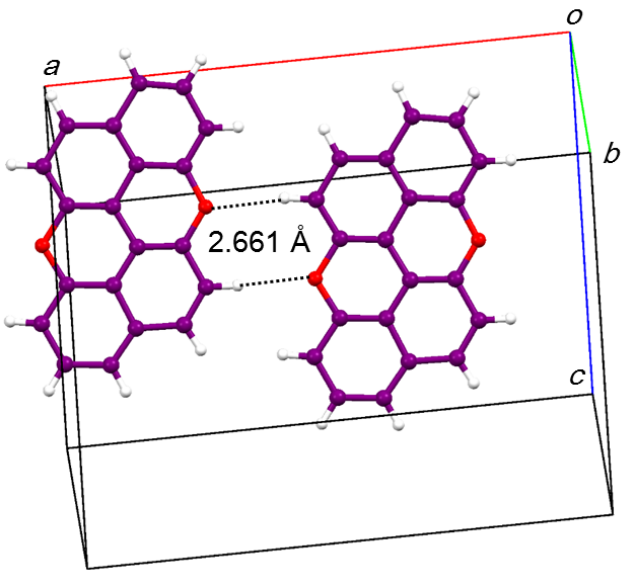

Figure 4.3.5. Hydrogen bonds in the pristine PXX crystal

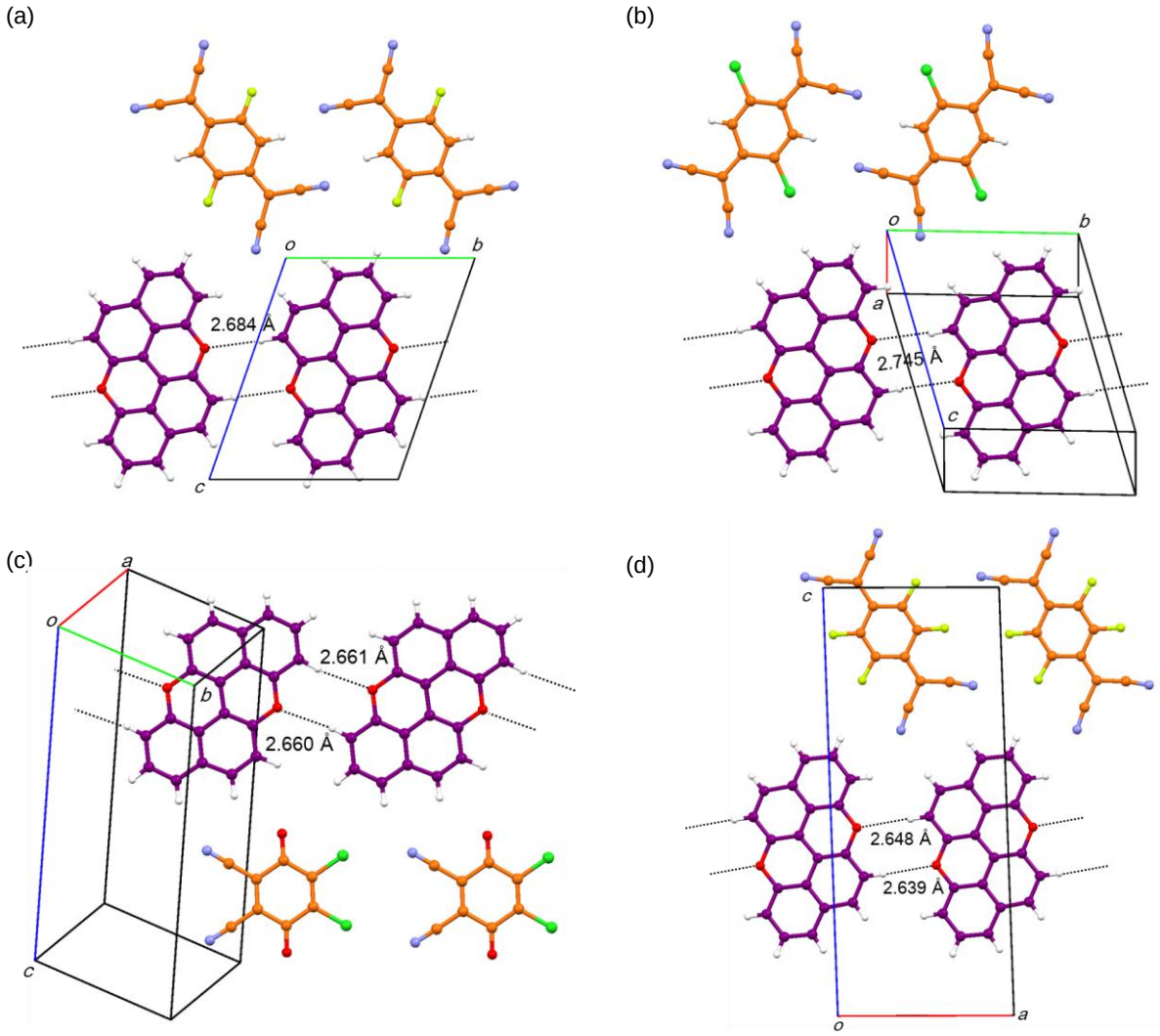

Figure 4.3.5. The ribbon structure in the PXX complexes. (a) PXX–F_2TCNQ, (b) PXX–Cl_2TCNQ, (c) PXX–DDQ, and (d) PXX–F_4TCNQ. The C–H•••O distances were shown for each complexes.

4.3.2. The properties of Field-Effect transistors

Figure 5 shows the transfer characteristics of the single crystal FETs of these complexes with the drain voltage (V_D) fixed at +50 V. All the results clearly show the n-type field-effect characteristics. The mobility of these devices were estimated as 1.6 x 10^{-2} cm^2 /(V·s) (PXX–F_2TCNQ), 1.3 x 10^{-4} cm^2 /(V·s) (PXX–Cl_2TCNQ), 3.5 x 10^{-3} cm^2 /(V·s) (PXX–DDQ), and 2.7 x 10^{-4} cm^2 /(V·s) (PXX–F_4TCNQ), from the transfer characteristics with using the FET formula

in the linear region; $\mu_{lin} = (dI_D/dV_G)[L/(WC_iV_D)]$.[27] This result is consistent with the difference of the overlap integrals and stacking patterns. The highest mobility was observed in the device with PXX–F_2TCNQ, which has *DADA-type* structure with uniform relatively large overlap integral. PXX–Cl_2TCNQ also has *DADA-type*, however, the device shows lowest mobility since the overlap integral is very small. Here, we note that FET on PXX–F_2TCNQ showed normally-on behavior. This behavior reflects the relatively high conductivity of PXX–F_2TCNQ at room temperature, indicating the presence of thermally activated carriers in the crystal. These carriers were depleted from the crystal surface by positive gate voltage. The device with PXX–DDQ, *(DA)(DA)-type*, complex showed relatively high mobility. In contrast, the device with PXX–F_4TCNQ, (*DA)(DA)-type*, showed low mobility. Though, both of the complexes are dimerized, the inter-dimer interaction of PXX–DDQ is larger than that of PXX–F_4TCNQ. The difference is reflected in the value of the mobility of the complexes. The off-currents of these devices showed a similar trend with the mobilities.

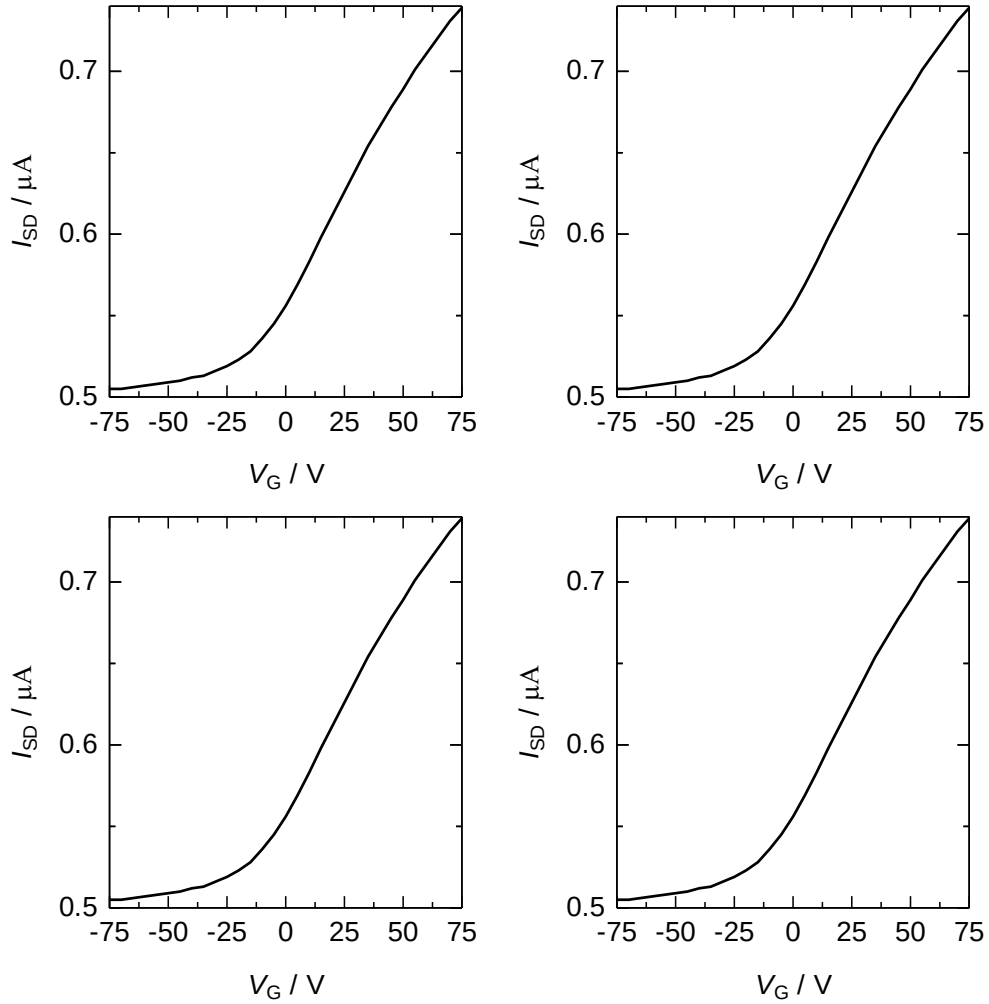

Figure 4.3.6. Transfer characteristics of FETs with using (a) PXX–F_2TCNQ, (b) PXX–Cl_2TCNQ, (c) PXX–DDQ and (d) PXX–F_4TCNQ as semiconductor crystal. V_{SD} = 50 V in each device.

Figure 4.3.7 depicted the output characteristics at various V_G for these devices. The all devices did not shows clear current saturation in the high V_D range, because of using bulk single crystals as semiconductor layers.

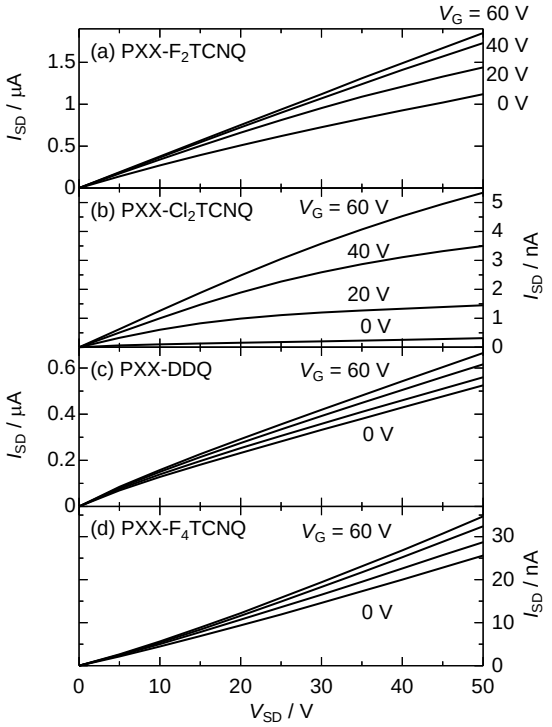

Figure 4.3.7. Output characteristics at various V_G (= 0, 20, 40 and 60 V) of the FETs using (a) PXX–F_2TCNQ, (b) PXX–Cl_2TCNQ, (c) PXX–DDQ and (d) PXX–F_4TCNQ as semiconductor crystal.

All the results presented above clearly show that there is a certain relationship between the device performances and molecular packing in the CT complex semiconductors. I suggest that using a CT complex with uniform stacking and large overlap between *D* and *A* molecules would be useful to improve the device performance including n-type organic FETs.

4.4. SUMMARY

Four kinds of CT complex crystals using PXX as donor were obtained by the co-sublimation method. The four CT complexes have different molecular arrangements and overlap integrals. It was shown that the four kinds of organic FETs with using single crystals of PXX CT complexes as the semiconductor layer show n-type characteristics. The relationship between molecular arrangements and device performances was found. The highest mobility was obtained for the device of PXX–F_2TCNQ. The complex had the largest transfer integral in the four kinds of CT complexes used in this work. In addition, semiconductor crystals with poor overlap integral or with strong dimerization showed poor performance. This study suggests that to use a CT complex with rich intra-column interaction as semiconductor materials is important to fabricate high performance organic FETs.

4.5. REFERENCES

1 Kaltenbrunner, M.; Sekitani, T.; Reeder, J.; Yokota, T.; Kuribara, K.; Tokuhara, T.; Drack, M.; Schwödiauer, R.; Graz, I.; Bauer-Gogonea, S.; Bauer, S.; Someya, T. *Nature* **2013**, 499, 458.

2 Webb, R. C.; Bonifas, A. P.; Behnaz, A.; Zhang, Y.; Yu, K. J.; Cheng, H.; Shi, M.; Bian, Z.; Liu, Z.; Kim, Y.-S.; Yeo, W.-H.; Park, J. S.; Song, J.; Li, Y.; Huang, Y.; Gorbach, A. M.; Rogers, J. *Nat. Mater.* **2013**, 12, 938.

3 Murphy, A. R.; Fréchet, J. M. J. *Chem. Rev.* **2007**, 107, 1066–1096.

4 Klauk, H. *Chem. Soc. Rev.* **2010**, 39, 2643.

5 Yi, H. T.; Payne, M. M.; Anthony, J. E.; Podzorov, V. *Nat. Commun*. **2012**, 3, 1259.

6 Okamoto, T.; Mitsui, C.; Yamagishi, M.; Nakahara, K.; Soeda, J.; Hirose, Y.; Miwa, K.; Sato, H.; Yamano, A.; Matsushita, T.; Uemura, T.; Takeya, J. *Adv. Mater.* **2013**, 25, 6392.

7 Nakayama, K.; Hirose, Y.; Soeda, J.; Yoshizumi, M.; Uemura, T.; Uno, M.; Li, W.; Kang, M. J.; Yamagishi, M.; Okada, Y.; Miyazaki, E.; Nakazawa, Y.; Nakao, A.; Takimiya, K.; Takeya, J. *Adv. Mater.* **2011**, 23, 1626.

8 Minemawari, H.; Yamada, T.; Matsui, H.; Tsutsumi, J.; Haas, S.; Chiba, R.; Kumai, R.; Hasegawa, T. *Nature* **2011**, 475, 364.

9 Giri, G.; Verploegen, E.; Mannsfeld, S. C. B.; Atahan-Evrenk, S.; Kim, D. H.; Lee, S. Y.; Becerril, H. A.; Aspuru-Guzik, A.; Toney, M. F.; Bao, Z. *Nature* **2011**, 480, 504.

10 Yuan, Y.; Giri, G.; Ayzner, A. L.; Zoombelt, A. P.; Mannsfeld, S. C. B.; Chen, J.; Nordlund, D.; Toney, M. F.; Huang, J.; Bao, Z. *Nat. Commun.* **2014**, 5, 3005.

11 Diao, Y.; Tee, B. C.-K.; Giri, G.; Xu, J.; Kim, D. H.; Becerril, H. a; Stoltenberg, R. M.; Lee, T. H.; Xue, G.; Mannsfeld, S. C. B.; Bao, Z. *Nat. Mater.* **2013**, 12, 665.

12 Takahashi, Y.; Hasegawa, T.; Horiuchi, S.; Kumai, R.; Tokura, Y.; Saito, G. *Chem. Mater.* **2007**, 19, 6382.

13 Takeya, J.; Yamagishi, M.; Tominari, Y.; Hirahara, R.; Nakazawa, Y.; Nishikawa, T.; Kawase, T.; Shimoda, T.; Ogawa, S. *Appl. Phys. Lett.* **2007**, 90, 102120.

14 Farges, J. -P. ed., *Organic Conductors* (Marcel Dekker, New York, 1994)

15 Conwell, E. ed., *Semiconductors and Semimetals, Vol27* (Academic Press, New York, 1988)

16 Kawasugi, Y.; Yamamoto, H. M.; Hosoda, M.; Tajima, N.; Fukunaga, T.; Tsukagoshi, K.; Kato, R. *Appl. Phys. Lett.* **2008**, 92, 243508.

17 Takahashi, Y.; Hasegawa, T.; Abe, Y.; Tokura, Y.; Nishimura, K.; Saito, G.; *Appl. Phys. Lett.* **2005**, 86, 063504.

18 Asari, T.; Kobayashi, N.; Naito, T.; Inabe, T. *Bull. Chem. Soc. Jpn.* **2001**, 74, 53.

19 Pummerer, R.; Prell, E.; Rieche, A.; *Ber. Dtsch. Chem. Ges*. **1929**, 59, 2159.

20 Mochida, T.; Hasegawa, T.; Kagoshima, S.; Sugiura, S.; Iwasa, Y. *Synth. Met.* **1997**, 86, 1797.

21 SIR 2004: Burla, M. C.; Caliandro, R.; Camalli, M.; Carrozzini, B.; Cascarano, G. L.; De Caro, L. Giacovazzo, C.; Polidori, G.; Spagna, R.; *J. Appl. Crystallogr.* **2005**, 38, 381

22 Sheldrick, G. M. *Acta Crys-tallogr., Sect. A* **2008**, 64, 112.

23 CrystalStructure4.0: Crystal Structure Analysis Package; Rigaku Corporation: Tokyo, 2000−2010

24 Hoffmann, R.; *J. Chem. Phys*. **1963**, 39, 1397−1412.

25 Whangbo, M.-H.; Hoffmann, R.; Woodward, R. B. *Proc. R. Soc. A Math. Phys. Eng. Sci.* **1979**, 366, 23–46.

26 Ren, J.; Liang, W.; Whangbo, M.-H. *CAESAR*; Prime-Color Software, Inc.: Raleigh, NC, 1998.

27 S. M. Sze, *Physics of Semiconductor Devices 2nd ed.* (Wiley, New York, 1981)

Chapter 5.

Conclusion

In this study, single-crystal FETs using CT complexes as semiconductor layers were fabricated and the transport properties were investigated.

In Chapter 2, an FET was fabricated using an AN–TCNQ single crystal, which underwent two structural phase transitions related to in-plane reorientational motion. The transfer characteristics drastically changed when decreasing the temperature from room temperature to 90 K: n-type → ambipolar-type → p-type → ambipolar-type. The electron and hole transport paths in the AN–TCNQ FET were different in the HT phase because of the molecular motion. The electron transport was hopping-type, while holes transported through disordered orbitals by reorientational motion of AN molecules, resulting in gradual change of transfer characteristic from n-type to p-type with decreasing temperature. Ambipolar behavior in the LT phase is considered to be caused by the presence of ionic pairs in the crystal, which are detected in the optical measurements. The ionic pair became the trap site in the high-temperature region, while it was involved in carrier transport in the low-temperature region. This study showed that transport characteristics can be used to study the change of molecular dynamics and electronic structure. A detailed study of the FET characteristics is useful for both device design and investigation of the transport properties of CT complexes.

In Chapter 3, the transfer characteristics of the FL–TCNQ FET can be measured below the transition temperature. The E_a of the mobility was found to become larger by the twinning. The

most likely influence of twinning to the device property, defects formed between the TDs interfere the charge transport, was confirmed. The transfer characteristics of the FET using TET–TCNQ could not be measured below the transition temperature. The device showed ambipolar behavior with decreasing temperature. In order to understand the mechanism, other detailed measurements are required.

In Chapter 4, it was shown that the four kinds of organic FETs with using single crystals of PXX CT complexes as the semiconductor layer exhibit n-type characteristics. The highest mobility was obtained for the device of PXX–F_2TCNQ. The complex had the largest transfer integral in the four kinds of CT complexes used in this work. In addition, semiconductor crystals with poor overlap integral or with strong dimerization showed poor performance. This study suggests that to use a CT complex with rich intra-column interaction as semiconductor materials is important to fabricate high performance organic FETs.

The measurements of OFETs properties are found to be useful evaluation methods of the transport properties of organic semiconductors because they have advantages such as the current enhancement, the sensitive response to the electronic structure change, and the individual detection of the hole and electron current. In this thesis, I explored the transport properties of the mixed-stack CT complexes, which had rarely been used for organic electronics in the previous srudies. Although it was well known that some mixed-stack CT complexes show molecular dynamics and/or phase transition, the correlation between these aspects and the transport properties have not been investigated because of their high resistivity. The measurements using FET structure enabled us to evaluate the transport properties of mixed-stack CT complexes, resulting in exposure of anomalous characteristics related to the molecular dynamics and the phase transitions.

In the previous studies on organic electronics, the semiconductor materials are limited to

only the molecular crystals which consist of a single component with poor varieties of molecular structure. This thesis indicated that the mixed-stack CT complexes, which have a large variety of the combination of two components, can be candidates of the semiconductors for organic electronics and are useful for the design of organic devices with unique properties. The methodology presented in this thesis will lead to understand the transport mechanism of organic semiconductors, resulting in fabricating various and unique devices with high performance.

Appendix

The SHELXL-2014 res files for the crystal structure with disorder

6. **AN–TCNQ at 300 K**
7. **AN–TCNQ at 150 K**
8. **FL–TCNQ at 300 K**
9. **FL–TCNQ at 100 K**
10. **TET–TCNQ at 300 K**

1. AN–TCNQ at 300 K

```
TITL ANT_TCNQ_300K in C2/m
CELL 0.71073    11.52760    12.97490     7.01260    90.0000 105.5838    90.0000
ZERR       2.00      0.00030      0.00040      0.00020      0.0000      0.0014      0.0000
LATT    7
SYMM -X, Y, -Z
SFAC C H N
UNIT 52 28 8
L.S. 5
FMAP 2
PLAN 40
BOND $H
CONF
LIST 4
TEMP 27
ACTA
EQIV $1 -x, -y, -z
DFIX 0.93 0.01 C5A H5A
SADI 0.01 H5A C6A H5A C11A_$1
RIGU C5A C6A C7A C8A C9A C10A C11A
RIGU C5B C6B C7B C8B
BIND C5A C11A_$1
SIZE 0.3 0.2 0.2
WGHT       0.081700       0.089400
FVAR           0.32798      0.71216
N1       3       0.376063       0.166278       0.655490       11.00000       0.09422       0.06949 =
             0.13102       0.00028       0.02345      -0.01682
C1       1       0.126905       0.000000       0.551490       10.50000       0.07457       0.04361 =
             0.04655       0.00000       0.02109       0.00000
C2       1       0.060173       0.095031       0.524029       11.00000       0.07826       0.03877 =
             0.06221      -0.00041       0.02207      -0.00291
AFIX    43
H2       2       0.101388       0.157417       0.539955       11.00000      -1.20000
AFIX     0
C3       1       0.250702       0.000000       0.602324       10.50000       0.07382       0.05107 =
```

0.05886 0.00000 0.02010 0.00000

C4 1 0.319625 0.093165 0.631430 11.00000 0.07529 0.06044 =

0.07972 0.00157 0.01978 -0.00194

part -1

C5A 1 -0.023760 0.102054 -0.013478 20.50000 0.09878 0.06221 =

0.07055 0.00648 0.03505 0.01282

H5A 2 -0.034968 0.173174 -0.020213 20.50000 -1.20000

SAME C11A C10A C9A C8A C7A C6A

C6A 1 0.096472 0.069737 0.039194 20.50000 0.10084 0.06862 =

0.06238 0.00413 0.04072 0.01045

C7A 1 0.196665 0.135240 0.087162 20.50000 0.11196 0.10242 =

0.09085 -0.00651 0.04867 0.00204

AFIX 43

H7A 2 0.184290 0.206054 0.087765 20.50000 -1.20000

AFIX 0

C8A 1 0.309793 0.099332 0.132233 20.50000 0.10272 0.13390 =

0.09933 -0.00564 0.03599 0.00009

AFIX 43

H8A 2 0.373452 0.145845 0.155742 20.50000 -1.20000

AFIX 0

C9A 1 0.335538 -0.010949 0.145327 20.50000 0.08477 0.13354 =

0.08892 -0.01197 0.02122 0.01238

AFIX 43

H9A 2 0.414383 -0.035094 0.177744 20.50000 -1.20000

AFIX 0

C10A 1 0.241808 -0.076730 0.109105 20.50000 0.07554 0.11611 =

0.06829 0.00025 0.01496 0.03030

AFIX 43

H10A 2 0.255872 -0.147389 0.114979 20.50000 -1.20000

AFIX 0

C11A 1 0.120700 -0.038976 0.061635 20.50000 0.08031 0.07807 =

0.03741 -0.00227 0.01530 0.01387

part 2

SAME C5A C6A C7A C8A

C5B 1 0.000000 0.114451 0.000000 -20.50000 0.07616 0.06339 =

0.04577 0.00000 0.01442 0.00000

```
AFIX   43
H5B    2      0.000000      0.186128     -0.000002     -20.50000     -1.20000
AFIX    0
C6B    1      0.105229      0.054704      0.034220     -21.00000      0.07176      0.08270 =
            0.03166      0.00610      0.00655      0.00376
C7B    1      0.217199      0.106632      0.083235     -21.00000      0.07746      0.11673 =
            0.07295     -0.00886      0.01621      0.00730
AFIX   43
H7B    2      0.218956      0.178264      0.080208     -21.00000     -1.20000
AFIX    0
C8B    1      0.321698      0.053268      0.134439     -21.00000      0.06871      0.11553 =
            0.07283     -0.00461      0.01341      0.00205
AFIX   43
H8B    2      0.394493      0.088666      0.170109     -21.00000     -1.20000
AFIX    0
HKLF 4

REM   ANT_TCNQ_300K in C2/m
REM R1 =   0.0452 for       1195 Fo > 4sig(Fo)    and   0.0564 for all       1539 data
REM       139 parameters refined using         75 restraints

END
```

2. AN-TCNQ at 300 K

```
TITL AN_TCNQ_155K in P2(1)/c
CELL 0.71073    11.57300      12.84790    6.90920    90.0000 107.0527    90.0000
ZERR        2.00      0.00150      0.00160      0.00090      0.0000      0.0020      0.0000
LATT    1
SYMM 0.5-X, 0.5+Y, -Z
SFAC C H N
UNIT 52 28 8
LIST 4
TEMP -118
SIZE 0.20 0.20 0.30
L.S. 5
BOND $H
CONF
FMAP 2
PLAN 40
ACTA
RIGU C11A > C17A
RIGU C11B > C17B
WGHT       0.069300       0.085500
FVAR            0.15009      0.65162
N1        3       0.624414        0.171230        0.353304        11.00000        0.05625        0.03445 =
             0.05542        0.00093        0.01357        0.00997
N2        3       0.620459       -0.164635        0.326691        11.00000        0.04953        0.03328 =
             0.06477        0.00093        0.01515       -0.00390
C1        1       0.872861        0.001219        0.446704        11.00000        0.04329        0.02093 =
             0.02153        0.00166        0.01222        0.00102
C2        1       0.941022        0.096684        0.488590        11.00000        0.04541        0.01811 =
             0.02929        0.00063        0.01316        0.00254
AFIX    43
H2        2       0.899738        0.161181        0.480565        11.00000       -1.20000
AFIX     0
C3        1       1.062023        0.095500        0.538747        11.00000        0.04509        0.01820 =
             0.02980        0.00033        0.01273        0.00008
AFIX    43
```

```
H3    2    1.105434    0.159239    0.565047    11.00000    -1.20000
AFIX   0
C4    1    0.748911    0.002355    0.394243    11.00000    0.04337    0.02395 =
          0.02759    0.00151    0.01237    0.00148
C5    1    0.681051    0.096958    0.373380    11.00000    0.04315    0.02940 =
          0.03475    0.00038    0.01109    0.00157
C6    1    0.678371   -0.091044    0.356327    11.00000    0.04177    0.02882 =
          0.03935    0.00250    0.01243    0.00195
PART 1
SAME C16A C15A C14A C13A C12A C11A
C11A   1    0.902116    0.071953    0.971248    21.00000    0.06052    0.03252 =
          0.02361   -0.00254    0.01904   -0.00598
C12A   1    0.803229    0.139466    0.940237    21.00000    0.07124    0.05126 =
          0.04045    0.00582    0.02676    0.00710
AFIX   43
H12A   2    0.817759    0.211975    0.960946    21.00000   -1.20000
AFIX   0
C13A   1    0.688384    0.105000    0.882103    21.00000    0.06001    0.08221 =
          0.04532    0.01414    0.02216    0.01562
AFIX   43
H13A   2    0.623483    0.153039    0.861365    21.00000   -1.20000
AFIX   0
C14A   1    0.663876   -0.003861    0.851486    21.00000    0.04012    0.08633 =
          0.03795    0.00400    0.01145   -0.00704
AFIX   43
H14A   2    0.582758   -0.028100    0.811453    21.00000   -1.20000
AFIX   0
C15A   1    0.756674   -0.072704    0.879667    21.00000    0.04141    0.06396 =
          0.03437   -0.00229    0.01159   -0.01452
AFIX   43
H15A   2    0.739901   -0.144903    0.858798    21.00000   -1.20000
AFIX   0
C16A   1    0.878738   -0.037510    0.940171    21.00000    0.04123    0.03656 =
          0.02065   -0.00121    0.01233   -0.00527
C17A   1    0.976211   -0.104863    0.969262    21.00000    0.05015    0.02686 =
          0.02987   -0.00281    0.01694   -0.00913
```

```
AFIX  43
H17A  2     0.960069    -0.177127    0.947915    21.00000    -1.20000
AFIX   0
SAME C11A > C17A
PART 2
C11B  1     0.893425    0.052791    0.956630    -21.00000    0.03496    0.04538 =
          0.02169    0.00263    0.00905    0.01005
C12B  1     0.778852    0.107153    0.912013    -21.00000    0.05112    0.07972 =
          0.03583    0.00836    0.01105    0.02866
AFIX  43
H12B  2     0.777162    0.181010    0.917208    -21.00000    -1.20000
AFIX   0
C13B  1     0.676511    0.053658    0.863984    -21.00000    0.04226    0.10641 =
          0.03971    0.01061    0.01154    0.01725
AFIX  43
H13B  2     0.601582    0.089176    0.839257    -21.00000    -1.20000
AFIX   0
C14B  1     0.678295    -0.056160    0.849342    -21.00000    0.04237    0.12038 =
          0.04250    0.00507    0.01384    -0.00144
AFIX  43
H14B  2     0.604192    -0.093497    0.811115    -21.00000    -1.20000
AFIX   0
C15B  1     0.783231    -0.108433    0.888694    -21.00000    0.04616    0.08934 =
          0.03279    -0.00030    0.01376    -0.01227
AFIX  43
H15B  2     0.780845    -0.182163    0.877841    -21.00000    -1.20000
AFIX   0
C16B  1     0.897202    -0.058293    0.945647    -21.00000    0.03889    0.03872 =
          0.02336    0.00129    0.01098    -0.00073
C17B  1     1.004434    -0.111269    0.989012    -21.00000    0.04830    0.03945 =
          0.02473    0.00211    0.00894    0.01350
AFIX  43
H17B  2     1.007197    -0.185018    0.981456    -21.00000    -1.20000
PART 0
AFIX   0
HKLF 4 1 0 0 1 0 -1 0 1 0 0
```

REM AN_TCNQ_155K in P2(1)/c

REM R1 = 0.0413 for 2271 Fo > 4sig(Fo) and 0.0552 for all 2885 data

REM 200 parameters refined using 125 restraints

END

3. FL-TCNQ at 300 K

```
TITL FL_TCNQ_300K in C2/m
CELL 0.71073    11.00340    13.09670     6.79310    90.0000 103.5837    90.0000
ZERR       2.00      0.00090      0.00110      0.00060      0.0000      0.0013      0.0000
LATT    7
SYMM -X, Y, -Z
SFAC C H N
UNIT 50 28 8
TEMP 27
SIZE 0.40 0.43 0.45
L.S. 5
FMAP 2
PLAN 40
BOND $H
CONF
LIST 4
EQIV $1 2-x, +y, -z
BIND C10 C10_$1
BIND C11 C12
RIGU C6 > C12
ACTA
WGHT       0.070000       0.099900
FVAR            0.33617
N1       3       0.610874       0.165523       0.347325       11.00000       0.07634       0.05496 =
             0.09221       0.00571       0.01873       0.01651
C1       1       0.867831       0.000000       0.449203       10.50000       0.05442       0.03497 =
             0.03289       0.00000       0.01282       0.00000
C2       1       0.937297       0.094391       0.476016       11.00000       0.05796       0.03053 =
             0.04178       0.00006       0.01299       0.00262
AFIX    43
H2       2       0.894484       0.156198       0.459796       11.00000      -1.20000
AFIX     0
C3       1       0.739564       0.000000       0.399236       10.50000       0.05485       0.03952 =
             0.03975       0.00000       0.01271       0.00000
C4       1       0.668625       0.092509       0.371110       11.00000       0.05487       0.04762 =
```

```
            0.05324      0.00013      0.01266      0.00172
PART -1
C6      1      0.764106      0.100392      -0.094367      10.50000      0.07711      0.06887 =
            0.04280      -0.00306      0.00923      0.01415
AFIX   43
H6      2      0.736792      0.167798      -0.106908      10.50000      -1.20000
AFIX    0
C7      1      0.681359      0.020227      -0.125640      10.50000      0.05561      0.08388 =
            0.05006      -0.00093      0.00769      0.01253
AFIX   43
H7      2      0.596017      0.033828      -0.158186      10.50000      -1.20000
AFIX    0
C8      1      0.721988      -0.081614      -0.109857      10.50000      0.06976      0.06857 =
            0.05169      -0.00380      0.01548      -0.00866
AFIX   43
H8      2      0.663372      -0.134062      -0.133083      10.50000      -1.20000
AFIX    0
C9      1      0.848329      -0.105100      -0.060107      10.50000      0.06726      0.05206 =
            0.04150      -0.00441      0.01477      -0.01049
AFIX   43
H9      2      0.875866      -0.172455      -0.049520      10.50000      -1.20000
AFIX    0
C10     1      0.931608      -0.024762      -0.026918      10.50000      0.05671      0.03414 =
            0.03032      -0.00199      0.01138      -0.00139
C11     1      0.891074      0.075999      -0.042898      10.50000      0.06589      0.04256 =
            0.03173      -0.00042      0.00819      0.00971
part 1
C12     1      1.000000      0.147846      0.000000      10.25000      0.08155      0.03618 =
            0.03518      0.00000      0.00720      0.00000
H12     2      0.999590      0.191555      -0.117327      10.50000      -1.20000
HKLF 4

REM    FL_TCNQ_300K in C2/m
REM R1 =    0.0358 for       1044 Fo > 4sig(Fo)    and    0.0391 for all       1178 data
REM       102 parameters refined using         36 restraints
END
```

4. FL-TCNQ at 100 K

```
TITL FL_TCNQ_100K in P-1
CELL 0.71073      8.20940      8.76080      6.63840    98.6193    98.4392 100.1572
ZERR       1.00      0.00100      0.00110      0.00080      0.0018      0.0018      0.0017
LATT    1
SFAC C H N
UNIT 25 14 4
TEMP -173
SIZE 0.40 0.43 0.45
L.S. 5
FMAP 2
PLAN 40
LIST 4
ACTA
BOND $H
CONF
RIGU C1 > C13
MERG 0
WGHT          0.0596          0.0262
BASF      0.51017
FVAR            1.86671
PART -1
C1        1       0.342745       0.645113       0.590743       10.50000       0.02184       0.02531 =
             0.01460       0.00158       0.00413       0.00645
AFIX    43
H1        2       0.446185       0.609915       0.604039       10.50000      -1.20000
AFIX      0
C2        1       0.340844       0.805574       0.623850       10.50000       0.02273       0.03107 =
             0.01905       0.00139       0.00168      -0.00262
AFIX    43
H2        2       0.444007       0.880502       0.657851       10.50000      -1.20000
AFIX      0
C3        1       0.189578       0.857133       0.607640       10.50000       0.02531       0.02133 =
             0.01730       0.00063       0.00196       0.00055
AFIX    43
```

```
H3    2    0.190921    0.967017    0.633494    10.50000    -1.20000
AFIX   0
C4    1    0.035638    0.750383    0.554046    10.50000    0.02531    0.01579 =
          0.01250    0.00033    0.00404    0.00573
AFIX  43
H4    2   -0.067814    0.785559    0.540717    10.50000    -1.20000
AFIX   0
C5    1   -0.271088    0.443359    0.432218    10.50000    0.02006    0.01661 =
          0.01489    0.00397    0.00511    0.00357
AFIX  43
H5    2   -0.317021    0.535865    0.440619    10.50000    -1.20000
AFIX   0
C6    1   -0.375091    0.294432    0.384357    10.50000    0.02287    0.02058 =
          0.01885    0.00395    0.00490    0.00213
AFIX  43
H6    2   -0.493734    0.284753    0.360417    10.50000    -1.20000
AFIX   0
C7    1   -0.307060    0.160127    0.371323    10.50000    0.02820    0.01854 =
          0.01533    0.00313    0.00323   -0.00255
AFIX  43
H7    2   -0.380516    0.059667    0.339126    10.50000    -1.20000
AFIX   0
C8    1   -0.133520    0.168271    0.404187    10.50000    0.02695    0.01887 =
          0.01270    0.00091    0.00100    0.00880
AFIX  43
H8    2   -0.088060    0.075489    0.393978    10.50000    -1.20000
AFIX   0
C9    1    0.158934    0.360954    0.495204    10.50000    0.02354    0.02124 =
          0.01310    0.00174    0.00235    0.01048
AFIX  23
H9A   2    0.206455    0.321141    0.373735    10.50000    -1.20000
H9B   2    0.206621    0.319417    0.616548    10.50000    -1.20000
AFIX   0
C10   1    0.039489    0.591604    0.521128    10.50000    0.01960    0.01623 =
          0.01083    0.00237    0.00511    0.00907
C11   1   -0.099190    0.453027    0.467189    10.50000    0.01791    0.01410 =
```

```
             0.01072       0.00234       0.00422       0.00577
C12    1    -0.029296      0.317851      0.452612      10.50000      0.02233      0.01480 =
             0.01253       0.00150       0.00407       0.00891
C13    1     0.191110      0.537988      0.538128      10.50000      0.01436      0.02342 =
             0.01256       0.00063       0.00173       0.00556
PART 0
N1     3     0.571954      0.743018      0.152618      11.00000      0.02592      0.02740 =
             0.04502       0.00759       0.01078       0.00785
N2     3     0.208255      1.048784      0.156091      11.00000      0.03091      0.01803 =
             0.02976       0.00326       0.00810       0.00563
C14    1     0.131676      0.634448      0.051229      11.00000      0.02368      0.01613 =
             0.01263       0.00310       0.00633       0.00463
C15    1     0.167121      0.477823      0.024300      11.00000      0.02234      0.01754 =
             0.01555       0.00298       0.00633       0.00690
AFIX   43
H15    2     0.280583      0.465063      0.041211      11.00000     -1.20000
AFIX    0
C16    1    -0.041627      0.650663      0.024501      11.00000      0.02426      0.01527 =
             0.01551       0.00318       0.00618       0.00668
AFIX   43
H16    2    -0.067555      0.752790      0.041440      11.00000     -1.20000
AFIX    0
C17    1     0.260381      0.765276      0.101554      11.00000      0.02346      0.01639 =
             0.01587       0.00305       0.00607       0.00511
C18    1     0.433057      0.752127      0.129482      11.00000      0.02585      0.01716 =
             0.02338       0.00314       0.00763       0.00352
C19    1     0.229966      0.922231      0.130770      11.00000      0.02119      0.01829 =
             0.01839       0.00302       0.00489       0.00168
HKLF 5

REM    FL_TCNQ_100K in P-1
REM R1 =    0.0306 for       1994 Fo > 4sig(Fo)    and    0.0317 for all       2093 data
REM       191 parameters refined using       108 restraints

END
```

5. TET-TCNQ at 300 K

```
TITL Tetracene_TCNQ_300K in C2/m
CELL 0.71073   11.89660   12.88460    7.25670   90.0000   90.1902   90.0000
ZERR    2.00    0.00100    0.00110    0.00060    0.0000    0.0014    0.0000
LATT  7
SYMM -X, Y, -Z
SFAC C H N
UNIT 60 32 8
TEMP 27
SIZE 0.20 0.22 0.45
L.S. 5
FMAP 2
PLAN 40
BOND $H
CONF
LIST 4
ACTA
EQIV $1 2-x, -y, 1-z
DFIX 0.93 0.01 C13A H13A
SADI 0.01 H13A C12A H13A C5A_$1
RIGU C5A C6A C7A C8A C9A C10A C11A C12A C13A
RIGU C5B C6B C7B C8B C9B
BIND C5A C5A_$1
BIND C13A C5A_$1
WGHT      0.071000      0.108300
EXTI      0.015261
FVAR           0.15220     0.65256
N1    3     0.660539     0.167415    -0.151262    11.00000     0.07667     0.07317 =
           0.10948     0.00106    -0.01838     0.01687
C1    1     0.885274     0.000000    -0.049830    10.50000     0.05147     0.04841 =
           0.04243     0.00000     0.00218     0.00000
C2    1     0.945361     0.095500    -0.023372    11.00000     0.05680     0.04203 =
           0.05981     0.00055    -0.00130     0.00320
AFIX  43
H2    2     0.908014     0.158323    -0.038847    11.00000    -1.20000
```

AFIX 0

C3 1 0.773586 0.000000 -0.099862 10.50000 0.05343 0.05458 =
0.04980 0.00000 -0.00205 0.00000

C4 1 0.711513 0.093723 -0.127790 11.00000 0.05553 0.06428 =
0.06531 -0.00098 -0.00801 0.00210

PART -1

C5A 1 1.005875 0.052181 0.485710 20.50000 0.04616 0.06207 =
0.02623 0.00352 0.01833 -0.00144

SAME C13A C12A C11A C10A C9A C8A C7A C6A

C6A 1 0.912646 0.109341 0.459176 20.50000 0.06018 0.06664 =
0.07513 -0.00778 0.00691 -0.00400

AFIX 43

H6A 2 0.919714 0.180918 0.470983 20.50000 -1.20000

AFIX 0

C7A 1 0.806757 0.070971 0.415711 20.50000 0.06159 0.06880 =
0.04498 -0.00714 0.01135 -0.00165

C8A 1 0.713756 0.133911 0.364571 20.50000 0.05737 0.08645 =
0.08005 0.00093 -0.00471 0.00287

AFIX 43

H8A 2 0.721190 0.205723 0.360385 20.50000 -1.20000

AFIX 0

C9A 1 0.615192 0.089271 0.322360 20.50000 0.05790 0.10215 =
0.08264 -0.00754 -0.00114 0.00046

AFIX 43

H9A 2 0.554172 0.131552 0.294074 20.50000 -1.20000

AFIX 0

C10A 1 0.600220 -0.021039 0.319135 20.50000 0.04585 0.09937 =
0.08516 -0.00847 -0.00315 -0.00131

AFIX 43

H10A 2 0.530249 -0.048977 0.290372 20.50000 -1.20000

AFIX 0

C11A 1 0.687290 -0.084418 0.357684 20.50000 0.03897 0.09327 =
0.08296 -0.00883 -0.00719 -0.01124

AFIX 43

H11A 2 0.678965 -0.156116 0.351986 20.50000 -1.20000

AFIX 0

```
C12A    1       0.793967    -0.038476       0.408112        20.50000        0.04009         0.07493 =
             0.04900     -0.00230        0.00388     -0.00320
C13A    1       0.886582    -0.098967       0.448972        20.50000        0.04492         0.05885 =
             0.06641     -0.00552        0.00203     -0.01304
H13A    2       0.890315    -0.170826       0.428301        20.50000        -1.20000
PART 2
SAME C5A C6A C7A C8A C9A
C5B     1       1.000000        0.060827        0.500000        -20.50000       0.05495         0.03974 =
             0.05806         0.00000         -0.00644        0.00000
C6B     1       0.903116        0.113470        0.455782        -21.00000       0.04459         0.05585 =
             0.04495         0.00208         -0.00347        0.00106
AFIX    43
H6B     2       0.900671        0.185589        0.459135        -21.00000       -1.20000
AFIX     0
C7B     1       0.808145        0.055607        0.405527        -21.00000       0.03902         0.06534 =
             0.04489     -0.00165        -0.00123        0.00149
C8B     1       0.705091        0.107052        0.360527        -21.00000       0.04517         0.08092 =
             0.06421     -0.00841        0.00029     -0.00594
AFIX    43
H8B     2       0.703276        0.179193        0.363422        -21.00000       -1.20000
AFIX     0
C9B     1       0.609162        0.054856        0.313457        -21.00000       0.04431         0.07791 =
             0.07019         0.00105     -0.00747        -0.00387
AFIX    43
H9B     2       0.544419        0.091234        0.281690        -21.00000       -1.20000
PART 0
AFIX     0
HKLF 4

REM    Tetracene_TCNQ_300K in C2/m
REM R1 =    0.0400 for        1187 Fo > 4sig(Fo)    and    0.0447 for all        1369 data
REM        167 parameters refined using        103 restraints

END
```